

1

UNIVERSITY OF BRISTOL

2

DOCTORAL THESIS

3

4

Investigating, implementing, and creating methods for analysing large neuronal ensembles

5

6

7

Author:

Thomas J. DELANEY

Supervisors:

Dr. Cian O'DONNELL

Dr. Michael C. ASHBY

8

A thesis submitted in fulfillment of the requirements

for the degree of Doctor of Philosophy

9

in the

10

Biological Intelligence & Machine Learning Unit

11

Department of Computer Science

12

July 9, 2020

¹⁵ Declaration of Authorship

¹⁶ I, Thomas J. DELANEY, declare that this thesis titled, "Investigating, implementing, and
¹⁷ creating methods for analysing large neuronal ensembles" and the work presented in it are
¹⁸ my own. I confirm that:

- ¹⁹ • This work was done wholly or mainly while in candidature for a research degree at this
²⁰ University.
- ²¹ • Where any part of this thesis has previously been submitted for a degree or any other
²² qualification at this University or any other institution, this has been clearly stated.
- ²³ • Where I have consulted the published work of others, this is always clearly attributed.
- ²⁴ • Where I have quoted from the work of others, the source is always given. With the
²⁵ exception of such quotations, this thesis is entirely my own work.
- ²⁶ • I have acknowledged all main sources of help.
- ²⁷ • Where the thesis is based on work done by myself jointly with others, I have made
²⁸ clear exactly what was done by others and what I have contributed myself.

²⁹

³⁰ Signed:

³¹ _____

³² Date:

³³ _____

34

UNIVERSITY OF BRISTOL

35

Abstract

36

Engineering

37

Department of Computer Science

38

Doctor of Philosophy

39

**Investigating, implementing, and creating methods for analysing large neuronal
ensembles**

41

by Thomas J. DELANEY

42

The Thesis Abstract is written here (and usually kept to just this page). The page is kept centered vertically so can expand into the blank space above the title too...

44

Acknowledgements

45 The acknowledgments and the people to thank go here, don't forget to include your project

46 advisor...

⁴⁷ Contents

⁴⁸	Declaration of Authorship	iii
⁴⁹	Abstract	v
⁵⁰	Acknowledgements	vii
⁵¹	1 Introduction	1
⁵²	1.1 Overview	1
⁵³	2 Sensitivity of the spikes-to-fluorescence transform to calcium indicator and neu-	
⁵⁴	ron properties	7
⁵⁵	2.1 Introduction	8
⁵⁶	2.2 Methods	10
⁵⁷	2.2.1 Calcium dynamics model	10
⁵⁸	Photon release & capture	12
⁵⁹	2.2.2 Parameter optimisation	13
⁶⁰	Fixed parameters	14
⁶¹	2.2.3 Julia	14
⁶²	2.2.4 Spike inference	16
⁶³	Comparing spike inference quality	18
⁶⁴	2.2.5 Perturbation analysis	18
⁶⁵	2.2.6 Signal-to-noise ratio	18
⁶⁶	2.2.7 Data sources	19
⁶⁷	2.3 Results	19
⁶⁸	2.3.1 A biophysical computational model can generate accurate fluores-	
⁶⁹	cence traces from spike trains	19
⁷⁰	2.3.2 Spike inference algorithms perform similarly on real data compared	
⁷¹	with time series simulated from the model	20
⁷²	2.3.3 Relative effects of various buffers to the fluorescence signal	21

73	2.3.4 Spike inference accuracy is sensitive to indicator properties, and likely varies within and between cells	22
74		
75	2.3.5 Single spike inference accuracy drops for high firing rates, but firing rate itself can be estimated from mean fluorescence amplitude	27
76		
77	2.4 Discussion	29
78	3 Functional networks expand across anatomical boundaries as correlation time-scale increases	33
79		
80	3.1 Introduction	34
81	3.2 Data	35
82	3.2.1 Brain regions	35
83	3.2.2 Video recordings	36
84	3.3 Methods	36
85	3.3.1 Binning data	36
86	3.3.2 Correlation coefficients	37
87	Total correlations, r_{SC}	37
88	Shuffled total correlations	38
89	Separating Correlations & Anti-correlations	38
90	3.3.3 Conditioning on behavioural data	38
91	Linear regression	38
92	Elastic net regularisation	39
93	Conditional covariance	39
94	Measures of conditional correlation	40
95	3.3.4 Information Theory	41
96	Entropy $H(X)$	41
97	Maximum entropy limit	41
98	Mutual Information $I(X; Y)$	42
99	Variation of Information $VI(X, Y)$	44
100	Measuring entropies & mutual information	44
101	3.3.5 Network analysis	44
102	Correlation networks	44
103	Rectified correlations	45
104	Sparsifying data networks	45
105	Communities	45

106	Weighted configuration model	46
107	Sparse weighted configuration model	46
108	Spectral rejection	46
109	Node rejection	47
110	Community detection	48
111	3.3.6 Clustering Comparison	48
112	Adjusted Rand Index	48
113	Clusterings as random variables	49
114	Information based similarity measures	50
115	Information based metrics	50
116	Comparing detected communities and anatomical divisions	51
117	3.4 Results	51
118	3.4.1 Average correlation size increases with increasing time bin width	52
119	3.4.2 Goodness-of-fit for Poisson and Gaussian distributions across increasing time bin widths	54
120	3.4.3 Differences between and inter- and intra- regional correlations decrease with increasing bin width	54
121	3.4.4 Connected and divided structure in correlation based networks reduces in dimension with increasing bin width	57
122	3.4.5 Detecting communities in correlation based networks	58
123	3.4.6 Functional communities resemble anatomical division at short timescales	61
124	3.4.7 Conditional correlations & signal correlations	61
125	3.4.8 Absolute correlations and negative rectified correlations	66
126	3.5 Discussion	67
130	4 A simple two parameter distribution for modelling neuronal activity and capturing neuronal association	73
131	4.1 Introduction	74
132	4.2 Data	75
133	4.2.1 Experimental protocol	75
134	4.3 Methods	76
135	4.3.1 Binning data	76
136	4.3.2 Number of <i>active</i> neurons	76
137	4.3.3 Moving windows for measurements	76

139	4.3.4	Fano factor	78
140	4.3.5	Probability Distributions suitable for modelling ensemble activity . .	78
141		Association	78
142		Binomial distribution	79
143		Beta-binomial distribution	79
144		Conway-Maxwell-binomial distribution	80
145	4.3.6	Fitting	82
146	4.3.7	Goodness-of-fit	84
147	4.4	Results	84
148	4.4.1	Increases in mean number of active neurons and variance in number of active neurons at stimulus onset in some regions	84
149		Primary visual cortex	85
150		Hippocampus	85
151		Thalamus	85
152	4.4.2	Conway-Maxwell-binomial distribution is usually a better fit than bi- nomial or beta-binomial	85
153	4.4.3	Conway-Maxwell-binomial distribution captures changes in associ- ation at stimulus onset	90
154	4.4.4	Replicating stimulus related quenching of neural variability	90
155	4.5	Discussion	92
159	5	Studies with practical limitations & negative results	95
160	5.1	Dynamic state space model of pairwise and higher order neuronal correlations	96
161	5.2	A multiscale model for hierarchical data applied to neuronal data	96
163	6	Discussion	99
164	Bibliography		107

165 List of Figures

166 2.1	A: Example spike train (blue) and the corresponding GCaMP6s fluorescence 167 trace (green), data replotted from (Berens et al., 2018). Inset shows zoomed 168 section of traces to highlight slow decay of GCaMP6s fluorescence relative 169 to spike time intervals. B: Schematic diagram of the neuron calcium and 170 GCaMP computational model. C: Good visual match of data fluorescence 171 trace (green) and model simulated fluorescence (orange) in response to an 172 identical spike train (blue).	9
173 2.2	A: Workflow to compare spike inference for real versus simulated fluores- 174 cence data. B: True positive rates achieved by three different spike inference 175 algorithms when applied to observed spike trains, and simulated spike trains. 176 Data points overlaid as blue circles. The performance is similar from real 177 and simulated data for each of the algorithms.	21
178 2.3	Calcium Buffering Dynamics (a) The proportions of bound and free cal- 179 cium concentrations within a cell, with the associated spike train. (b)-(f) The 180 dynamics of the concentration of (b) excited indicator bound calcium, (c) in- 181 dicator bound calcium, (d) immobile endogenous buffer bound calcium, (e) 182 mobile endogenous buffer bound calcium, and (f) free calcium in response to 183 an action potential at $\sim 23.2\text{s}$	23
184 2.4	(a) An example trace for each of the five pairs of values used for the binding 185 and unbinding rates of the fluorescent calcium indicator. (b) The signal-to- 186 noise ratio of the modelled fluorescence traces using each of the four per- 187 turbed value pairs, and the experimental value. The SNRs for the value pairs 188 perturbed downward are lower than that for the unperturbed value pair or 189 the higher value pairs. (c) The true-positive rates of the deconvolution al- 190 gorithm's predictions when inferring from the observed data, and inferring 191 from modelled traces using the perturbed and experimental values.	25

192	2.5 (a) An example trace for each of the five perturbed values for the concentration of fluorescent calcium indicator. The top two traces are produced by the lower perturbed values, the middle trace is produced by the experimental value, and the lowest two traces are produced when using the higher perturbed values. (b) The signal-to-noise ratio of the modelled fluorescence traces using each of the four perturbed values, and the experimental value. Extreme perturbations of the concentration either above or below the experimental level lowered the SNR. (c) The true-positive rates of the deconvolution algorithm's predictions when inferring from the observed data, and inferring from modelled traces using the perturbed and experimental values. We found that the algorithms performs equally badly on the two most extreme values, and performs equally well on the experimental value, and the next higher perturbed value.	26
205	2.6 (a) An example trace for each of the five perturbed values for the concentration of immobile endogenous buffer. (b) The signal-to-noise ratio of the modelled fluorescence traces using each of the four perturbed values, and the experimental value. The lower values for the immobile buffer produce the same SNR as the experimental value. But the higher perturbed values produce fluorescence traces with a lower SNR. (c) The true-positive rates of the deconvolution algorithm's predictions when inferring from the observed data, and inferring from modelled traces using the perturbed and experimental values.	28
214	2.7 Simulating fluorescence traces at different firing rates Example modelled traces created using simulated spike trains with a mean firing rate of 1Hz (left column), 5Hz (middle column), and 10Hz (right column). Note the difference in amplitude with different mean firing rates.	29
218	2.8 Inference quality and $\Delta F/F_0$ vs Firing rate (left) The spike inference accuracy when applied to 30 traces created using simulated spike trains with mean firing rates of 1, 5, and 10 Hz. (right) The mean $\Delta F/F_0$ across those 30 traces for each frequency.	30
222	3.1 Probe Locations: The locations of the probes in each of the three mouse brains (Stringer et al., 2019).	36

224	3.2 Entropy Limit: The upper limit on entropy of binned spike count data as 225 a function of the maximum observed spike count. The orange line is the 226 analytical maximum. The blue line is the entropy of samples with $N = 1000$ 227 data points taken from the discrete uniform distribution.	42
228	3.3 (A) An example of the correlation coefficients between two different pairs 229 of cells, one where both cells are in the same brain region (intra-regional 230 pair), and one where both cells are in different brain regions (inter-regional 231 pair). The correlation coefficients have been measured using different time 232 bin widths, ranging from 5ms to 3s. Note the increasing amplitude of the 233 correlations with increasing bin width. (B) A raster plot showing the spike 234 times of each pair of cells.	52
235	3.4 Mean correlation coefficients measured from pairs of 50 randomly chosen 236 neurons. (A) All possible pairs, (B) positively correlated pairs, and (C) neg- 237 atively correlated pairs. (D) Mean and standard error of χ^2 test statistics for 238 Poisson and Gaussian distributions fitted to neuron spike counts.	53
239	3.5 (Left)The mean intra-region and inter-region correlations using all possible 240 pairs of ~ 500 neurons, spread across 9 different brain regions. (Right) 241 Courtesy of Stringer et al. (2019), mean inter-regional (out-of-area) corre- 242 lation coefficients vs mean intra-regional (within-area) correlation coefficients 243 for a bin width of 1.2s. Note that the intra-regional coefficients are higher in 244 each case.	55
245	3.6 The mean intra-regional correlations (coloured dots) and mean inter-regional 246 correlations (black dots) for a given region, indicated on the x-axis, for dif- 247 ferent time bin widths. Each black dot represents the mean inter-regional 248 correlations between the region indicated on the x-axis and one other region. 249 (A) shows these measurements when we used a time bin width of 5ms. (B) 250 shows these measurements when we used a time bin width of 1s. Note that 251 the difference between the mean inter-regional correlations and mean intra- 252 regional correlations is smaller for 1s bins.	56
253	3.7 Mean inter-regional (main diagonal) and intra-regional (off diagonal) corre- 254 lation coefficients. (A) Shows these measurements when spike times were 255 binned using 5ms time bins. (B) Shows the same, using 1s time bins. Note 256 that the matrices are ordered according to the main diagonal values, therefore 257 the ordering is different in each subfigure.	57

258 3.8 The number of dimensions in the k -partite and connected structure in the cor-	
259 relation based networks beyond the structure captured by a sparse weighted	
260 configuration null network model (see section 3.3.5), shown for different time	
261 bin widths. Note that the k -partite structure disappears for time bin width	
262 greater than 200ms for all three subjects. The dimension of the connected	
263 structure reduces with increasing bin width for 2 of the 3 subjects (top row).	59
264 3.9 (A-B) Correlation matrices with detected communities indicated by white	
265 lines. Each off main diagonal entry in the matrix represents a pair of neu-	
266 rons. Those entries within a white square indicate that both of those neurons	
267 are in the same community as detected by our community detection proce-	
268 dure. Matrices shown are for 5ms and 1s time bin widths respectively. Main	
269 diagonal entries were set to 0. (C-D) Matrices showing the anatomical dis-	
270 tribution of pairs along with their community membership. Entries where	
271 both cells are in the same region are given a colour indicated by the colour	
272 bar. Entries where cells are in different regions are given the grey colour also	
273 indicated by the colour bar.	60
274 3.10 (A) The variation of information is a measure of distance between cluster-	
275 ings. The distance between the anatomical ‘clustering’ and community de-	
276 tection ‘clustering’ increases with increasing time bin width. (B) The ad-	
277 justed Rand index is a normalised similarity measure between clusterings.	
278 The anatomical and community detection clusterings become less similar as	
279 the time bin width increases.	62
280 3.11 Comparing the components of the total covariance across different values for	
281 the time bin width. We observed a consistent increase in $E[\text{cov}(X, Y Z)]$ as	
282 the time bin width increased. But we saw different trends for $\text{cov}(E[X Z], E[Y Z])$	
283 for each mouse.	63
284 3.12 Comparing the components of the total covariance across different values for	
285 the time bin width. We saw a consistent increase in $\rho_{X,Y Z}$ as the time bin	
286 width increased in all three subjects. But we saw different trends in ρ_{signal} for	
287 each of the subjects.	64

288	3.13 Matrices showing the regional membership of pairs by colour, and the com-	
289	munities in which those pairs lie. (A-B) Detected communities and regional	
290	membership matrix for network based on rectified spike count correlation	
291	$\rho_{X,Y Z}$, using time bin widths of 0.005s and 1s respectively. (C-D) Detected	
292	communities and regional membership matrix for network based on rectified	
293	signal correlation ρ_{signal} , using time bin widths of 0.005s and 1s respectively.	65
294	3.14 Distance and similarity measures between the anatomical division of the neu-	
295	rons, and the communities detected in the network based on the spike count	
296	correlations $\rho_{X,Y Z}$. (A) The variation of information is a ‘distance’ mea-	
297	sure between clusterings. The distance between the anatomical ‘clustering’	
298	and the community clustering increases as the time bin width increases. (B)	
299	The adjusted Rand index is a similarity measure between clusterings. The	
300	detected communities become less similar to the anatomical division of the	
301	cells as the time bin width increases.	66
302	3.15 Distance and similarity measures between the anatomical division of the neu-	
303	rons, and the communities detected in the network based on the signal cor-	
304	relations ρ_{signal} . (A) The variation of information is a ‘distance’ measure be-	
305	tween clusterings. The distance between the anatomical ‘clustering’ and the	
306	community clustering increases as the time bin width increases. (B) The ad-	
307	justed Rand index is a similarity measure between clusterings. The detected	
308	communities become less similar to the anatomical division of the cells as	
309	the time bin width increases.	67
310	3.16 (A-B) Absolute correlation matrices with detected communities indicated by	
311	white lines. These communities are based on the absolute value of the total	
312	correlation between each pair of cells. Those entries within a white square in-	
313	dicate that both of those neurons are in the same community. Matrices shown	
314	are for 5ms and 1s time bin widths respectively. Main diagonal entries were	
315	set to 0. (C-D) Matrices showing the anatomical distribution of pairs along	
316	with their community membership. Regional membership is indicated by the	
317	colour bar. (E) Variation of information between the anatomical division of	
318	the cells, and the detected communities. (F) Adjusted Rand index between	
319	the anatomical division, and the detected communities.	68

320	3.17 (A-B) Sign reversed rectified correlation matrices with detected communities indicated by white lines. Those entries within a white square indicate that both of those neurons are in the same community. Matrices shown are for 5ms and 1s time bin widths respectively. Main diagonal entries were set to 0. (C-D) Matrices showing the anatomical distribution of pairs along with their community membership. Regional membership is indicated by the colour bar. (E) Variation of information between the anatomical division of the cells, and the detected communities. (F) Adjusted Rand index between the anatomical division, and the detected communities.	69
329	4.1 Figures showing the over-dispersion possible for a beta-binomial distribution relative to a binomial distribution. Parameters are shown in the captions. . .	80
331	4.2 Figures showing (A) the under-dispersion and (B) over-dispersion permitted by the COMb distribution relative to a binomial distribution. (C) illustrates that the p parameter of the COMb distribution does not correspond to the mean of the distribution, as it does for the binomial and beta-binomial distributions. (D) shows a heatmap for the value of the Kullback-Liebler divergence between the COMb distribution and the standard binomial distribution with same value for n , as a function of p and ν . Parameters are shown in the captions.	83
339	4.3 (A) Raster plot showing the spikes fired by 33 randomly chosen neurons in the primary visual cortex. (B-C) (B) average and (C) variance of the number of active neurons, measured using a sliding window 100ms wide, split into 100 bins. The midpoint of the time interval for each window is used as the timepoint (x-axis point) for the measurements using that window. The grey shaded area indicates the presence of a visual stimulus. The opaque line is an average across the 160 trials that included a visual stimulus of any kind. We can see a transient increase in the average number of active neurons and the variance of this number, followed by a fluctuation and another increase. .	86

348	4.4 (A) Raster plot showing the spikes fired by 33 randomly chosen neurons in 349 the hippocampus. (B-C) (B) average and (C) variance of the number of active 350 neurons, measured using a sliding window 100ms wide, split into 100 bins. 351 The midpoint of the time interval for each window is used as the timepoint (x- 352 axis point) for the measurements using that window. The grey shaded area 353 indicates the presence of a visual stimulus. The opaque line is an average 354 across the 160 trials that included a visual stimulus of any kind. We can see 355 a transient increase in the average number of active neurons and the variance 356 of this number at stimulus onset.	87
357	4.5 (A) Raster plot showing the spikes fired by 33 randomly chosen neurons in 358 the thalamus. (B-C) (B) average and (C) variance of the number of active 359 neurons, measured using a sliding window 100ms wide, split into 100 bins. 360 The midpoint of the time interval for each window is used as the timepoint (x- 361 axis point) for the measurements using that window. The grey shaded area 362 indicates the presence of a visual stimulus. The opaque line is an average 363 across the 160 trials that included a visual stimulus of any kind. We can 364 see in immediate increase at stimulus onset, a subsequent fall, and another 365 sustained increased until the stimulus presentation ends.	88
366	4.6 (A) An example of the binomial, beta-binomial, and Conway-Maxwell-binomial 367 distributions fitted to a sample of neural activity. The Conway-Maxwell- 368 binomial distribution is the best fit in this case. The histogram shows the 369 empirical distribution of the sample. The probability mass function of each 370 distribution is indicated by a different coloured line. (B) Across all samples 371 in all trials, the proportion of samples for which each fitted distribution was 372 the the best fit. The Conway-Maxwell-binomial distribution was the best fit 373 for 93% of the samples taken from V1 using a bin width of 1ms.	89

374	4.7 (A) We fit a Conway-Maxwell-binomial distribution to the number of active	
375	neurons in 1ms time bins of a 100ms sliding window. We did this for all	
376	trials with a visual stimulus and took the average across those trials. We	
377	see a transient drop in value for the distribution's ν parameter at stimulus	
378	onset. This shows an increase in association between the neurons. (B) We	
379	measured the correlation coefficient between the spike counts of all possible	
380	pairs of neurons in the same sliding window. The took the average of those	
381	coefficients. We also did this for every visually stimulated trial, and took	
382	the average across trials. The increase in association is not reflected with an	
383	increase in average correlation.	91
384	4.8 (A) The mean Fano factor of the spike counts of the cells in the primary visual	
385	cortex. Means were taken across cells first, then across trials. There was a	
386	significant decrease in the Fano factors immediately after stimulus onset. (B)	
387	The mean Fano factor of the spike counts of the cells in the motor cortex. No	
388	significant change in measurements at any point.	92

389 List of Tables

390 2.1	Fixed parameters A table of the parameters fixed before optimising the	
391	model. The values of these parameters could be changed to model differ-	
392	ent fluorescent calcium indicators.	15
393 4.1	Details of the different bin width and analysis window sizes used when bin-	
394	ning spike times, and analysing those data.	77
395 4.2	Relative dispersion of the COMb distribution, and association between Bernoulli	
396	variables as represented by the value of the ν parameter.	82
397 4.3	Proportion of samples for which each distribution was the best fit, grouped	
398	by bin width. The COMb distribution is the best fit most of the time.	90

³⁹⁹ List of Abbreviations

COMb Conway-Maxwell-binomial (distribution)

OASIS Online active set method to infer spikes

SNR Signal to noise ratio

⁴⁰⁰ **List of Symbols**

$[Ca^{2+}]$	Free calcium concentration	mol
$[BCa]$	Fluorescent indicator bound calcium	mol
$[ECa]$	Endogenous mobile buffer bound calcium	mol
$[ImCa]$	Immobile mobile buffer bound calcium	mol
$[BCa^*]$	excited fluorescent indicator bound calcium	mol
k_{X_f}	binding (affinity) rate	s^{-1}
k_{X_b}	unbinding (dissociation) rate	s^{-1}

For/Dedicated to/To my...

402 **Chapter 1**

403 **Introduction**

404 **1.1 Overview**

405 Since Hodgkin and Huxley's squid experiments featuring a single axon (Hodgkin and Hux-
406 ley, 1939), to more recent research with spike sorted data from ~ 24000 neurons from 34
407 brain regions from 21 mice (Allen et al., 2019), the number of neurons contributing to elec-
408 trophysiological datasets has been growing. Recording methods using two-photon calcium
409 imaging have also been used to extract data from populations containing over 10000 neurons
410 (Peron et al., 2015). This dramatic growth in the number of neurons available for analysis
411 requires a dramatic change in analysis methods. In this project, we have attempted to address
412 some of the difficulties in collecting data from these large ensembles, and analysing these
413 data.

414 To focus on calcium imaging for a start, a neuron that contains a fluorescent calcium
415 indicator in its cytoplasm will fluoresce when bombarded with photons. The amount that the
416 cell will fluoresce is dependent on the concentration of fluorescent indicator within the cell,
417 and the concentration of calcium within the cell. When a neuron fires an action potential, the
418 influx of free calcium ions causes an increase in fluorescence when those ions bond with the
419 fluorescent indicator and those bounded molecules are bombarded with photons. After the
420 action potential, as calcium is extruded from the cell the fluorescence returns to a baseline
421 level. This is the basic mechanism of fluorescent calcium indicator based imaging.

422 This method has some advantages over electrophysiology as measure of neuronal ensem-
423 ble activity. Isolating individual neurons is easier and more reliable than identifying unique
424 spike sources in electrophysiology (Buccino et al., 2019). Also, spike sorting methods can
425 only detect spikes, but imaging methods can also detect cells that are not spiking, because
426 cells will emit a baseline level of fluorescence when not firing action potentials. Calcium
427 imaging sites can be re-used for weeks for longitudinal studies (Chen et al., 2013). The

428 fluorescent indicator is delivered to the cell by adeno-associated viruses, consequently there
429 can be problems with indicator gradients around the infection site, and expression levels
430 will change in individual cells over weeks (Tian et al., 2009; Chen et al., 2013). This de-
431 livery method can also cause cell pathology, and nuclear filling (Zariwala et al., 2012), but
432 these problems can be solved by using lines of transgenic mice (Dana et al., 2014). The
433 fluorescence signal itself can serve a a good indicator of cell activity, but similarly to electro-
434 physiology, the aim of calcium imaging is often spike detection.

435 If the imaging data is collected at a high enough frequency, and the signal-to-noise ratio
436 of the fluorescence trace is high enough, it should be possible to infer the spike times to some
437 level of accuracy. For example, the calmodulin based indicator GCaMP6s has a sufficiently
438 high signal-to-noise ratio that isolated action potentials can be detected and inferred (Chen
439 et al., 2013). Many spike inference algorithms exist (Vogelstein et al., 2010; Pnevmatikakis
440 et al., 2016; Friedrich and Paninski, 2016; Pnevmatikakis et al., 2013; Pnevmatikakis et al.,
441 2014; Deneux et al., 2016; Greenberg et al., 2018), and some of these can perform both cell
442 isolation and spike detection simultaneously (Vogelstein et al., 2010; Pnevmatikakis et al.,
443 2016; Pnevmatikakis et al., 2014; Deneux et al., 2016). But the relationship between spik-
444 ing and fluorescence change is not fully understood. For example, the fluorescent indicator
445 will act like an additional calcium buffer within the cell cytoplasm and will compete with
446 the other endogenous buffers to bind with free calcium cells. Therefore, the concentration of
447 those endogenous buffers, and the binding dynamics of those buffers will have an effect on
448 the change in fluorescence in response to an action potential. Furthermore, the binding dy-
449 namics of the fluorescent indicator itself will have an effect on the change in fluorescence. For
450 example, the GCaMP series of fluorescence indicators are based on the calcium buffer pro-
451 tein *calmodulin*. This protein has four binding sites, whose affinities interact non-linearly.
452 But most of the spike inference algorithms model the fluorescence as a linear function of a
453 calcium trace, and they model this calcium trace as a first or second order autoregression with
454 a pulse input to represent action potentials. Deneux et al. (2016) developed a spike inference
455 algorithm with a bit more biological inspiration, but this amounted to a very similar process.
456 While this autoregression idea appears to be a reasonable approximation, the algorithms that
457 use this approximation are outperformed by the most recently published spike inference al-
458 gorithm to be cited here (Greenberg et al., 2018). This algorithm does take into account the
459 binding dynamics of both the endogenous buffers and fluorescent calcium indicator, and the
460 concentrations of free calcium, indicator, and endogenous buffer within the cell cytoplasm.
461 This shows that there is value in more biologically inspired models of fluorescent calcium

462 indicators.

463 In light of the growing popularity of two-photon calcium imaging, and the lack of biolog-
464 ically inspired spike inference algorithms (Greenberg et al. developed their spike inference
465 algorithm in parallel to our work), we decided to develop a biologically inspired model for
466 fluorescent calcium indicator fluorescence. The idea being that our model would take a spike
467 train, or simply spike times, provided by the user, and return the fluorescence trace that would
468 be induced by this spike train or spike times. The model contains parameters for concentra-
469 tions of indicator and endogenous buffers, as well as affinity and unbinding rates for these
470 buffers. There are also parameters for the baseline concentration of free calcium in the cell
471 cytoplasm, and the cell radius (as a means for calculating the cell volume). With this model,
472 we hoped that experimentalists would be able to test out different calcium indicators on the
473 types of spike trains that they expect to encounter. This way they could decide ahead of time
474 which indicator suited their situation best. Since the output of our model is a fluorescence
475 trace, the spike inference models mentioned above can be applied to the modelled fluores-
476 cence. This means that the model could also be used to benchmark the performance of these
477 spike inference algorithms, and to investigate the impact of variations in the model on spike
478 inference accuracy.

479 We have outlined some of the advantages that calcium imaging has over electrophysiolog-
480 ogy. But electrophysiology is more useful in some situations. One particular drawback for
481 two-photon calcium imaging is that it can only be used for imaging near to the surface of the
482 brain. Although imaging with three (or presumably more) photons may solve this problem
483 in the future (Ouzounov et al., 2017). A better option for reading activity from neurons be-
484 yond the surface of the brain is to use Neuropixels probes (Jun et al., 2017). These probes
485 can be used to read from thousands of neurons simultaneously in many different areas of the
486 brain (Allen et al., 2019; Stringer et al., 2019; Steinmetz, Carandini, and Harris, 2019; Stein-
487 metz et al., 2019). This brings us to another problem for which we require new innovations
488 in our analysis methods. Specifically, analysing correlated behaviour in neural ensembles
489 consisting of neurons from many different brain regions.

490 Until the invention of new technologies such as the Neuropixels probes, most elec-
491 trophysiology datasets read from neurons in only one or two regions. Therefore most of
492 the research on interactions between neurons in different regions is limited to two regions
493 (Wierzynski et al., 2009; Patterson et al., 2014; Girard, Hupé, and Bullier, 2001). In chapters
494 3 and 4 we used datasets with neurons from 9 and 5 different brain regions respectively.

495 In light of recent findings based on correlated behaviour showing that spontaneous be-
496 haviours explain activity in many different parts of the brain that would otherwise be regarded
497 as noise (Stringer et al., 2019), that satiety is represented brain wide (Allen et al., 2019), and
498 that exploratory and non-exploratory states are represented in the amygdala (Gründemann
499 et al., 2019), it was clear that state representation or motor control had an influence on cor-
500 related behaviour in areas of the brain not usually associated with these tasks. Also, given
501 differences in timescales of fluctuations in different brain regions (Murray et al., 2014), and
502 different timescales for event representation in different brain regions (Baldassano et al.,
503 2017), we decided to investigate brain wide correlated behaviour at timescales ranging from
504 5ms up to 3s.

505 We started off measuring the correlations in spike counts between individual neurons in
506 our ensemble. These measurements induced a weighted undirected graph where each node
507 represented a neuron, and the weight of each edge was the strength of the correlation be-
508 tween the neurons represented by the nodes at either end of that edge. In order to put the
509 neurons into groups with correlated behaviour, we applied a novel community detection al-
510 gorithm (Humphries et al., 2019) to this graph. We repeated this analysis for timescales
511 from milliseconds to seconds. Bear in mind that our correlation based graph was completely
512 agnostic of the anatomical regions in which our cells resided. We then compared our corre-
513 lated communities to their anatomy at each timescale. In this way, we used a novel method,
514 never applied neuronal data before, to analyse the makeup of correlated communities across
515 different regions at different timescales.

516 Many important findings have been made by measuring the correlations between binned
517 spike counts, but there are some problems with this method of analysis. Firstly, the width
518 of the bins used to bin spike times into spike counts has an effect on the magnitude of the
519 correlations measured. Using a short bin width can cause your measurements to be artificially
520 small (Cohen and Kohn, 2011). This may not be an issue if one is considering relative size of
521 correlations when using the same bin width, but it is still not ideal. Secondly, while pairwise
522 correlations can capture most of the information in a small network (up to 40 cells) of highly
523 correlated cells (Schneidman et al., 2006), a model based on pairwise correlations alone will
524 fail to capture the activity of larger (~ 100 cells) networks, higher order correlated activity
525 is required (Ganmor, Segev, and Schneidman, 2011). One problem with these higher order
526 correlations is that they may be defined in different ways (Staude, Grün, and Rotter, 2010).
527 Furthermore if we want to include them in a model this usually involves greatly increasing the
528 number of parameters to fit, which increases the dimension of the parameter space leading

529 to the ‘curse of dimensionality’. Some models attempt to sidestep these problems while
530 still capturing higher-order correlations. These models attempt to capture the relationship
531 between each individual neuron in the ensemble, and the ensemble as a whole. Okun et al
532 (2015) called the strength of this relationship the ‘population coupling’, and demonstrated
533 that this quantity can predict an individual neuron’s response to optogenetic stimulation of
534 the whole ensemble. They also showed that this quantity was an indicator of the neuron’s
535 synaptic connectivity (Okun et al., 2015). With the ‘population tracking model’, O’Donnell
536 et al. (2016) linked the probability of firing an action potential for each individual neuron
537 with the distribution of the number of active neurons. This allowed model fitting for a large
538 number of neurons, as well as calculation of full pattern probabilities, and population entropy
539 (O’Donnell et al., 2017).

540 In this work, we also aimed to capture correlated behaviour between the neurons in a
541 neuronal ensemble without measuring correlations directly. Correlation coefficients capture
542 the linear component of the relationship between two random variables, but will not mea-
543 sure any relationship beyond linearity. Also, measuring correlation coefficients using short
544 timebins can be difficult for neuronal data (Cohen and Kohn, 2011). We decided to abandon
545 correlation, and we aimed to quantify a more general concept of association by modelling
546 the number of active neurons in the ensemble using a Conway-Maxwell-binomial (COMb)
547 distribution (Kadane, 2016).

548 The COMb distribution is a probability distribution over the number of successes in a
549 sequence of Bernoulli trials, where these trials can be associated in some way. The COMb
550 distribution is an extension of the standard binomial distribution, with an additional parameter
551 to model association between the Bernoulli variables. Using this additional parameter the
552 distribution can capture positive association, where the Bernoulli variables tend to take the
553 same value, negative association, where the Bernoulli variables tend to take opposite values,
554 or no association i.e. the standard binomial distribution.

555 We fit a COMb distribution to spike sorted electrophysiological data taken from five
556 different regions in the brain of an awake mouse exposed to visual stimuli (Steinmetz et al.,
557 2019). We examined whether or not a model based on the COMb distribution was able to
558 capture changes in the number of active neurons in these neuronal ensembles in response to
559 the stimuli. We also investigated the relationship between the changes as captured by the
560 COMb model and the change in neural variability as measured by Churchland et al. in their
561 famous paper (Churchland et al., 2010).

562 Our overall aim was to investigate some of the challenges in analysing large ensembles

563 of neurons present today. That included collecting the data to analyse (via calcium imaging),
564 and subsequently analysing these data. We felt that this was a worthwhile project because
565 the size of datasets, in terms of numbers of neurons and data collected, is growing rapidly.
566 Consequently these challenges will only become greater unless they are addressed. This is
567 our attempt at addressing them.

568 **Chapter 2**

569 **Sensitivity of the**
570 **spikes-to-fluorescence transform to**
571 **calcium indicator and neuron**
572 **properties**

573 *Abstract*

574 Fluorescent calcium indicators such as GCaMP are widely used to monitor neuronal activity.
575 However the relationship between the fluorescence signal and the underlying action potential
576 firing is poorly understood. This lack of knowledge makes it difficult for experimenters
577 to decide between different indicator variants for a given application. We addressed this
578 problem by studying a basic biophysical model of calcium dynamics in neuronal soma. We
579 fit the model parameters to publicly available data where GCaMP6s fluorescence and whole-
580 cell electrophysiological recordings were made simultaneously in the same single neurons.
581 We systematically varied the model's parameters to characterise the sensitivity of spike train
582 inference algorithms to the calcium indicator's main biophysical properties: binding rate,
583 dissociation rate, and molecular concentration. This model should have two potential uses:
584 experimental researchers may use it to help them select the optimal indicator for their desired
585 experiment; and computational researchers may use it to generate simulated data to aid design
586 of spike inference algorithms.

587

2.1 Introduction

588 Although fluorescent calcium indicators such as GCaMP are widely used to monitor neuronal
589 activity, the relationship between the fluorescence signal and the underlying action potential
590 firing is imperfect. The fluorescence signal has a low signal-to-noise ratio, and most indica-
591 tors' kinetics are slow relative to the millisecond-timescale dynamics of the membrane volt-
592 age (example in figure 2.1A). This makes spike inference difficult. Furthermore, the effects
593 of the indicator and cell properties on the fluorescence signal are unknown. For example,
594 genetically encoded indicators can accumulate within neurons over weeks and months (Chen
595 et al., 2013). Studies using calcium-sensitive fluorescent dyes have shown that indicator con-
596 centration has substantial effects on the spike-to-fluorescence relationship (Maravall et al.,
597 2000). Therefore spike rates inferred from GCaMP fluorescence signals may give mislead-
598 ing results if comparing across imaging sessions. More generally, the poor understanding of
599 the spike-to-fluorescence transform means experimenters may not know whether to trust the
600 outputs of spike train inference methods in any given application.

601 Spike trains are usually inferred from the time series of intensity values of one pixel of the
602 fluorescence image, where the pixel is located at the cell's soma. The problems of identifying
603 these pixels, and inferring spikes from their time series can solved separately or together.
604 When attempting to infer spikes, the fluorescence trace is modelled as a linear combination of
605 calcium concentration dynamics, a baseline calcium concentration, and some Gaussian noise.
606 The calcium concentration dynamics are modelled as an autoregressive process of degree 1
607 or 2 with a pulse input corresponding to the spike train, or the number of spikes fired in a
608 time step. The model includes no dynamics for the fluorescent indicator itself. Furthermore,
609 in order to make this model into an easily solvable linear programming problem the number
610 of spikes fired in a timestep is not restricted to non-negative integers but to arbitrary non-
611 negative values (Vogelstein et al., 2010; Pnevmatikakis et al., 2016; Friedrich and Paninski,
612 2016; Pnevmatikakis et al., 2013; Pnevmatikakis et al., 2014). More biologically inspired
613 spike inference models do exist (Deneux et al., 2016), but their fundamentals are very similar.
614 In this work, we investigated the effect of changing dynamics and buffer concentrations on
615 the accuracy of the inference algorithms based on these models.

616 The aim of this project was to model the fluorescence traces produced by a fluorescent
617 calcium indicator in a neuron soma resulting from a specific spike train, given calcium indi-
618 cator parameters such as binding rate, dissociation rate, and molecular concentration. Such

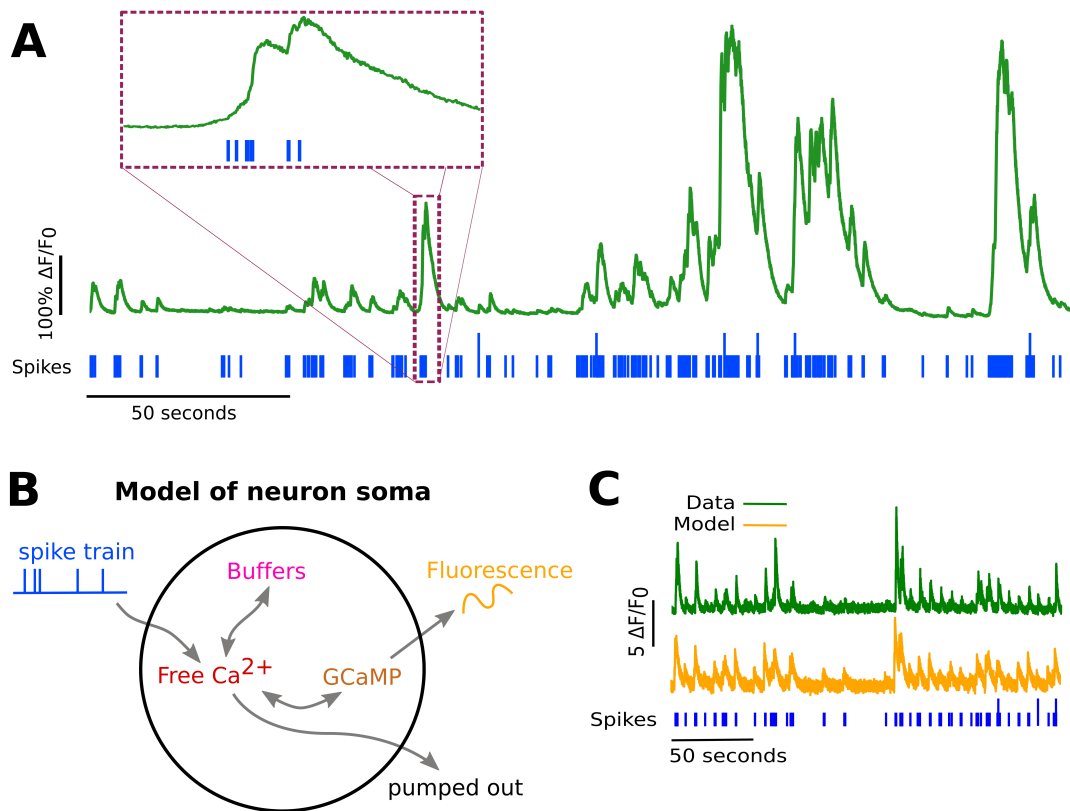


FIGURE 2.1:

A: Example spike train (blue) and the corresponding GCaMP6s fluorescence trace (green), data replotted from (Berens et al., 2018). Inset shows zoomed section of traces to highlight slow decay of GCaMP6s fluorescence relative to spike time intervals.

B: Schematic diagram of the neuron calcium and GCaMP computational model.

C: Good visual match of data fluorescence trace (green) and model simulated fluorescence (orange) in response to an identical spike train (blue).

619 a model would allow benchmarking of various spike inference algorithms, and enable under-
620 standing of how indicator characteristics affect the quality of spike train inference.

621 The model we developed consisted of free calcium, fluorescent indicator molecules, and
622 mobile and immobile endogenous calcium buffers. The indicator molecules which were
623 bound to a calcium molecule could be either excited, i.e. able to release a photon, or relaxed.
624 In order to reproduce the noise inherent in the data collection, we modelled the release of
625 photons from the excited indicator bound calcium as a stochastic process.

626 The fluorescence traces produced by the simulation were calibrated to reproduce the
627 signal-to-noise ratio observed in experimental data. Previously published spike inference
628 algorithms were then used to infer spike trains from the experimental fluorescence traces and
629 the modelled fluorescence traces. The parameters of the model were then varied in order to
630 determine the effect on the system dynamics and the effects on spike inference.

631 2.2 Methods

632 2.2.1 Calcium dynamics model

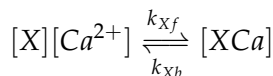
633 We wrote a biophysical model of the calcium dynamics within a cell soma. When a neu-
634 ron fires an action potential, voltage-dependent calcium ion-channels open up that allow a
635 current of Ca^{2+} to flow into the neuron (Koch, 1999). The increase in the free calcium ion
636 concentration inside of the cell, along with changes in the concentration of potassium and
637 sodium, causes the change in cell membrane potential, which must be depolarised. The de-
638 polarising process consists of free calcium ions leaving the cell through open ion channels,
639 or binding to molecules within the cell called buffers, or calcium storage by organelles such
640 as the endoplasmic reticulum. A diagram illustrating the cell, its channels, and its buffers
641 can be seen in figure 2.1A. There are several different types of calcium buffer, each with
642 different dynamics and different concentrations within different types of excitable cell. The
643 fluorescent calcium indicator is another calcium buffer, with the useful property that when it
644 is bound to a calcium ion, the bound molecule may become excited by a photon and release
645 a photon in return. This is what creates the fluorescence. After the action potential has taken
646 place, the free calcium concentration within the cell will return to a baseline level (Maravall
647 et al., 2000).

648 We modelled the the dynamics of five molecular concentrations,

- 649 • Free calcium ion concentration, $[\text{Ca}^{2+}]$

- 650 • Fluorescent indicator bound calcium, $[BCa]$
- 651 • Endogenous mobile buffer bound calcium, $[ECa]$
- 652 • Endogenous immobile buffer bound calcium, $[ImCa]$
- 653 • Excited buffered calcium, $[BCa^*]$

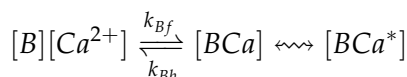
The term ‘buffering’ refers to free calcium ions coming into contact with buffer molecules and binding together. Diagrammatically:



654 where $[X]$ represents any buffer molecule, and k_{X_f} and k_{X_b} represent the binding and un-
 655 binding (dissociation) rates in units of per molar concentration per second ($M^{-1} s^{-1}$) and per
 656 second (s^{-1}) respectively. The speed of this chemical reaction is determined by the binding
 657 and unbinding rates.

658 There are a number different endogenous buffers in any neuron. Which buffers are
 659 present, and the buffers’ concentrations vary from cell to cell. In order to capture the ef-
 660 fects of mobile and immobile endogenous buffers without introducing several parameters,
 661 they were modelled as two buffers. One representing mobile buffers and the other represent-
 662 ing immobile buffers. Each with their own binding and unbinding rates.

The fluorescent calcium indicator behaves similarly to the other calcium buffers. The calcium is buffered by the indicator in the same way. But an indicator bound calcium molecule can become excited by absorbing the energy from a photon. An excited indicator bound calcium molecule can then release a photon to go back to its ‘relaxed’ state.



663 The released photons are captured by a photon collector. This gives us the fluorescence trace.
 664 Ignoring the baseline level of free calcium in a neuron, the system of equations we used
 665 to model all of these interactions is as follows:

$$\begin{aligned} \frac{d[Ca^{2+}]}{dt} = & k_{Bb}[BCa] + k_{Eb}[ECa] + k_{Imb}[ImCa] \\ & - k_{Bf}[B][Ca^{2+}] - k_{Ef}[E][Ca^{2+}] - k_{Imf}[Im][Ca^{2+}] \\ & + \beta([Ca_0^{2+}] - [Ca^{2+}]) \end{aligned} \quad (2.1)$$

$$\frac{d[BCa]}{dt} = k_{Bf}[B][Ca^{2+}] - k_{Bb}[BCa] + r[BCa^*] - \eta[BCa] \quad (2.2)$$

$$\frac{d[ECa]}{dt} = k_{Ef}[E][Ca^{2+}] - k_{Eb}[ECa] \quad (2.3)$$

$$\frac{d[ImCa]}{dt} = k_{Imf}[Im][Ca^{2+}] - k_{Imb}[ImCa] \quad (2.4)$$

$$\frac{d[BCa^*]}{dt} = \eta[BCa] - r[BCa^*] \quad (2.5)$$

666 where $[Ca_0^{2+}]$ is the baseline calcium concentration within the cell soma, β is a rate defining
667 how quickly free calcium enters or leaves the cell in the absence of an action potential, η
668 is the excitation rate for indicator bound calcium, r is the photon release rate for the excited
669 indicator bound calcium, and f and b are used to indicate the forward and backward rates
670 for chemical reactions respectively. The excitation rate defines the proportion of indicator
671 bound calcium that becomes excited at each time step. The photon release rate defines the
672 proportion of excited indicator bound calcium that releases a photon and returns to its relaxed
673 state at each time step. An action potential is modelled as a discontinuous increase in the free
674 calcium concentration to an appropriate value (Maravall et al., 2000).

675 Note that each of the three pairs of binding and unbinding terms in the first equation has a
676 corresponding pair in one of the subsequent three equations. Binding removes a free calcium
677 molecule and adds a bound calcium molecule, and unbinding does the opposite.

678 When using this model to simulate a fluorescence trace, the system of equations above are
679 first solved over a period of 25s without action potentials. This lets each of the five tracked
680 chemical concentrations reach their steady state. Then we use the given spike train and the
681 parameters to model the fluorescence trace.

682 Note that since the model has no spatial component, the mobile and immobile buffers
683 only differ in their binding and unbinding rates.

684 Photon release & capture

685 We used a simple model for the photon release. The number of photons released at each time
686 step was controlled by the number of excited indicator bound calcium molecules in the cell
687 and a parameter called the ‘release rate’. The release rate is an optimised free parameter of
688 the model.

689 As for the photon capture, in two-photon excitation microscopy the photons scattered
690 by the fluorescent indicator get scattered in all directions. Therefore the number of photons
691 detected is stochastic. This made the process for capturing photons the natural source of
692 noise in the system. The number of photons captured, and therefore the intensity of the

693 fluorescence, is modelled using a binomial distribution. The number of photons released was
694 used as the number of trials. The probability of success, or ‘capture rate’ was a free parameter
695 of the model that we optimised.

696 **2.2.2 Parameter optimisation**

697 The free parameters of the model are as follows:

698 **Calcium rate, β** Controls how quickly the concentration of free calcium will be driven to
699 the baseline concentration.

700 **Capture rate, p** The average proportion of photons captured by the photon detector.

701 **Excitation rate, η** The number of indicator bound calcium molecules that become excited
702 by photon bombardment at each time step.

703 **Release rate, r** The number of excited indicator bound calcium molecules that release a
704 photon at each time step.

705 To optimise the free parameters given a fluorescence trace, we applied the following proce-
706 dure:

- 707 1. The frequency power spectrum of the trace was measured.
- 708 2. The power spectrum was smoothed using a boxcar smoother (aka. sliding average, box
709 smoother).
- 710 3. The log of the smoothed power spectrum was measured.
- 711 4. Use the model to create a modelled fluorescence trace.
- 712 5. Apply steps 1, 2, and 3 to the modelled fluorescence trace.
- 713 6. Calculate the root mean squared difference between the log power of the actual fluo-
714 rescence trace, and the log power of the modelled fluorescence trace.
- 715 7. Calculate the root mean squared difference between the actual fluorescence trace and
716 the modelled fluorescence trace.
- 717 8. Use an optimisation algorithm to reapply this process, attempting to minimize the sum
718 of the two root mean squared differences at each iteration.

719 Using the root mean squared difference of the log power spectra as part of the objective
720 function forces the model to match the noise frequency of the actual fluorescence. Using
721 the root mean squared difference of the traces themselves forces the model to match the
722 amplitude of the fluorescence trace more accurately.

723 In order to minimise the objective function, a suite of meta-heuristic optimisation (aka.
724 black-box optimisation) algorithms were implemented on each of the traces in the dataset.
725 These methods were chosen because they don't require a gradient for the objective function
726 (gradient-free) and they are particularly useful for minimising stochastic objective functions
727 like the one we used here. The free parameters were optimised for each individual fluores-
728 cence trace. The most successful method for each trace was recorded. The method that was
729 most often successful was probabilistic descent, and the second most successful method was
730 generating set search. Both of these methods are examples of pattern search. These two
731 methods were the best optimisers on about 75% of the traces in the dataset.

732 Although this optimisation procedure minimises the value of the optimisation function,
733 the value never reaches zero for a number of reasons. Firstly, the fluorescence traces carry low
734 frequency fluctuations that cannot be captured by the model. Secondly, the model assumes
735 that the process of calcium binding to the fluorescent indicator is linear in time (see equation
736 1), but there are more complicated dynamics involved here. Fluorescent calcium indicators
737 are often built upon the calcium binding protein called 'calmodulin'. This protein has four
738 calcium binding sites. These sites are locally split into two pairs. Each pair has a different
739 affinity for calcium, and the affinity of the binding sites is affected by the occupancy of
740 the other binding sites (Kilhoffer et al., 1992). So the calcium to calcium indicator binding
741 process is non-linear, but the model does not take this into account.

742 **Fixed parameters**

743 As well as the optimised parameters mentioned in section 2.2.2, the model also has thirteen
744 fixed parameters. Please see table 2.1 for details of these parameters and their values. In
745 an application of the model, these parameters can be changed in order to model any given
746 fluorescent calcium indicator.

747 **2.2.3 Julia**

748 The programming language used to write and execute the model was 'Julia'. Julia is a dy-
749 namic programming language designed for technical computing. Julia was designed specif-
750 ically to provide a convenient high-level dynamic language similar to MATLAB, or Python,

Parameter	Description	Value	Source
baseline	The baseline concentration of free calcium within the cell soma	$4.5 \times 10^{-8} M$	(Maravall et al., 2000)
cell radius	The radius of the soma (assumed to be spherical)	$10^{-5} M$	(Fiala and Harris, 1999)
endogenous	The concentration of endogenous mobile buffer within the cell soma	$10^{-4} M$	(Faas et al., 2011)
frequency	The frequency at which the spike trains are sampled.	100Hz	
immobile	The concentration of endogenous immobile buffer within the cell soma	$7.87 \times 10^{-5} M$	(Bartol et al., 2015)
indicator	The concentration of fluorescent indicator within the cell soma	$10^{-4} M$	(Maravall et al., 2000)
k_{Bb}	The unbinding rate of the fluorescent calcium indicator	$160 s^{-1}$	(Bartol et al., 2015)
k_{Bf}	The binding rate of the fluorescent calcium indicator	$7.77 \times 10^8 s^{-1} M^{-1}$	(Bartol et al., 2015)
k_{Eb}	The unbinding rate of the endogenous mobile buffer	$10^4 s^{-1}$	(Bartol et al., 2015)
k_{ef}	The binding rate of the endogenous mobile buffer	$10^8 s^{-1} M^{-1}$	(Bartol et al., 2015)
k_{Imb}	The unbinding rate of the endogenous immobile buffer	$524 s^{-1}$	(Bartol et al., 2015)
k_{Imf}	The binding rate of the endogenous immobile buffer	$2.47 \times 10^8 s^{-1} M^{-1}$	(Bartol et al., 2015)
peak	The increase in free calcium concentration within the cell induced by an action potential	$2.9 \times 10^{-7} M$	(Maravall et al., 2000)

TABLE 2.1: **Fixed parameters** A table of the parameters fixed before optimising the model. The values of these parameters could be changed to model different fluorescent calcium indicators.

751 with improved performance. Julia’s type system and Julia’s direct interfaces with C and
752 Fortran allow this aim to be achieved (Bezanson et al., 2012). The Julia version of the
753 ‘Sundials’ package for ODE solving was used to solve the system of equations above. The
754 BlackBoxOptim.jl package for Julia was used to perform the optimisation.

755 **2.2.4 Spike inference**

756 We used spike inference algorithms to compare the quality of spike inference using the mod-
757 elled traces to the quality of spike inference using the observed traces. We also used the
758 spike inference algorithms to assess the effect of parameter perturbation on the spike infer-
759 ence. Three algorithms were used:

760 **Constrained non-negative deconvolution algorithm (aka Pnevmatikakis algorithm)** This
761 algorithm uses a constrained version of non-negative Weiner deconvolution to infer a
762 calcium signal and a ‘spiking activity signal’ from the fluorescence trace (Vogelstein
763 et al., 2010; Pnevmatikakis et al., 2016). The spiking activity signal is a non-negative
764 vector of real numbers reflecting the cell’s activity rather than an actual spike train. We
765 inferred a spike train by choosing an optimised threshold for the spiking activity sig-
766 nal. Whenever the spiking activity signal exceeded that threshold, an action potential
767 was inferred. The threshold was optimised by minimising the difference between the
768 number of spikes observed and the number of spikes predicted.

769 **ML-Spike algorithm** This algorithm uses a generalised version of the Viterbi algorithm to
770 return the spike train that maximises the likelihood of producing the given fluorescence
771 trace. The Viterbi algorithm is an algorithm for estimating the most likely sequence
772 of hidden states resulting in a sequence of observed states in a discrete-time finite-
773 state Markov process (Forney, 1973). In this case, each hidden state is defined by the
774 presence or absence of an action potential, and each observed state is the value of the
775 fluorescence trace at each time step. This algorithm assumes that the concentration of
776 calcium within the cell will decay to a drifting baseline, rather than a fixed baseline
777 (Deneux et al., 2016).

778 **Online Active Set method to Infer Spikes (OASIS)** This algorithm is once again based on
779 an auto-regressive model of the fluorescence trace, but can be generalised to any or-
780 der. The algorithm itself is a generalisation of the pool adjacent violators algorithm
781 (PAVA) that is used in isotonic regression. The OASIS algorithm works through the

782 fluorescence trace from beginning to end, this combined with the speed of the algo-
783 rithm means that it could be used for real-time online spike inference (Friedrich and
784 Paninski, 2016). Given a fluorescence trace, the algorithm will return the most likely
785 spike train and an inferred denoised fluorescence signal.

786 In order to quantify the quality of spike inference for a given algorithm, we ran that algorithm
787 on all of the fluorescence traces in dataset number eight of the spike finder datasets. Then we
788 measured some binary classification measures on the results. These measures included

- 789 • Accuracy
- 790 • True positive rate (aka recall, sensitivity, hit rate)
- 791 • True negative rate (aka specificity)
- 792 • Precision
- 793 • Negative predicted value
- 794 • False negative rate (aka miss rate)
- 795 • False positive rate (aka fall-out)
- 796 • False discovery rate
- 797 • False omission rate

798 In making these measurements, we allowed a tolerance of two subsequent time bins for spike
799 prediction. For example, the spike train data is a vector of 0s and 1s, with one element for
800 each time bin. A ‘0’ denotes inactivity, a ‘1’ denotes the presence of at least one action
801 potential. The inferred spike trains produced by the spike inference algorithms take the same
802 form. In our analysis, if a spike appeared in the inferred spike train up to two time frames
803 after a spike in the observed spike train, that spike was considered correctly inferred i.e. a true
804 positive. However, once a spike in the inferred spike train was matched to a spike from the
805 observed spike train, the inferred spike could not be matched to another observed spike. To
806 illustrate, if two spikes were inferred in the two time bins following an isolated observed
807 spike, the first inferred spike was considered correctly inferred, but the second inferred spike
808 was considered incorrectly inferred, i.e. a false positive.

809 The most useful measure was the true positive rate. This is because the spiking is sparse
810 and this measurement is sensitive to the number of spikes observed and inferred, but is not
811 affected by the true negative or false negative rates. After optimising the parameters for each

812 fluorescence trace we measured the spike inference quality for the observed fluorescence
813 traces, and compared this to the spike inference quality for the modelled traces.

814 When measuring the spike inference quality for higher frequency spike train (1 – 10Hz),
815 we used the accuracy as our binary classification measure. At these frequencies the variance
816 of the fluorescence trace was much higher than for sparser spiking regimes, therefore we
817 wanted to take into account the number of false negatives inferred by the algorithm.

818 **Comparing spike inference quality**

819 In order to compare spike inference quality we had to use methods for comparing samples.
820 When comparing the true positive rate distributions arising from two different datasets, or
821 two different algorithms on the same dataset, we compared the distributions using a paired
822 t-test.

823 **2.2.5 Perturbation analysis**

824 In order to measure the sensitivity of spike inference to changes in a given model parameter,
825 we perturbed the parameter and compared the quality of spike inference with the perturbed
826 parameters to the quality of spike inference with the experimental or optimised parameters.
827 In order to maximise the possibility of observing a difference due to the perturbation, we
828 perturbed the chosen parameter by a relatively large amount. For example, the experimen-
829 tal value for the molar concentration of the fluorescent indicator within the cell was 10^{-4}M
830 (Maravall et al., 2000). The perturbed values used for this parameter were 10^{-2}M , 10^{-3}M ,
831 10^{-5}M , and 10^{-6}M . The quality of the inference was compared by measuring the true posi-
832 tive rate for each perturbed value and using a t-test to compare the distributions of the results.

833 This analysis was performed firstly without any optimisation of the free parameters for
834 use with the perturbed parameters. Then the analysis was performed after the optimised
835 parameters for each perturbed value were calculated.

836 **2.2.6 Signal-to-noise ratio**

837 To assess the effect of perturbation on the modelled traces, we measured and compared the
838 signal to noise ratio (SNR) on each of the modelled traces. We calculated the SNR as the
839 peak change in fluorescence divided by the standard deviation of the baseline fluctuation of
840 the fluorescence trace (Tada et al., 2014). We measured these values by running the model
841 on a spike train consisting a long period of inactivity followed by one action potential. We
842 ran the model on this spike train one hundred times. We then measured the mean change

843 in fluorescence and standard deviation of baseline activity across the one hundred modelled
 844 fluorescence traces, and calculated the SNR.

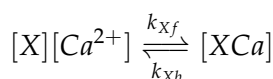
845 **2.2.7 Data sources**

846 All of the data used in this project was sourced from the ‘Spike Finder’ project (spikefinder.codeneuro.org).
 847 The data consisted of a collection of datasets with simultaneously measured fluorescence
 848 traces and action potentials (Berens et al., 2018).

849 **2.3 Results**

850 **2.3.1 A biophysical computational model can generate accurate fluorescence
 851 traces from spike trains**

To study the relationship between action potential firing and calcium fluorescence, we built a computational model of calcium dynamics in a neuronal soma. The model consisted of four dynamic variables: the concentration of free calcium, two types of endogenous buffer, and the calcium-sensitive fluorescent indicator. Each of the buffers and the indicator could independently bind and unbind with calcium. These reactions were modelled as



852 where X is the buffer concentration and Ca^{2+} is the calcium concentration. Each species
 853 could therefore exist in two states: either bound with calcium or unbound. To model the
 854 imaging process, we also added a third, excited state to the indicator. When in the calcium-
 855 bound state, the indicator could be converted to an excited state, corresponding to the absorp-
 856 tion of a photon. The rate of this excitation process could be interpreted as the intensity of
 857 the light illuminating the sample. Once excited, the species decayed back to the unexcited
 858 state at a fixed rate, corresponding to the spontaneous emission of photons. The total emitted
 859 fluorescence signal was interpreted as proportional to this de-excitation flux. To represent
 860 experimental noise in the photon capture process, we drew a random number of captured
 861 photons at each time step from a binomial distribution, parameterised by a number p that
 862 corresponds to the mean fraction of released photons that are captured.

863 The model had 17 parameters in total describing the molecules’ concentrations and re-
 864 action rates (Methods). We set 13 of these parameters to values from the literature. The
 865 remaining 4 parameter values we fit to publicly-available data (Berens et al., 2018), briefly

explained as follows (see Methods for full details). Single neurons from acute rat cortical slices expressing GCaMP6f were imaged with two-photon microscopy while the membrane potentials of the somata of the same neurons were simultaneously recorded via whole-cell patch clamp electrophysiology. In this dataset, the electrical recordings give unambiguous information about neurons' spike times. To do the parameter fitting, we feed these spike trains as inputs to the computational model. After running, the model returns a simulated fluorescence trace. We aimed to find the model parameter values that give the best match between this simulated fluorescence trace and the real fluorescence time series recorded in the corresponding neuron. To do this we used a suite of optimisation procedures to jointly fit both the real neuron's fluorescence time series and power spectrum, which capture complementary information about the spikes-to-fluorescence mapping (Methods). We performed the fitting procedure independently for each of the 20 neurons in the spikefinder dataset (<http://spikefinder.org>). After fitting, the model produced realistic-looking fluorescence time series (Figure 2.1).

2.3.2 Spike inference algorithms perform similarly on real data compared with
time series simulated from the model

Researchers often pass the fluorescence time series through a spike inference tool before performing further statistical analyses. These spike inference algorithms take the fluorescence trace as input and attempt to estimate the neuronal spike train that triggered them (Vogelstein et al., 2010; Pnevmatikakis et al., 2016; Friedrich and Paninski, 2016; Pnevmatikakis et al., 2013; Pnevmatikakis et al., 2014; Deneux et al., 2016). Part of our motivation for building this model was to allow us to ask the question: how do the properties of the cell and the calcium indicator affect the quality of spike inference? In order to trust the conclusions from our model, we should first be confident that spike inference from our simulated fluorescence traces is similar to that from the real data. To test this we passed each of the simulated fluorescence traces through three previously published spike inference algorithms, quantified their performance against the ground-truth electrophysiology data, repeated the procedure for the real calcium fluorescence time series, and compared the accuracy of the inference processes in all cases. The *true positive rate*, also known as the *recall*, the *sensitivity*, or the *probability of detection* of spike inference varied across the three inference algorithms we tried (p-value and statistical test here). The constrained non-negative matrix deconvolution algorithm (Pnevmatikakis et al., 2016) (CNMD algorithm) correctly detected approximately 45% of the

898 true spikes, the OASIS algorithm (Friedrich and Paninski, 2016) correctly detected approx-
 899 imately 35% of the true spikes, and the ML spike algorithm (Deneux et al., 2016) correctly
 900 detected approximately 15% of the true spikes (see figure 2.2). Notably, for two of the three
 901 inference algorithms, the quality of inference was also fairly consistent for individual spike
 902 trains, not just the group means ($p > 0.05$, paired t-test). This demonstrates that the models
 903 were generating fluorescence time series that were similarly difficult to decode as the real
 904 data, in ways that were not specific to any one inference algorithm. This is evidence that the
 models captured real aspects of the spikes-to-fluorescence transform.

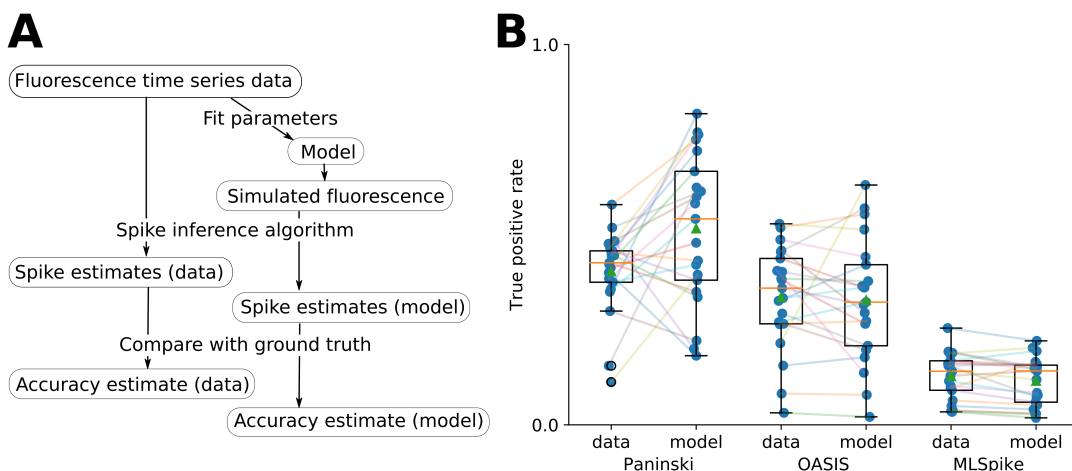


FIGURE 2.2:
 A: Workflow to compare spike inference for real versus simulated fluorescence data.
 B: True positive rates achieved by three different spike inference algorithms when applied to observed spike trains, and simulated spike trains. Data points overlaid as blue circles. The performance is similar from real and simulated data for each of the algorithms.

905

906 2.3.3 Relative effects of various buffers to the fluorescence signal

907 One of the benefits of computational models over laboratory experiments is that we can
 908 observe all the variables in the simulation to gain insight into the system's dynamics, which
 909 can be difficult to do in the lab. We plotted the concentrations of the various species over
 910 time for a version of the model fit to one data set, in response to the same train of spikes used
 911 for fitting (figure 2.3). Figure 2.3a shows the absolute values of the species concentrations,
 912 summed. Consistent with experimental estimates (Maravall et al., 2000), only a small fraction
 913 ($\sim 0.1\%$) of calcium is free and unbound to any buffer. Of the bound calcium, the vast
 914 majority, ($\sim 96\%$) is bound to the GCaMP indicator. The two types of endogenous buffer

915 are bound to the remaining calcium ($\sim 4\%$). An influx of calcium from a single spike adds
916 very little to the total calcium, in relative terms (red line in Figure 3a).

917 When calcium entered the model neuron it was rapidly buffered (Bartol et al., 2015).
918 However the relative fractions of which buffer molecules bound to the influxed calcium was
919 dynamic, and changed over time. Figure 2.3 (b-f) shows the time course of the various
920 species over time in response to a calcium influx event from a single action potential. Cru-
921 cially, the indicator $[BCa]$ competed with the endogenous buffers $[ImCa]$ and $[ECa]$ – all
922 three bind calcium on similar timescales. This implies that the timecourse and amplitude of
923 the $[BCa]$ variable will also depend on the binding rates and availabilities of the endogenous
924 buffers. For example if we decreased the concentration of an endogenous buffer, we might
925 expect both a faster rise time and greater peak amplitude of the $[BCa]$ signal in response to
926 a calcium influx event. The slowest component of the decay had a similar time constant for
927 $[BCa]$, $[ImCa]$ and $[ECa]$, which in turn matched the $[Ca]$ extrusion time constant in our
928 model ($\sim 6.29 \times 10^{-22} \text{Ms}^{-1}$). This implies that the buffers and the indicator had reached
929 a dynamic equilibrium and were jointly tracking the free calcium concentration as calcium
930 was slowly extruded from the cell.

931 Interestingly the excited bound calcium species ($[BCa^*]$) showed a qualitatively different
932 timecourse in response to a calcium influx event. This concentration is subject to the added
933 ‘excitation and release’ dynamic, where a certain proportion of the concentration absorbs the
934 energy from an incoming photon and goes into an ‘excited state’ at each time step. A certain
935 proportion of the concentration releases a photon and reverts to a ‘relaxed state’ at each
936 timestep also. This means that the excited bound calcium lags behind the bound calcium
937 trace. We could think of the excited bound calcium trace as a low pass filtered version of the
938 bound calcium trace.

939 **2.3.4 Spike inference accuracy is sensitive to indicator properties, and likely
940 varies within and between cells**

941 The above results imply that the fluorescence signal depends on the relative properties of
942 both GCaMP and the endogenous buffers. We next used the model to directly ask how
943 sensitive spike inference was to these components. We focused on three key parameters that
944 likely vary from cell to cell and experiment to experiment: GCaMP binding kinetics, GCaMP
945 concentration, and endogenous buffer concentration.

946 Several variants of GCaMP itself have been made that differ in calcium binding kinetics,
947 baseline fluorescence, fluorescence efficiency, and other factors. For example, GCaMP6f has

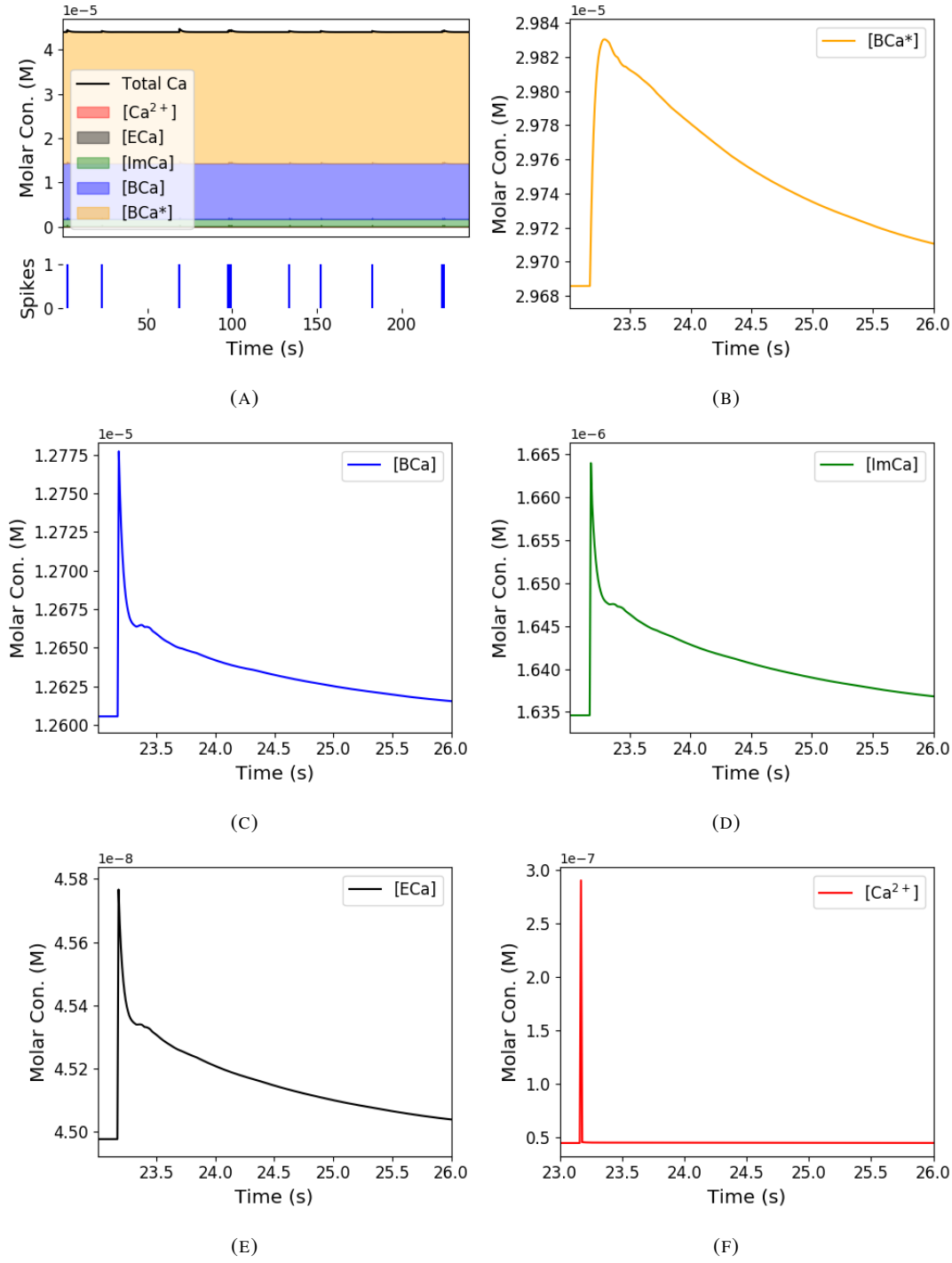


FIGURE 2.3: Calcium Buffering Dynamics (a) The proportions of bound and free calcium concentrations within a cell, with the associated spike train. (b)-(f) The dynamics of the concentration of (b) excited indicator bound calcium, (c) indicator bound calcium, (d) immobile endogenous buffer bound calcium, (e) mobile endogenous buffer bound calcium, and (f) free calcium in response to an action potential at ~ 23.2 s.

948 a decay time constant of ~ 1 s, while GCaMP6s has a decay time constant of ~ 2 s (Chen
949 et al., 2013). Here we asked how these differences in binding kinetics affect spike inference.
950 We jointly varied the calcium binding and unbinding rates of the indicator by the same factor
951 over a range from 100-fold slower to 100-fold faster from the fitted values, and simulated the
952 fluorescence response for each of the parameter settings in response to the same spike trains
953 as before (figure 2.4). Notably this manipulation does not affect the indicators affinity, and
954 therefore would not affect steady-state responses to prolonged changes in calcium. Instead
955 it is likely to affect its sensitivity to the spike train dynamics. We computed two summary
956 measures from the simulated fluorescence traces: the signal-to-noise ratio for a single spike
957 (Methods, section 2.2.6), and the accuracy of spike inference for each of the spike trains. We
958 observed a reduction in the signal-to-noise ratio and the spike inference quality when we set
959 the binding and unbinding rates were set to one hundredth of their fitted values, and to one
960 tenth of their fitted values. When we increased the value of both binding rates, we observed
961 no change in these measurements. The reduction in both rates lead to smaller increases in
962 fluorescence in response to an action potential and a longer decay time (figure 2.4a), this
963 caused the reduction in signal-to-noise ratio. As both rates were increased, the change in
964 $\Delta F/F_0$ in response to an action potential increased and the decay time decreased slightly,
965 but the fluorescence trace created by these values was very similar to the trace created by the
966 fitted values.

967 Second, the overall concentrations of GCaMP often varies from cell to cell. For exam-
968 ple different cells, even of the same type in the same tissue, can express different levels of
969 GCaMP, due to proximity to the infection site, or the cell becoming ‘nuclear-filled’ (Tian et
970 al., 2009; Chen et al., 2013). Also, GCaMP is often used for longitudinal experiments where
971 the same cells are re-imaged across multiple days or weeks. However since GCaMP expres-
972 sion typically ramps up over time (Chen et al., 2013), the accuracy of spike inference may
973 differ across multiple longitudinal recordings in the same cell. We addressed this by varying
974 the concentration of calcium indicator in the model, simulating spike trains and measuring
975 signal-to-noise ratio and spike inference accuracy on the resulting fluorescence traces. Both
976 increasing and decreasing the concentration of the indicator had effects on the fluorescence
977 trace, signal-to-noise ratio, and spike inference. The signal-to-noise ratio and spike inference
978 quality decreased with decreased indicator concentration, and both showed a decrease when
979 the indicator concentration was increased to 100 times its fitted value (figure 2.5). The signal-
980 to-noise ratio showed an increase when the indicator concentration was increased to 10 times
981 its fitted value, but there was no corresponding change in the spike inference quality. The

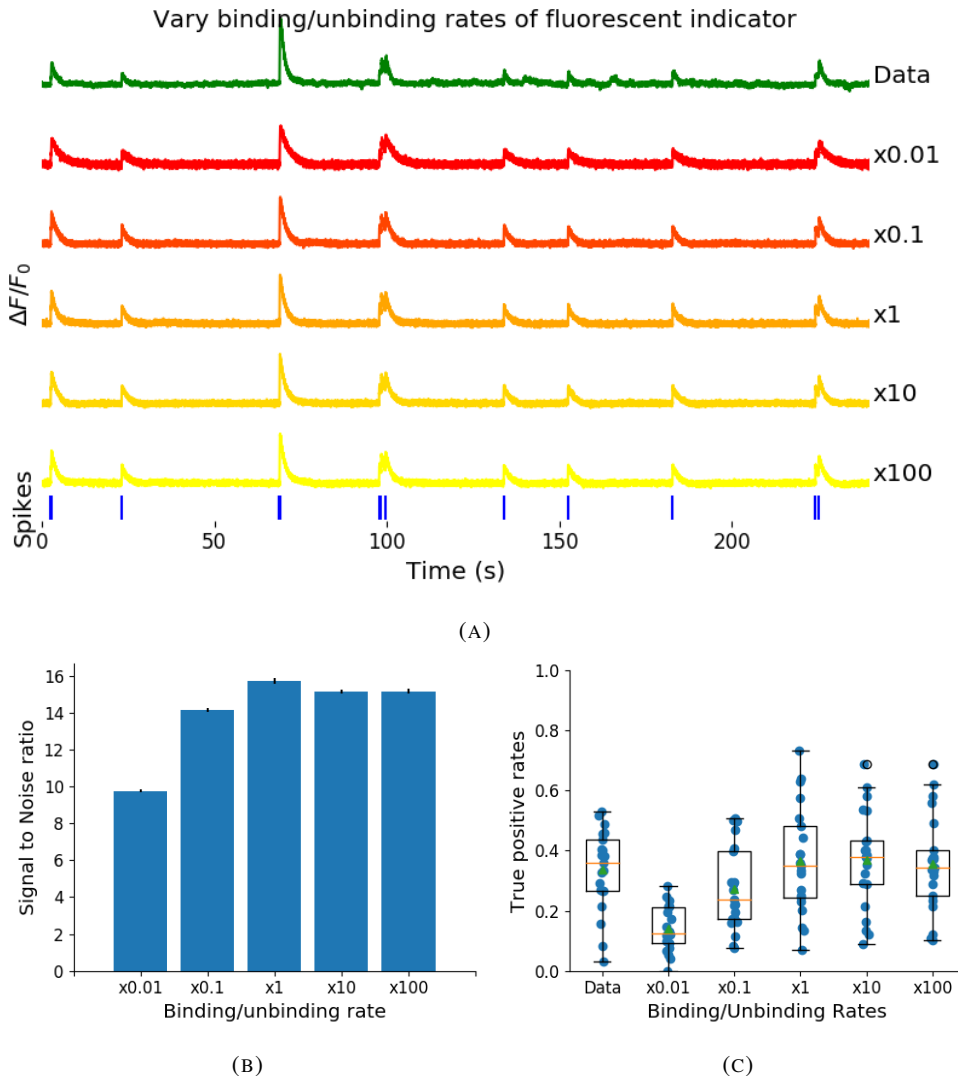


FIGURE 2.4: (a) An example trace for each of the five pairs of values used for the binding and unbinding rates of the fluorescent calcium indicator. (b) The signal-to-noise ratio of the modelled fluorescence traces using each of the four perturbed value pairs, and the experimental value. The SNRs for the value pairs perturbed downward are lower than that for the unperturbed value pair or the higher value pairs. (c) The true-positive rates of the deconvolution algorithm's predictions when inferring from the observed data, and inferring from modelled traces using the perturbed and experimental values.

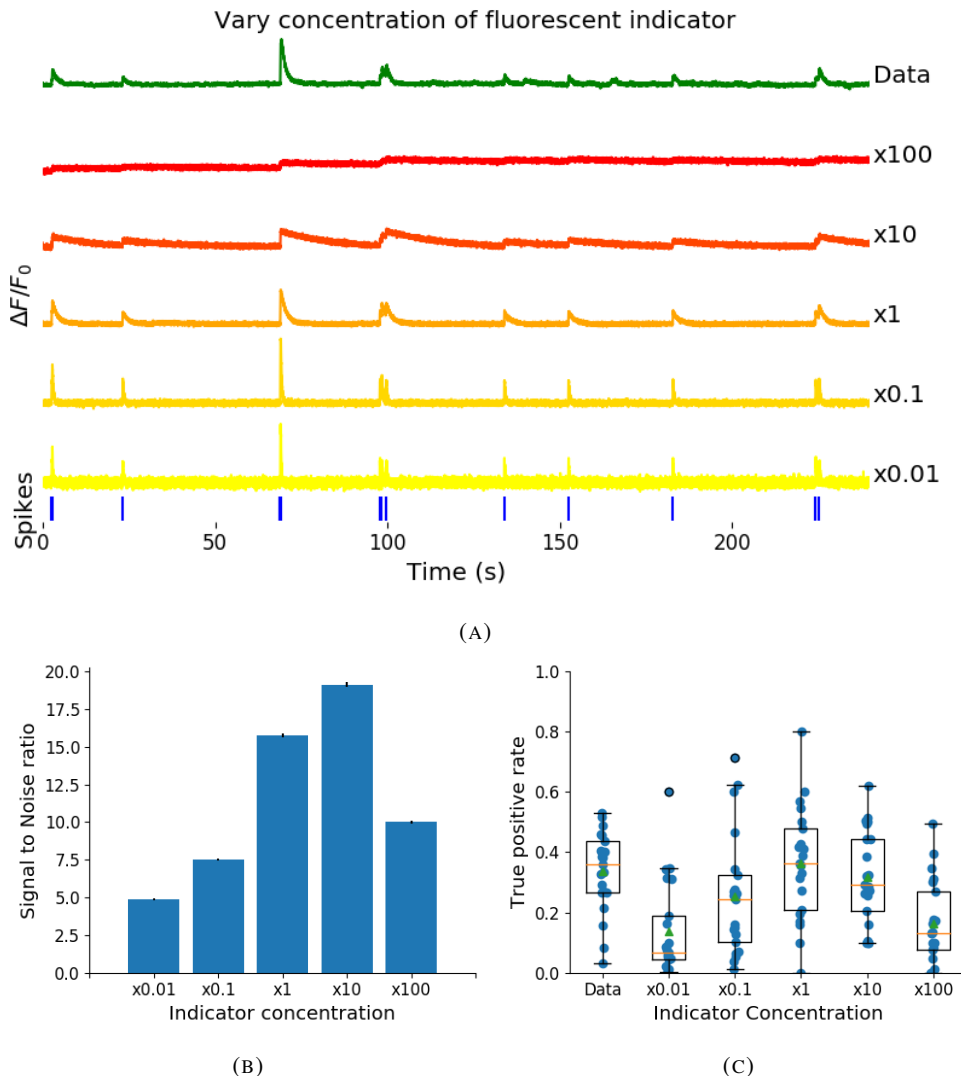


FIGURE 2.5: (a) An example trace for each of the five perturbed values for the concentration of fluorescent calcium indicator. The top two traces are produced by the lower perturbed values, the middle trace is produced by the experimental value, and the lowest two traces are produced when using the higher perturbed values. (b) The signal-to-noise ratio of the modelled fluorescence traces using each of the four perturbed values, and the experimental value. Extreme perturbations of the concentration either above or below the experimental level lowered the SNR. (c) The true-positive rates of the deconvolution algorithm's predictions when inferring from the observed data, and inferring from modelled traces using the perturbed and experimental values. We found that the algorithms performs equally badly on the two most extreme values, and performs equally well on the experimental value, and the next higher perturbed value.

decrease in indicator concentration caused a reduction in the increase in $\Delta F / F_0$ in response to an action potential, and an increase in the decay time of this increase (figure 2.5a). The increase in indicator concentration had the opposite effect, it caused an increase in the change in $\Delta F / F_0$ in response to an action potential, and a decrease in the decay time.

Third, the concentration and types of endogenous calcium buffers also vary from neuron to neuron, both within and between cell types (Bartol et al., 2015; Maravall et al., 2000; Neher and Augustine, 1992). Since the calcium buffer capacity of neurons is high, around 50-70 (Lee et al., 2000) in excitatory hippocampal pyramidal cells, around 100-250 (Lee et al., 2000) in inhibitory hippocampal pyramidal cells, and 900-200 in Purkinje cells (depending on the age of the subject), these endogenous buffers compete with GCaMP for binding to calcium, and variations in endogenous buffer concentration may affect GCaMP signal and therefore spike inference. To address this we varied the concentration of the endogenous buffer in the model neuron over five orders of magnitude from 0.8 to 8000 μM , simulated calcium fluorescence traces in response to the same set of spike trains, and performed spike inference on the resulting fluorescence time series. Increasing the endogenous buffer concentration had a substantial effect on the GCaMP fluorescence signal, both decreasing its amplitude and slowing its kinetics (figure 2.6(a)). This corresponded with a decrease in both single-spike signal-to-noise ratio (figure 2.6(b)) and spike inference accuracy (figure 2.6(c)). In contrast, decreasing endogenous buffer capacity from the fitted value had little effect on either the GCaMP signal or spike inference (figure 2.6).

2.3.5 Single spike inference accuracy drops for high firing rates, but firing rate itself can be estimated from mean fluorescence amplitude

The fluorescence signal recorded from neurons using calcium indicators is typically much slower than changes in membrane potential for two reasons: first, because the calcium and the indicator have slow binding and unbinding kinetics, the signal is a low-pass filtered version of the membrane potential. Second, neuronal two-photon imaging experiments are often performed in scanning mode, which limits their frame rate to $\sim 10\text{Hz}$ or slower. This implies that multiple spike events that occur close in time might be difficult to resolve from a calcium indicator time series. Many cells, especially several types of inhibitory interneurons, fire tonically at rates higher than 10Hz. We used the model to test whether spike inference accuracy depended on the neuron's firing frequency by driving the cell with spike trains sampled from a Poisson processes of varying frequency. We simulated a variable firing rate using an Ornstein-Uhlenbeck process, and simulated the spike trains using a Poisson distribution

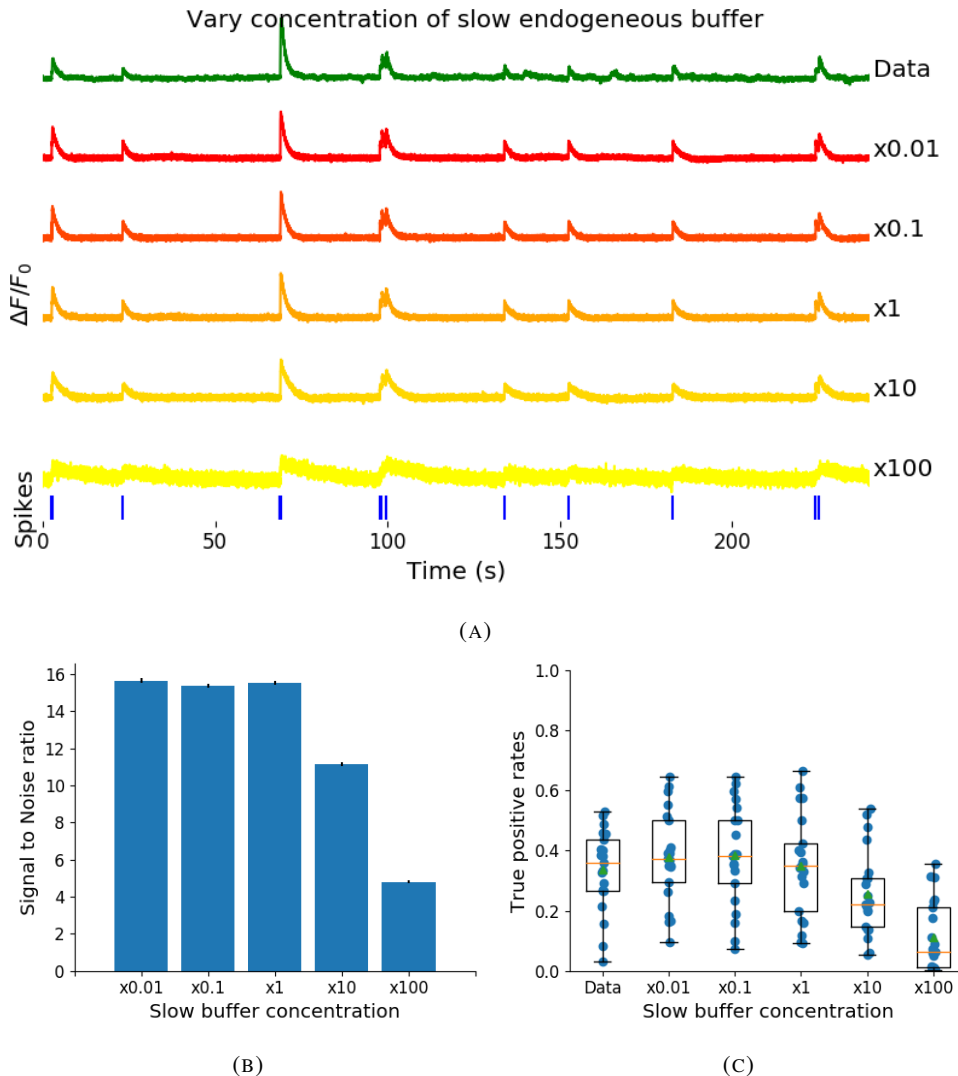


FIGURE 2.6: (a) An example trace for each of the five perturbed values for the concentration of immobile endogenous buffer. (b) The signal-to-noise ratio of the modelled fluorescence traces using each of the four perturbed values, and the experimental value. The lower values for the immobile buffer produce the same SNR as the experimental value. But the higher perturbed values produce fluorescence traces with a lower SNR. (c) The true-positive rates of the deconvolution algorithm's predictions when inferring from the observed data, and inferring from modelled traces using the perturbed and experimental values.

with its rate taken from this process. Because of the high frequency firing rate of these spike trains, we used the accuracy as the measure of spike inference quality. We simulated 30 spike trains at average firing rate of 1, 5, and 10Hz, and measured the spike inference quality of all these traces. Spike inference accuracy decreased with increasing firing rate, for up to 10Hz Poisson spike trains (figure 2.8(left)). Although the accuracy remained above 90% for each of the three frequencies. We also plotted the average $\Delta F/F_0$ as a function of stimulation firing rate. We found that it increased monotonically as a function of firing rate (figure 2.8(right)).

We expected lower spike inference quality as the average spiking frequency increased. Since the fluorescence trace, in some sense, is a low pass filtered version of the spike train, a tightly packed groups of spikes will be more difficult to infer than isolated spikes. However, the increasing amplitude of the fluorescence trace with increasing frequency suggests that some spike inference algorithm could be developed based on this amplitude.

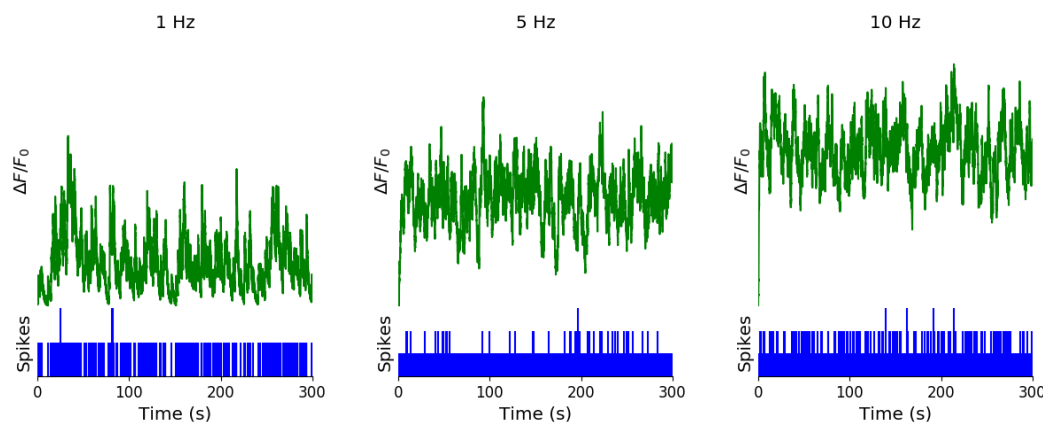


FIGURE 2.7: Simulating fluorescence traces at different firing rates Example modelled traces created using simulated spike trains with a mean firing rate of 1Hz (left column), 5Hz (middle column), and 10Hz (right column). Note the difference in amplitude with different mean firing rates.

2.4 Discussion

We designed a biophysical model for the changes in free calcium and bound calcium concentrations within a cell soma with a fluorescent calcium indicator. We used this model to model the fluorescence trace resulting from a spike train in this cell. We fit the free parameters of the model by matching the power spectrum and amplitude of fluorescence traces with simultaneously measured spike trains. We inferred spikes from real fluorescence traces and modelled fluorescence traces, and measured the quality of the spike inference in both cases.

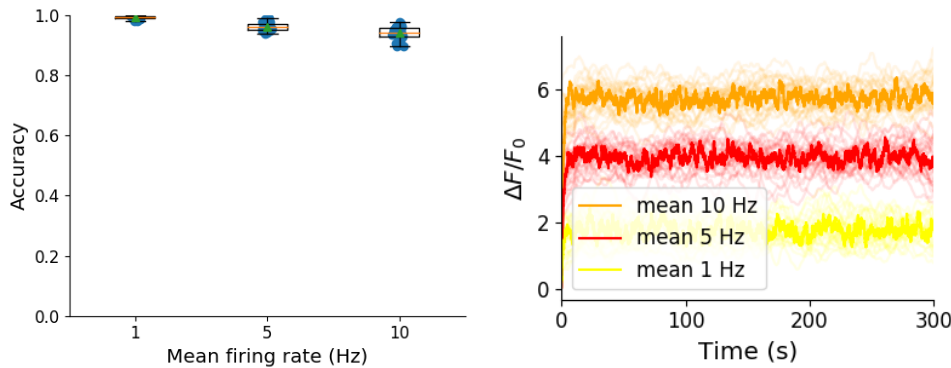


FIGURE 2.8: **Inference quality and $\Delta F/F_0$ vs Firing rate** (left) The spike inference accuracy when applied to 30 traces created using simulated spike trains with mean firing rates of 1, 5, and 10 Hz. (right) The mean $\Delta F/F_0$ across those 30 traces for each frequency.

1035 We found that the spike inference quality was similar in both cases. We perturbed the concentration of the calcium buffers in the model, and the binding/unbinding rates of those buffers
 1036 in the model, and measured the effect on the signal-to-noise ratio (SNR) of the modelled
 1037 fluorescence traces and the spike inference quality.
 1038

1039 For the fluorescent calcium indicator, we found that any large perturbation away from
 1040 the taken from the literature led to a reduction in SNR, and spike inference quality. For the
 1041 binding/unbinding rates, we kept the ratio of these rates constant, but altered their values in
 1042 parallel. The lower values caused a reduction in SNR, and a reduction in spike inference
 1043 quality. For the endogenous buffer concentration, an increase above the experimental value
 1044 caused a reduction in SNR and spike inference quality.

1045 Although the model produced visually similar time series to the real data, there were a
 1046 few aspects it did not capture. First, the real data featured some low-frequency components
 1047 that did not appear related to the spike events. These were not captured by the models we
 1048 used in this study, but could be added in future by adding a suitable low-frequency term to the
 1049 resulting time series. Second, the real data seemed to have some non-linearities not captured
 1050 in the model, for example the response to two nearby spikes was greater than expected from
 1051 the linear sum of two single spikes. This may be due to the co-operative binding of calmod-
 1052 ulin to calcium, which gives calmodulin a supra-linear sensitivity to calcium concentration
 1053 (Faas et al., 2011). The non-linear dynamics of this binding have been included in a recently
 1054 developed spike inference model (Greenberg et al., 2018). Our model, in contrast, behaved
 1055 much more linearly but could be extended in future to include such non-linearities. Third,
 1056 in the real data the fluorescence peak amplitude seemed to vary from spike to spike, even
 1057 for well-isolated spike events. Recent research has shown that calcium influx due to a single

1058 action potential was quite variable in pyramidal cells, and that this variability had a effect on
1059 spike inference (Éltes et al., 2019). However in our model we assumed each spike lead to the
1060 same fixed-amplitude injection of calcium to the cell, leading to much greater regularity in
1061 fluorescence peak amplitudes. This variability could be added in future versions of the model
1062 by making the injected calcium peak a random variable. Fourth, we modelled the soma as
1063 a single compartment, but in reality there is likely a non-uniform spatial profile of calcium
1064 concentration. This may matter because some endogenous buffers might access calcium right
1065 as it influxes from the extracellular space, whereas the majority of the fluorescence signal is
1066 more likely coming from the bulk of the cytoplasm. Future models could attempt to model
1067 these spatial dependencies to assess whether they affect the overall spike inference procedure.

1068 As well as the optimised parameters, the model has 14 fixed parameters than can be
1069 changed to simulate different types of calcium indicators. This model could be used to test
1070 the theoretical performance of proposed new types of calcium indicator. The model could
1071 also be used by developers of spike inference algorithms to test the effects of changing cal-
1072 cium indicator parameters on spike inference, or to test the affects of changing spiking char-
1073 acteristics on spike inference. For example, high firing rate vs low firing rate, or bursting vs
1074 no bursting. Given the increasing amplitude of the fluorescence trace with increasing mean
1075 firing rate, it would be possible to build a spike inference algorithm on this principle at least
1076 in part.

1077 Our model has already been used as a tool by our colleagues, for simulating fluorescence
1078 traces in response to cells that can fire with a continuous rate between 10 and 20Hz, but do
1079 not always do so. Our colleagues found that a combination of the amplitude and the variance
1080 of the simulated fluorescence trace was the best indicator of firing rate. For example, when
1081 a cell was not firing, the amplitude and variance of the fluorescence trace was relatively low.
1082 When the cell fired with a low firing rate $\sim 1\text{Hz}$, the mean amplitude was still low but
1083 the variance of the fluorescence trace was high, and for high firing rate $\sim 10 - 20\text{Hz}$, the
1084 fluorescence amplitude was high, and the variance was low. In this way, our model may be
1085 useful for investigating firing rates underlying real fluorescence traces in response to cells
1086 which can fire in these rage ranges.

1087 A recent paper by Greenberg et al (2018) described a biophysical model for spike train
1088 inference called the ‘Sequential binding model’. Their model for spike inference was sim-
1089 ilar to our model for fluorescence traces in that their model included parameters for two
1090 types of endogenous buffer. But this model also included dynamics for calcium binding to
1091 and unbinding from these endogenous buffers. Furthermore, this model included dynamics

1092 for calcium binding to and unbinding from the four binding sites present on a GCaMPs6
1093 molecule. In the accuracy measurements specified in that paper, this model performed better
1094 than the MLspike algorithm, which is also partially a biophysically model, and it performed
1095 better than the constrained non-negative deconvolution algorithm. The sequential binding
1096 model also has biophysically interpretable parameters, and its fitted parameters for quantities
1097 such as buffering capacity and calcium influx upon action potential firing fall in line with
1098 experimental values (Greenberg et al., 2018). Biophysical models like this appear to be the
1099 way forward for spike inference algorithms, and would make a good complimentary tool to
1100 our fluorescence model.

1101 **Chapter 3**

1102 **Functional networks expand across
1103 anatomical boundaries as correlation
1104 time-scale increases**

1105 *Abstract*

1106 Decades of research has established that correlated spiking plays a crucial role in represent-
1107 ing sensory information. One drawback associated with the recent improvement in recording
1108 technology and consequent large datasets is the difficulty in analysing higher order correla-
1109 tions in large neuronal ensembles. One benefit of these datasets that has not yet been explored
1110 is the opportunity to compare correlations within anatomical regions to correlations across
1111 anatomical regions. In this work, we measured correlations between neurons residing in
1112 nine different brains regions in three awake and behaving mice. Using the these correlation
1113 measurements, we created weighted undirected graph networks and applied network science
1114 methods to detect functional communities in our neural ensembles. We compared these func-
1115 tional communities to their anatomical distribution. We repeated the analysis, using different
1116 timescales for our correlation measurements, and found that functional communities were
1117 more likely to be dominated by neurons from a single brain region at shorter timescales
1118 (< 100ms).

1119 3.1 Introduction

1120 Decades of research has established that correlations play a crucial role in representing sen-
1121 sory information. For example, the onset of visual attention has been shown to have a greater
1122 affect on the correlations in the macaque V4 region than on the firing rates in that region
1123 (Cohen and Maunsell, 2009). Recent findings show that spontaneous behaviours explain cor-
1124 relations in parts of the brain not associated with motor control (Stringer et al., 2019), that
1125 satiety state appears to have a brain wide representation (Allen et al., 2019), and that subject
1126 exploratory and non-exploratory states are represented in the amygdala (Gründemann et al.,
1127 2019). So, behavioural states are likely represented across many regions of the brain, not just
1128 motor related areas. In order to understand the brain, we must understand the interactions
1129 between neurons and regions.

1130 Because of limitations in recording technology almost all research has explored corre-
1131 lations between neurons within a given brain region, or within only two regions at most
1132 (Wierzynski et al., 2009; Patterson et al., 2014; Girard, Hupé, and Bullier, 2001). Rela-
1133 tively little is known about correlations between neurons in many different brain regions.
1134 However, the recent development of ‘Neuropixels’ probes (Jun et al., 2017) has allowed
1135 extracellular voltage measurements to be collected from multiple brain regions simultane-
1136 ously routinely, and in much larger numbers than traditional methods. In this project we
1137 used a publicly-available Neuropixels dataset to analyse correlations between different brain
1138 regions (Stringer et al., 2019).

1139 A drawback associated with the improvement in recording technology is an increase in
1140 the difficulty in analysing these data. For example, analysing the i th order interactions of
1141 N neurons generally requires estimation of N^i parameters. A number that becomes astro-
1142 nomical for large N . New methods are required for analysing these new large datasets. We
1143 attempted to address this requirement in this piece of research by applying a cutting-edge
1144 network science community detection method to neural data.

1145 Another unexplored area of research is the changes in cell interactions at different timescales.
1146 Studies have shown different timescales for fluctuations in spiking activity (Murray et al.,
1147 2014), and different time scales for event representation (Baldassano et al., 2017) across dif-
1148 ferent brain regions. Still most studies focus on quantifying interactions at a given timescale.
1149 But neurons may interact differently, or may interact with different neurons at different
1150 timescales. Here we explore correlated communities of neurons at different timescales.

1151 In this work, we measured correlations between binned spike counts from neurons from

1152 nine different regions of the mouse brain. These measurements induced a weighted undi-
1153 rected graph or network where each neuron is represented by a node, and the strength of
1154 the connection between these nodes/neurons is the strength of the correlation between their
1155 spike counts. We then applied newly invented network methods (Humphries et al., 2019)
1156 to this network to find any community structure, and place the neurons in these correlation
1157 based communities. Finally, we compared these functional communities to the anatomical
1158 membership of the neurons.

1159 To investigate the functional communities and their relationship with anatomy at different
1160 time scales, we repeated these analyses using different length bin widths when binning spike
1161 times.

1162 To find and analyse functional networks while controlling for the subject’s behaviour, we
1163 conditioned the binned spike counts on data from a video of the subject’s face, and repeated
1164 our analysis for spike count correlations (or noise correlations) and signal correlations.

1165 3.2 Data

1166 The data that we used in this project were collected by Nick Steinmetz and his lab members
1167 (Stringer et al., 2019).

1168 3.2.1 Brain regions

1169 Neuropixels probes were used to collect extracellular recordings (Jun et al., 2017) from three
1170 different mice. The mice were awake, headfixed, and engaging in spontaneous behaviour.
1171 The mice were of different sexes and different ages. One mouse was ‘wild-type’, the others
1172 were mutants. Details as follows:

- 1173 1. male, wild type, P73.
- 1174 2. female, TetO-GCaMP6s, Camk2a-tTa, P113
- 1175 3. male, Ai32, Pvalb-Cre, P99

1176 Eight probes were used to collect readings from 2296, 2668, and 1462 cells respectively.
1177 Data were collected from nine brain regions in each mouse:

- 1178 • Caudate Putamen (CP)
- 1179 • Frontal Motor Cortex (Frmocxt)
- 1180 • Hippocampal formation (Hpf)

- 1181 ● Lateral Septum (Ls)
- 1182 ● Midbrain (Mb)
- 1183 ● Superior Colliculus (Sc)
- 1184 ● Somatomotor cortex (Sommotcx)
- 1185 ● Thalamus (Th)
- 1186 ● Primary visual cortex (V1)

1187 Readings were continuous and lasted for about 1 hour (Stringer et al., 2019). Locations of
 1188 each of the probes can be seen in figure 3.1.

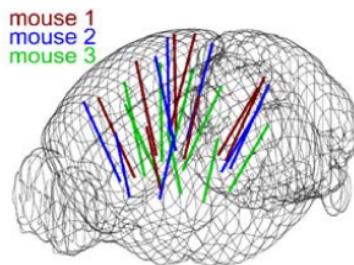


FIGURE 3.1: Probe Locations: The locations of the probes in each of the three mouse brains (Stringer et al., 2019).

1189 **3.2.2 Video recordings**

1190 Video recordings of the mouse's face were taken during the spontaneous behaviour. We had
 1191 access to the top 500 principle components and top 500 eigenvectors of the processed videos.
 1192 The frequency of recording was slightly less than 40Hz. Each frame contained 327×561
 1193 pixels. These principal components were used as behavioural data. We controlled for these
 1194 components when taking measurements conditioned on behaviour.

1195 **3.3 Methods**

1196 **3.3.1 Binning data**

1197 We transformed the spike timing data into binned spike count data by dividing the exper-
 1198 imental period into time bins and counting the spikes fired by each cell within the time period
 1199 covered by each of those bins. The data were divided into time bins of various widths ranging
 1200 from 0.01s to 4s.

If the total length of the recording period was not an integer multiple of the time bin width, we cut off the remaining time at the end of the recording period. This period was at most 3.99s. This is far less than the total recording time of around 1 hour. So, this detail would not affect our results.

3.3.2 Correlation coefficients

We calculated Pearson's correlation coefficient for pairs of spike counts from pairs of neurons. For jointly distributed random variables X and Y , Pearson's correlation coefficient is defined as:

$$\rho_{XY} = \frac{\text{cov}(X, Y)}{\sigma_X \sigma_Y} \quad (3.1)$$

$$= \frac{E[(X - \mu_X)(Y - \mu_Y)]}{\sigma_X \sigma_Y} \quad (3.2)$$

where E denotes the expected value, μ denotes the mean, and σ denotes the standard deviation. The correlation coefficient is a normalised measure of the covariance. It can take values between 1 (completely correlated) and -1 (completely anti-correlated). Two independent variables will have a correlation coefficient of 0. But, having 0 correlation does not imply independence.

If we do not know the means and standard deviations required for equation 3.1, but we have samples from X and Y , Pearson's sample correlation coefficient is defined as:

$$r_{XY} = \frac{\sum_{i=1}^n (x_i - \bar{x})(y_i - \bar{y})}{\sqrt{\sum_{i=1}^n (x_i - \bar{x})^2} \sqrt{\sum_{i=1}^n (y_i - \bar{y})^2}} \quad (3.3)$$

where $\{(x_i, y_i)\}$ for $i \in \{1, \dots, n\}$ are the paired samples from X and Y , and $\bar{x} = \frac{1}{n} \sum_{i=1}^n x_i$, and $\bar{y} = \frac{1}{n} \sum_{i=1}^n y_i$ are the sample means.

In practice we used the python function `scipy.stats.pearsonr` to calculate the correlation coefficients.

1215 Total correlations, r_{SC}

The total correlation (r_{SC}) of two cells is the correlation between the spike counts of those cells in response to a given stimulus condition.

1218 **Shuffled total correlations**

1219 We measured the shuffled total correlations between two neurons by randomly permuting one
 1220 of the neuron's spike counts and measuring the total correlations. These shuffled correlations
 1221 were useful when measuring the effect of time bin width on correlations, and when decid-
 1222 ing which correlations should be preserved when creating correlation networks (see section
 1223 [3.3.5](#)).

1224 **Separating Correlations & Anti-correlations**

1225 In order to compare the effect of bin width on measures of negative r_{SC} (anti-correlation) and
 1226 positive r_{SC} separately, we had to separate correlated and anti-correlated pairs. To do this, we
 1227 simply measured the mean r_{SC} , taking the mean across all the bin widths. If this quantity was
 1228 positive or zero we regarded the pair as positively correlated. If this quantity was negative
 1229 we regarded the pair as anti-correlated.

1230 **3.3.3 Conditioning on behavioural data**

Our behavioural data consisted of the top 500 principal components (PCs) of a processed video recording of the mouse's face (see section [3.2.2](#)). Denoting the spike count of a given cell by X , and the PCs by Z_1, \dots, Z_{500} , we wanted to model X as a function of Z_1, \dots, Z_{500} in order to estimate

$$E[X|Z_1, \dots, Z_{500}] = \int_{x \in X} x P(X = x|Z_1, \dots, Z_{500}) dx \quad (3.4)$$

$$= \int_{x \in X} x \frac{P(X = x, Z_1, \dots, Z_{500})}{P(Z_1, \dots, Z_{500})} dx \quad (3.5)$$

1231 Given the 500 components, a naïve estimation of $P(Z_1, \dots, Z_{500})$ or $P(X, Z_1, \dots, Z_{500})$ by
 1232 histogramming was impossible. Therefore we modelled X as a linear combination of the
 1233 PCs.

1234 **Linear regression**

1235 We modelled the spike count of a given cell, X , as a linear combination of the PCs of the
 1236 video of the mouse's face, $\mathbf{Z} = Z_1, \dots, Z_{500}$. We tried three different types of regularization

1237 • L1 or 'Lasso'

1238 • L2 or 'Ridge regression'

- 1239 • ‘Elastic net’ regularisation (a linear combination of both $L1$ and $L2$ regularisation
 1240 penalties)

1241 The elastic net regularisation performed the best, so we stuck with that.

1242 **Elastic net regularisation**

Suppose we wish to model n observations of a random variable X , $\mathbf{x} = (x_1, \dots, x_n)$ using n instances of m predictors $\mathbf{Z} = (Z_1, \dots, Z_m)$. The naïve elastic net criterion is

$$L(\lambda_1, \lambda_2, \boldsymbol{\beta}) = |\mathbf{x} - \mathbf{Z}\boldsymbol{\beta}|^2 + \lambda_2|\boldsymbol{\beta}|_2 + \lambda_1|\boldsymbol{\beta}|_1 \quad (3.6)$$

where

$$|\boldsymbol{\beta}|_2 = \sum_{j=1}^m \beta_j^2 \quad (3.7)$$

$$|\boldsymbol{\beta}|_1 = \sum_{j=1}^m |\beta_j| \quad (3.8)$$

The naïve elastic net estimator $\hat{\boldsymbol{\beta}}$ is the minimiser of the system of equations 3.6 (Zou and Hastie, 2005)

$$\hat{\boldsymbol{\beta}} = \arg \min_{\boldsymbol{\beta}} L(\lambda_1, \lambda_2, \boldsymbol{\beta}) \quad (3.9)$$

1243 We implemented the model using the `ElasticNetCV` method of Python’s
 1244 `sklearn.linear_models` package.

1245 As well as using the PCs, we also tried fitting the models using the raw video data recon-
 1246 structed from the PCs and eigenvectors. These models performed worse than those using the
 1247 PCs. We expected this because each representation contains the same amount of information,
 1248 but the raw video representation spreads this information across many more components.
 1249 This requires more parameter fitting, but given the same information.

1250 **Conditional covariance**

We calculated the expected value of the conditional covariance using the law of total covariance.

$$\text{cov}(X, Y) = E[\text{cov}(X, Y|Z)] + \text{cov}(E[X|Z], E[Y|Z]) \quad (3.10)$$

1251 where these expected values are calculated with respect to the distribution of Z as a random
 1252 variable.

1253 The law of total covariance breaks the covariance into two components. The first com-
 1254 ponent $E[\text{cov}(X, Y|Z)]$ is the expected value, under the distribution of Z , of the conditional
 1255 covariance $\text{cov}(X, Y|Z)$. This covariance could be interpreted as the unnormalised version
 1256 of what Cohen et al. (2011) call the spike count correlation (Cohen and Kohn, 2011), aka.
 1257 the noise correlation. In particular, this is the covariance of the spike counts in response to
 1258 repeated presentation of identical stimuli.

1259 The second component is analogous to what Cohn et al. (2011) call the *signal correlation*
 1260 (Cohen and Kohn, 2011). In particular, $\text{cov}(E[X|Z], E[Y|Z])$ is the covariance between
 1261 spike counts in response to different stimuli.

Using our linear model, we calculated $E[X|Z_1, \dots, Z_{500}]$ for each cell X . Then we pro-
 ceeded to calculate

$$E[\text{cov}(X, Y|Z_1, \dots, Z_{500})] = \text{cov}(X, Y) - \quad (3.11)$$

$$\text{cov}(E[X|Z_1, \dots, Z_{500}], E[Y|Z_1, \dots, Z_{500}]) \quad (3.12)$$

1262 **Measures of conditional correlation**

As a measure of expected correlation, we measured the ‘event conditional correlation’ (Maugis,
 2014)

$$\rho_{XY|Z} = \frac{E[\text{cov}(X, Y|Z)]}{\sqrt{E[\text{var}(X|Z)]E[\text{var}(Y|Z)]}} \quad (3.13)$$

1263 Although this is not an actual correlation, it is an intuitive analogue to the correlation as a
 1264 normalised version of the covariance.

For comparison, we also measured the ‘signal correlation’

$$\rho_{\text{signal}} = \frac{\text{cov}(E[X|Z], E[Y|Z])}{\sqrt{\text{var}(E[X|Z])\text{var}(E[Y|Z])}} \quad (3.14)$$

1265 this is an actual correlation.

1266 **3.3.4 Information Theory**

1267 **Entropy $H(X)$**

The entropy of a random variable X , with outcomes x_1, \dots, x_N , and corresponding probabilities p_1, \dots, p_N is defined as

$$H(X) = - \sum_{n=1}^N p_n \log_2 p_n \quad (3.15)$$

1268 This quantity is also known as the information entropy or the ‘surprise’. It measures the
 1269 amount of uncertainty in a random variable. For example, a variable with a probability of 1
 1270 for one outcome, and 0 for all other outcomes will have 0 bits entropy, because it contains no
 1271 uncertainty. But a variable with a uniform distribution will have maximal entropy as it is the
 1272 least predictable. This quantity is analogous to the entropy of a physical system (Shannon,
 1273 1948). Note that any base may be used for the logarithm in equation 3.15, but using base 2
 1274 means that the quantity will be measured in ‘bits’.

The joint entropy of two jointly distributed random variables X and Y , where Y has outcomes y_1, \dots, y_M , is defined as

$$H(X, Y) = - \sum_{n=1}^N \sum_{m=1}^M P(X = x_n, Y = y_m) \log_2 P(X = x_n, Y = y_m) \quad (3.16)$$

1275 If X and Y are independent then $H(X, Y) = H(X) + H(Y)$. Otherwise $H(X, Y) <$
 1276 $H(X) + H(Y)$. When X and Y are completely dependent $H(X, Y) = H(X) = H(Y)$.

The conditional entropy of Y conditioned on X is defined as

$$H(Y|X) = - \sum_{n=1}^N \sum_{m=1}^M P(X = x_n, Y = y_m) \log_2 \frac{P(X = x_n, Y = y_m)}{P(X = x_n)} \quad (3.17)$$

1277 When X and Y are independent $H(Y|X) = H(Y)$. Intuitively, we learn nothing of Y by
 1278 knowing X , so Y is equally uncertain whether we know X or not. If Y is totally dependent
 1279 on X , then the fraction in the logarithm is 1, which gives $H(Y|X) = 0$.

1280 These entropy measures are the basis of the mutual information measure.

1281 **Maximum entropy limit**

When spiking data is binned into spike counts there is an upper limit on the entropy of these data. The maximum entropy discrete distribution is the discrete uniform distribution. A

random variable with this distribution will take values from some finite set with equal probabilities. Binned spike count data will take values between 0 and some maximum observed spike count n_{\max} . A neuron with responses that maximises entropy will take these values with equal probability, i.e. if $i \in \{0, \dots, n_{\max}\}$ then $P(X = i) = \frac{1}{n_{\max} + 1}$. The entropy of this neuron will be

$$\begin{aligned} H(X) &= - \sum_{i=0}^{n_{\max}} P(X = i) \log_2 P(X = i) \\ &= - \sum_{i=0}^{n_{\max}} \frac{1}{n_{\max} + 1} \log_2 \left(\frac{1}{n_{\max} + 1} \right) \\ &= - \log_2 \left(\frac{1}{n_{\max} + 1} \right) \\ &= \log_2 (n_{\max} + 1) \end{aligned}$$

1282 Therefore, the maximum entropy of the binned spike counts of a neuron is $\log_2 (n_{\max} + 1)$.
 1283 Of course, it would be very unusual for a neuron to fire in accordance with the discrete
 1284 uniform distribution. Most measurements of entropy taken on binned spiking data will be
 1285 much lower than the maximum. See figure 3.2 to see the maximum entropy as a function of
 1286 the maximum observed spike count.

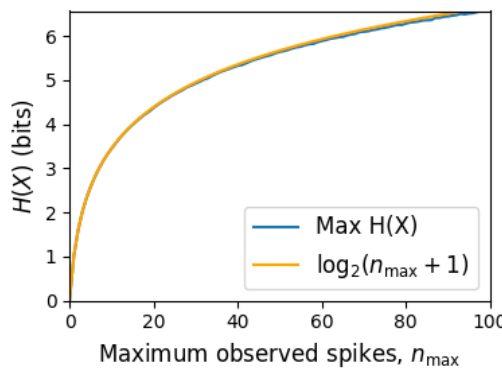


FIGURE 3.2: **Entropy Limit:** The upper limit on entropy of binned spike count data as a function of the maximum observed spike count. The orange line is the analytical maximum. The blue line is the entropy of samples with $N = 1000$ data points taken from the discrete uniform distribution.

1287 **Mutual Information $I(X; Y)$**

1288 The mutual information can be defined mathematically in a number of ways, all of which are
 1289 equivalent. These definitions illustrate the different ways of interpreting the mutual informa-
 1290 tion.

For two jointly distributed random variables X and Y , the mutual information $I(X;Y)$ is defined as

$$I(X;Y) = H(Y) - H(Y|X) \quad (3.18)$$

$$= H(X) - H(X|Y) \quad (3.19)$$

1291 Equation 3.18 fits with the following intuition: The mutual information between X and Y is
 1292 the reduction in uncertainty about X gained by knowing Y , or vice versa. We could also say
 1293 the mutual information is the amount of information gained about X by knowing Y , or vice
 1294 versa.

Another useful entropy based definition for the mutual information is

$$I(X;Y) = H(X) + H(Y) - H(X,Y) \quad (3.20)$$

1295 This definition is useful because it does not require the calculation of conditional probabili-
 1296 ties.

The mutual information can also be defined in terms of marginal, joint, and conditional distributions. For example,

$$I(X;Y) = - \sum_{n=1}^N \sum_{m=1}^M P(X = x_n, Y = y_m) \log_2 \frac{P(X = x_n, Y = y_m)}{P(X = x_n)P(Y = y_m)} \quad (3.21)$$

Notice that this can be rewritten as a Kullback–Leibler divergence.

$$I(X;Y) = D_{KL}(P(X,Y) || P(X)P(Y)) \quad (3.22)$$

1297 So, we can also think of the mutual information as a measure of the difference between
 1298 the joint distribution of X and Y , and the product of their marginal distributions. Since the
 1299 product of the marginal distributions is the joint distribution for independent variables, we
 1300 can think of the mutual information as a measure of the variables’ dependence on one another.

1301 The minimum value that $I(X;Y)$ can take is 0. This occurs when the random variables
 1302 X and Y are independent. Then we have $H(X|Y) = H(X)$, and $H(Y|X) = H(Y)$, which
 1303 according to equation 3.18, gives $I(X;Y) = 0$. We also have that $H(X,Y) = H(X) +$
 1304 $H(Y)$ in this case, which according equation 3.20, gives $I(X;Y) = 0$. Finally, we also have
 1305 $P(X,Y) = P(X)P(Y)$, which leaves us with 1 in the argument for the logarithm in equation
 1306 3.21, which again gives $I(X;Y) = 0$.

1307 The mutual information reaches its maximum value when one of the variables X and
 1308 Y is completely determined by knowing the value of the other. In that case $I(X; Y) =$
 1309 $\min\{H(X), H(Y)\}$.

1310 **Variation of Information** $VI(X, Y)$

The variation of information is another information theoretical quantity based on the mutual information. It is defined as

$$VI(X; Y) = H(X) + H(Y) - 2I(X; Y) \quad (3.23)$$

We can rewrite this as the summation of two positive quantities

$$VI(X; Y) = [H(X) - I(X; Y)] + [H(Y) - I(X; Y)] \quad (3.24)$$

1311 In English, the variation of information is the summation of the uncertainty in the random
 1312 variables X and Y excluding the uncertainty shared by those variables.

1313 This measure will become more relevant when we go on to talk about clusterings because
 1314 $VI(X; Y)$ forms a metric on the space of clusterings.

1315 **Measuring entropies & mutual information**

1316 In practice, we measured the mutual information between spike counts using Python and the
 1317 python package `pyitlib`. We used the PT-bias correction technique to estimate the bias of
 1318 our measurements when measuring the mutual information between the spike counts of two
 1319 cells (Treves and Panzeri, 1995).

1320 When measuring the mutual information between clusterings we used Python, but we
 1321 used the `mutual_info_score`, `adjusted_mutual_info_score`, and
 1322 `normalized_mutual_info_score` functions from the `sklearn.metrics` part of
 1323 the `sklearn` package.

1324 **3.3.5 Network analysis**

1325 **Correlation networks**

1326 In order to analyse functional networks created by the neurons in our ensemble, we mea-
 1327 sured the total correlation between each pair of neurons. These measurements induced an

1328 undirected weighted graph/network between the neurons. The weight of each connection
1329 was equal to the total correlation between each pair of neurons.

1330 We followed the same procedure for total correlations 3.3.2, spike count correlations, and
1331 signal correlations 3.3.3.

1332 **Rectified correlations**

1333 At the time of writing, the community detection method outlined in (Humphries et al., 2019)
1334 could only be applied to networks with positively weighted connections. But many neuron
1335 pairs were negatively correlated. To apply the community detection method, we *rectified* the
1336 network, by setting all the negative weights to zero.

1337 We also looked for structure in the network created by negative correlations by reversing
1338 the signs of the correlations, and rectifying these correlations before applying our network
1339 analysis.

1340 Finally, we used the absolute value of the correlations as the weights for the graph/network.
1341 By doing this, we hoped to identify both correlated and anti-correlated functional communi-
1342 ties of neurons.

1343 **Sparsifying data networks**

1344 When creating our correlation networks, we wanted to exclude any correlations that could
1345 be judged to exist ‘by chance’. To do this, we measured the 5th and 95th percentile of
1346 the shuffled correlations (see section 3.3.2) for the given mouse and time bin width. We
1347 then set all the data correlations between these two values to 0. This excluded any ‘chance’
1348 correlations from our network, and created a sparser network. This allowed us to make use
1349 of the ‘sparse weighted configuration model’ as described in section 3.3.5.

1350 **Communities**

1351 Given some network represented by an adjacency matrix \mathbf{A} , a community within that net-
1352 work is defined as a collection of nodes where the number of connections within these nodes
1353 is higher than the expected number of connections between these nodes. In order to quan-
1354 tify the ‘expected’ number of connections, we need a model of expected networks. This is
1355 analogous to a ‘null model’ in traditional hypothesis testing. We test the hypothesis that our
1356 data network departs from the null network model to a statistically significant degree. For
1357 undirected unweighted networks, the canonical model of a null network is the configuration

model (Fosdick et al., 2016). Since we are working with weighted sparse networks, we used more suitable null models, described below.

1360 **Weighted configuration model**

1361 The *weighted configuration model* is a canonical null network model for weighted networks.
 1362 Given some data network, the weighted configuration model null network will preserve the
 1363 degree sequence and weight sequence of each node in the data network. But the edges will
 1364 be distributed randomly (Fosdick et al., 2016). Any structure in the data network beyond
 1365 its degree sequence and weight sequence will not be captured in the weighted configuration
 1366 model. So, this model can be used in testing the hypothesis that this extra structure exists.

1367 **Sparse weighted configuration model**

1368 The *sparse weighted configuration model* is another null network model. Similar in nature to
 1369 the weighted configuration model (see section 3.3.5), but the sparsity of the data network is
 1370 preserved in the null network. This is achieved by sampling from a probability distribution
 1371 for the creation or non-creation of each possible connection, then distributing the weight of
 1372 the data network randomly in this sparse network (Humphries et al., 2019). This is the null
 1373 network that we used when searching for additional structure in our data networks.

1374 **Spectral rejection**

1375 We made use of the spectral rejection algorithm as outlined in (Humphries et al., 2019). The
 1376 spectral rejection algorithm is a method for finding structure in a network not captured by a
 1377 supposed null model, if such structure exists.

To describe the method, we denote our data network matrix \mathbf{W} , we denote the expected network of our null network model as $\langle \mathbf{P} \rangle$. Then the departure of our data network from the null network can be described by the matrix

$$\mathbf{B} = \mathbf{W} - \langle \mathbf{P} \rangle \quad (3.25)$$

1378 a common choice for $\langle \mathbf{P} \rangle$ in community detection is the ‘configuration model’ (Fosdick et
 1379 al., 2016; Humphries, 2011). The matrix \mathbf{B} is often called the configuration matrix, in this
 1380 context we will use the term ‘deviation matrix’ as it captures the deviation of \mathbf{W} from the
 1381 null model.

1382 To test for structure in the network represented by \mathbf{W} , we examine the eigenspectrum of \mathbf{B}
1383 and compare it to the eigenspectrum of our null model. Firstly, note that since our data model
1384 doesn't allow self loops, and is not directed, the matrix representing the network will be
1385 symmetric and positive semi-definite, and will therefore be invertible with real eigenvalues.
1386 We selected a null model with the same characteristics.

1387 To find the eigenspectrum of the null model, we generated N samples from our null
1388 model P_1, \dots, P_N , and we measured their deviation matrices B_1, \dots, B_N . We then calculated
1389 the eigenspectrum of each of those samples. We calculated the upper bound of the null model
1390 eigenspectrum by taking the mean of the largest eigenvalues of B_1, \dots, B_N . We calculated a
1391 lower bound on the null model eigenspectrum by taking the mean of the smallest eigenvalues
1392 of B_1, \dots, B_N .

1393 We then calculated the eigenspectrum of \mathbf{B} , our data network deviation matrix. If any of
1394 those eigenvalues lay outside of the upper or lower bounds of the null model eigenspectrum,
1395 this is evidence of additional structure not captured by the null model. If we chose the sparse
1396 weighted configuration model (see section 3.3.5) as our null network model, then eigenvalues
1397 lying below the lower bound indicate k -partite structure in the network. For example, if one
1398 eigenvalue lay below the lower bound, this would indicate some bipartite structure in the data
1399 network. If any eigenvalues lay above the upper bound of the null model eigenspectrum, this
1400 is evidence of community structure in the data network. For example, one eigenvalue of \mathbf{B}
1401 lying above the upper bound of the null model eigenspectrum indicates the presence of two
1402 communities in the network (Humphries, 2011).

1403 **Node rejection**

1404 If there are d data eigenvalues lying outside of the null network eigenspectrum, the d eigen-
1405 vectors corresponding to these eigenvalues will form a vector space. If we project the nodes
1406 of our network into this vector space, by projecting either rows or columns of the data ma-
1407 trix, we can see how strongly each node contributes to the vector space. Nodes that contribute
1408 strongly to the additional structure will project far away from the origin, nodes that do not
1409 contribute to the additional structure will project close to the origin. We want to use this
1410 information to discard those nodes that do not contribute.

1411 We can test whether a node projects *far* away from the origin or *close* to the origin
1412 using the eigenvalues and eigenvectors of B_1, \dots, B_N . The j th eigenvector and eigenvalue
1413 of B_i gives a value for a null network's projection into the j th dimension of the additional
1414 structure vector space. The matrices B_1, \dots, B_N give N projections into that dimension.

1415 These projections are a distribution of the null networks' projections. If the data node's
 1416 projection exceeds that of the null network projections this node is judged to project *far* from
 1417 the origin, and therefore contribute to the additional structure. Otherwise, the node is judged
 1418 to project *close* to the origin, and is therefore rejected (Humphries et al., 2019).

1419 **Community detection**

1420 Another application for this d dimensional space is community detection. We first project
 1421 all of the nodes into this d -dimensional space, then perform the clustering in this space. The
 1422 clustering and community detection procedure is described in (Humphries, 2011).

1423 In practice, the procedure is carried out n times (we chose $n = 100$ times), this returns n
 1424 clusterings. We resolve these n clusterings to one final clustering using *consensus clustering*.
 1425 We used the consensus clustering method that uses an explicit null model for the consensus
 1426 matrix, as outlined in (Humphries et al., 2019).

1427 **3.3.6 Clustering Comparison**

A clustering \mathcal{C} is a partition of a set D into sets C_1, C_2, \dots, C_K , called clusters, that satisfy the following for all $k, l \in \{1, \dots, K\}$:

$$C_k \cap C_l = \emptyset \quad (3.26)$$

$$\bigcup_{k=1}^K C_k = D \quad (3.27)$$

1428 If we consider two clusterings, \mathcal{C} with clusters C_1, C_2, \dots, C_K and \mathcal{C}' with clusters
 1429 C'_1, C'_2, \dots, C'_K . There are a number of measurements we can use to compare \mathcal{C} and \mathcal{C}' . In
 1430 the following, the number of elements in D is denoted by n , and the number of elements in
 1431 cluster C_k is n_k .

1432 **Adjusted Rand Index**

1433 The *adjusted Rand Index* is a normalised similarity measure for clusterings based on pair
 1434 counting.

1435 If we consider the clusterings \mathcal{C} and \mathcal{C}' , and denote

1436 • the number of pairs in the same cluster in \mathcal{C} and \mathcal{C}' by N_{11}

1437 • the number of pairs in different clusters in \mathcal{C} and \mathcal{C}' by N_{00}

- 1438 • the number of pairs in the same cluster in \mathcal{C} and different clusters in \mathcal{C}' by N_{10}

- 1439 • the number of pairs in different clusters in \mathcal{C} and the same cluster in \mathcal{C}' by N_{01}

then the *Rand Index* is defined as

$$RI = \frac{N_{11} + N_{00}}{N_{11} + N_{00} + N_{10} + N_{01}} = \frac{N_{11} + N_{00}}{\binom{n}{2}} \quad (3.28)$$

1440 The Rand Index is 1 when the clusterings are identical, and 0 when the clusterings are com-
1441 pletely different.

The *adjusted Rand Index* intends on correcting the Rand Index for chance matching pairs.

This is defined as

$$ARI = \frac{2(N_{00}N_{11} - N_{01}N_{10})}{(N_{00} + N_{01})(N_{01} + N_{11}) + (N_{00} + N_{10})(N_{10} + N_{11})} \quad (3.29)$$

1442 The adjusted Rand Index is 1 when the clusterings are identical, and 0 when the Rand Index
1443 is equal to its expected value.

1444 Clusterings as random variables

If we take any random element of D , the probability that this element is in cluster C_k of clustering \mathcal{C} is

$$P(K = k) = \frac{n_k}{n} \quad (3.30)$$

1445 this defines a probability distribution, which makes the clustering a random variable. Any
1446 clustering can be considered as a random variable this way.

This means that we can measure any of the information theoretic quantities defined in section 3.3.4 with respect to clusterings. For example, the entropy of a clustering is

$$H(\mathcal{C}) = - \sum_{k=1}^K \frac{n_k}{n} \log \frac{n_k}{n} \quad (3.31)$$

If we have two clusterings, the joint probability distribution of these clusterings is defined as

$$P(K = k, K' = k') = \frac{|C_k \cap C'_{k'}|}{n} \quad (3.32)$$

1447 The joint distribution allows us to define the mutual information between two clusterings,
1448 $I(\mathcal{C}; \mathcal{C}')$ (Meilă, 2007).

1449 **Information based similarity measures**

The mutual information between two clusterings is a similarity measure, with $I(\mathcal{C}; \mathcal{C}') = 0$ if \mathcal{C} and \mathcal{C}' are completely different, and $I(\mathcal{C}; \mathcal{C}') = H(\mathcal{C}) = H(\mathcal{C}')$ if \mathcal{C} and \mathcal{C}' are identical. This can be normalised in a number of different ways to make more similarity measures (Vinh, Epps, and Bailey, 2010)

$$NMI_{joint} = \frac{I(\mathcal{C}; \mathcal{C}')}{H(\mathcal{C}, \mathcal{C}')} \quad (3.33)$$

$$NMI_{max} = \frac{I(\mathcal{C}; \mathcal{C}')}{\max\{H(\mathcal{C}), H(\mathcal{C}')\}} \quad (3.34)$$

$$NMI_{sum} = \frac{2I(\mathcal{C}; \mathcal{C}')}{H(\mathcal{C}) + H(\mathcal{C}')} \quad (3.35)$$

$$NMI_{sqrt} = \frac{I(\mathcal{C}; \mathcal{C}')}{\sqrt{H(\mathcal{C})H(\mathcal{C}')}} \quad (3.36)$$

$$NMI_{min} = \frac{I(\mathcal{C}; \mathcal{C}')}{\min\{H(\mathcal{C}), H(\mathcal{C}')\}} \quad (3.37)$$

We can control for chance similarities between the two clusterings by measuring the *adjusted mutual information* between the clusterings. This is defined as

$$AMI_{sum} = \frac{I(\mathcal{C}; \mathcal{C}') - E\{I(\mathcal{C}; \mathcal{C}')\}}{\frac{1}{2}[H(\mathcal{C}) + H(\mathcal{C}')] - E\{I(\mathcal{C}; \mathcal{C}')\}} \quad (3.38)$$

1450 The first term in the denominator, taking the average of the marginal entropies, can be re-
 1451 placed by taking the maximum, minimum, or the geometric mean (Vinh, Epps, and Bailey,
 1452 2010).

1453 **Information based metrics**

The variation of information between two clusterings $VI(\mathcal{C}; \mathcal{C}')$ (see section 3.3.4) is a metric on the space of clusterings (Meilă, 2007). That is,

$$VI(\mathcal{C}; \mathcal{C}') \geq 0 \quad (3.39)$$

$$VI(\mathcal{C}; \mathcal{C}') = 0 \iff \mathcal{C} = \mathcal{C}' \quad (3.40)$$

$$VI(\mathcal{C}; \mathcal{C}') = VI(\mathcal{C}'; \mathcal{C}) \quad (3.41)$$

$$VI(\mathcal{C}; \mathcal{C}'') \leq VI(\mathcal{C}; \mathcal{C}') + VI(\mathcal{C}'; \mathcal{C}'') \quad (3.42)$$

Another metric is the *information distance* (Vinh, Epps, and Bailey, 2010)

$$D_{max} = \max\{H(\mathcal{C}), H(\mathcal{C}')\} - I(\mathcal{C}; \mathcal{C}') \quad (3.43)$$

Both of these can be normalised

$$NVI(\mathcal{C}; \mathcal{C}') = 1 - \frac{I(\mathcal{C}; \mathcal{C}')}{H(\mathcal{C}, \mathcal{C}')} \quad (3.44)$$

$$d_{max} = 1 - \frac{I(\mathcal{C}; \mathcal{C}')}{\max\{H(\mathcal{C}), H(\mathcal{C}')\}} \quad (3.45)$$

1454 Comparing detected communities and anatomical divisions

1455 In order to quantify the difference or similarity between the communities detected in our cor-
 1456 relation network and the anatomical classification of the cells in that network, we considered
 1457 the communities and the anatomical regions as clusters in two different clusterings, \mathcal{C}_{comm}
 1458 and \mathcal{C}_{anat} , respectively. We then measured the similarity between the clusterings using the
 1459 mutual information, the adjusted mutual information, and the normalised mutual informa-
 1460 tion. We measured the difference between, or the distance between, the clusterings using the
 1461 variation of information, the normalised variation of information, and the normalised infor-
 1462 mation distance. We also measured the difference between the clusterings using the adjusted
 1463 Rand Index, just to use a non-information based measure.

1464 We took all of these measures for communities detected using different time bin widths.
 1465 This gave us an idea of the effect of time bin width on correlation networks in neural ensem-
 1466 bles relative to anatomical regions within those ensembles.

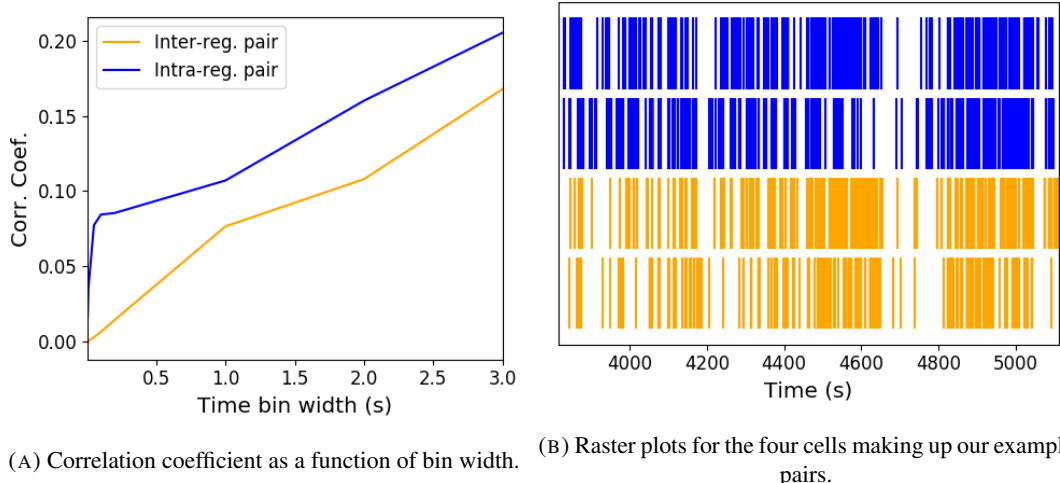
1467 3.4 Results

1468 Note that in the following text, we refer to the correlation coefficient between two sequences
 1469 of spike counts from two different cells as the *total correlation*. We refer to the correlation
 1470 between spike counts in response to a certain stimulus as the *spike count correlation* aka
 1471 *noise correlation*, and we refer to the correlation between mean or expected responses to
 1472 different stimuli as the *signal correlation* (Cohen and Kohn, 2011).

1473 The nine different brain regions from which we had data were the caudate putamen (CP),
 1474 frontal motor cortex (FrMoCtx), hippocampus (HPF), lateral septum (LS), midbrain (MB),
 1475 primary visual cortex (V1), superior colliculus (SC), somatomotor cortex (SomMoCtx), and
 1476 thalamus (TH).

1477 **3.4.1 Average correlation size increases with increasing time bin width**

1478 First we inspected the affect of time bin width on total correlations. We know that using short
 1479 time bins results in artificially small correlation measurements (Cohen and Kohn, 2011), so
 1480 we expected to see an increase in correlation amplitude with increasing time bin width. That
 1481 is exactly what we observed. Taking 50 cells at random, we calculated the total correla-
 1482 tion between every possible pair of these cells, using different time bin widths ranging from
 1483 0.005s to 3s. We found that the longer the time bin width, the greater the correlations (see
 1484 figure 3.4a).



(A) Correlation coefficient as a function of bin width. (B) Raster plots for the four cells making up our example pairs.

FIGURE 3.3: (A) An example of the correlation coefficients between two different pairs of cells, one where both cells are in the same brain region (intra-regional pair), and one where both cells are in different brain regions (inter-regional pair). The correlation coefficients have been measured using different time bin widths, ranging from 5ms to 3s. Note the increasing amplitude of the correlations with increasing bin width. (B) A raster plot showing the spike times of each pair of cells.

1485 We also separated the positively correlated pairs from the negatively correlated pairs
 1486 using the mean correlation of each pair across all bin widths (see section 3.3.2). We found
 1487 that the positively correlated pairs become more positively correlated with increasing time bin
 1488 width, and the negatively correlated pairs become more negatively correlated with increasing
 1489 time bin width (see figures 3.4b and 3.4c).

1490 In figure 3.3a we plot correlations from two example pairs, one pair from within a region,
 1491 and one pair between regions. It can be seen that the correlation coefficient increases with
 1492 bin width. The correlations can be observed by eye in the raster plot for these cells in figure
 1493 3.3b.

1494 When taking the mean across all pairs, the positively correlated pairs dominate in terms
 1495 of both number of pairs, and amplitude of correlations. Therefore the mean across all pairs

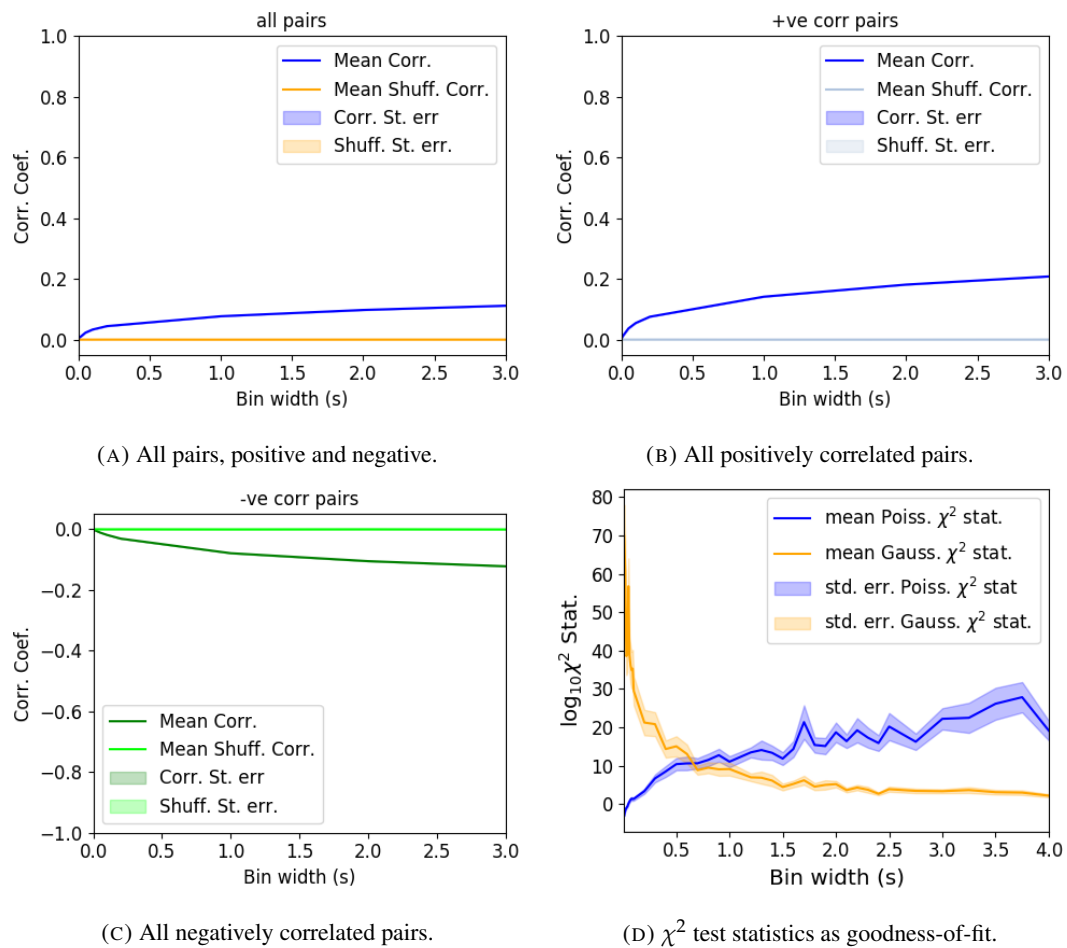


FIGURE 3.4: Mean correlation coefficients measured from pairs of 50 randomly chosen neurons. (A) All possible pairs, (B) positively correlated pairs, and (C) negatively correlated pairs. (D) Mean and standard error of χ^2 test statistics for Poisson and Gaussian distributions fitted to neuron spike counts.

1496 is positive.

1497 These results were observed in each of the three mouse subjects from which we had data.

1498 3.4.2 Goodness-of-fit for Poisson and Gaussian distributions across increasing 1499 time bin widths

1500 We wanted to investigate if the width of the time bin used to bin spike times into spike counts
1501 had an effect on the distribution of spike counts. We used the χ^2 statistic as a goodness-of-fit
1502 measure for Poisson and Gaussian (normal) distributions to the spike count of 100 randomly
1503 chosen neurons for a number of bin widths ranging from 0.01s to 4s. For the χ^2 statistic, the
1504 higher the value, the worse the fit.

1505 We expected a Poisson distribution to be a better fit for shorter time bin widths because
1506 spike counts must be non-negative, therefore any distribution of spike counts with mass dis-
1507 tributed at or close to 0 will be skewed. The distribution of spike counts is more likely to be
1508 distributed close to 0 when the time bin widths used to bin spike times into spike counts are
1509 small relative to the amount of time it takes for a neuron to fire an action potential ($\sim 1\text{ms}$ in
1510 the case of non-burst firing neurons).

1511 We expected a Gaussian distribution to be a better fit for longer time bin widths, because
1512 a Poisson distribution with a large rate is well approximated by a Gaussian distribution with
1513 mean and variance equal to the Poisson rate. Therefore, a Gaussian distribution would ap-
1514 proximate the mean of a collection of large spike counts, and have more flexibility than a
1515 Poisson distribution to fit the variance.

1516 We found that that a Poisson distribution is the best fit for shorter time bins less than 0.7s
1517 in length. Then a Gaussian distribution is a better fit for time bins greater than 0.7s in length
1518 (see figure 3.4d).

1519 3.4.3 Differences between and inter- and intra- regional correlations decrease 1520 with increasing bin width

1521 We investigated the differences in distribution between inter-regional correlations, i.e. corre-
1522 lations between neurons in different brain regions, and intra-regional correlations, i.e. corre-
1523 lations between neurons in the same brain region.

1524 Firstly, we investigated these quantities for all possible pairs of ~ 500 neurons taken
1525 from across all the 9 brain regions from which we had data. We distributed these neurons as
1526 evenly as possible across all of the regions, so that cells from one region would not dominate
1527 our data. We observed that the mean intra-regional correlations were always higher than the

mean inter-regional correlations for every value of time bin width used. We also observed that as the time bin width increased these mean correlations increased and the difference between the mean inter-regional and intra-regional correlations grew (see figure 3.5 (Left)).

Stringer et al. (2019) had a similar finding using the same data. They used only one value for the time bin width, 1.2s. Using this time bin width to bin spike times and measure total correlations, they found that the mean ‘within-region’ correlations were always greater than the ‘out-of-region’ correlations (Stringer et al., 2019). The figure from their paper showing this result can be seen in figure 3.5 (Right).

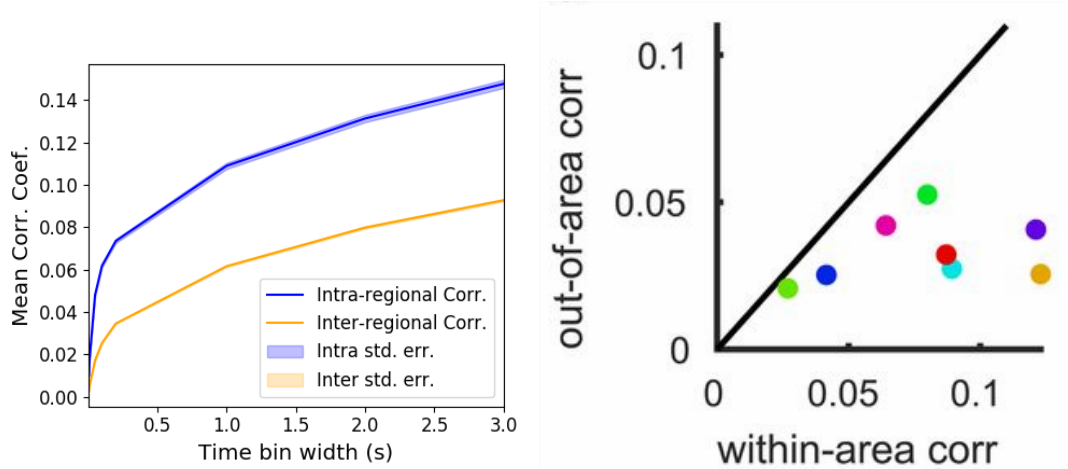
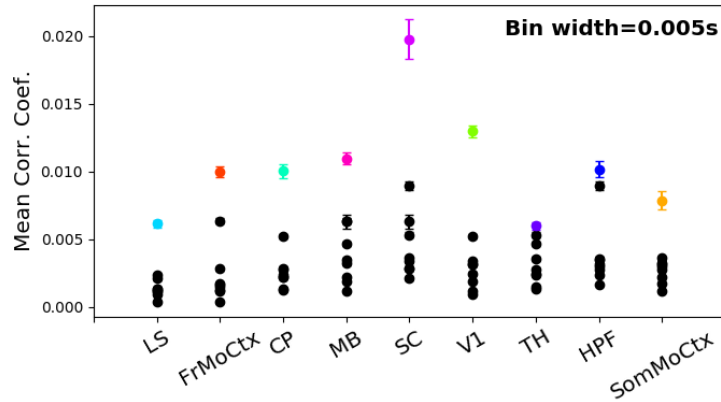


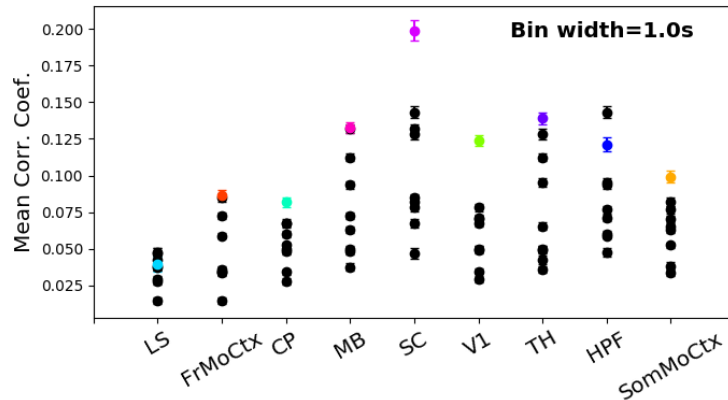
FIGURE 3.5: (Left)The mean intra-region and inter-region correlations using all possible pairs of ~ 500 neurons, spread across 9 different brain regions. (Right) Courtesy of Stringer et al. (2019), mean inter-regional (out-of-area) correlation coefficients vs mean intra-regional (within-area) correlation coefficients for a bin width of 1.2s. Note that the intra-regional coefficients are higher in each case.

Examples of the correlations of one intra-regional pair and one inter-regional pair can be seen in figure 3.3.

Secondly, we separated those pairs into intra-regional and inter-regional groups. We noted that the mean intra-regional correlations (coloured dots in figures 3.6a and 3.6b) for a given region tended to be higher than the mean inter-regional correlations (black dots in figures 3.6a and 3.6b) involving cells from that region. However, in contrast with our previous result, we noted that the difference between the mean intra-regional correlations and most highly correlated inter-regional correlations reduced as we increased the time bin width (see figures 3.6a and 3.6b). This shows that the mean correlations shown in figure 3.5 are not distributed evenly across all region pair combinations.



(A) Mean inter-regional and intra-regional correlations using a time bin width of 5ms.

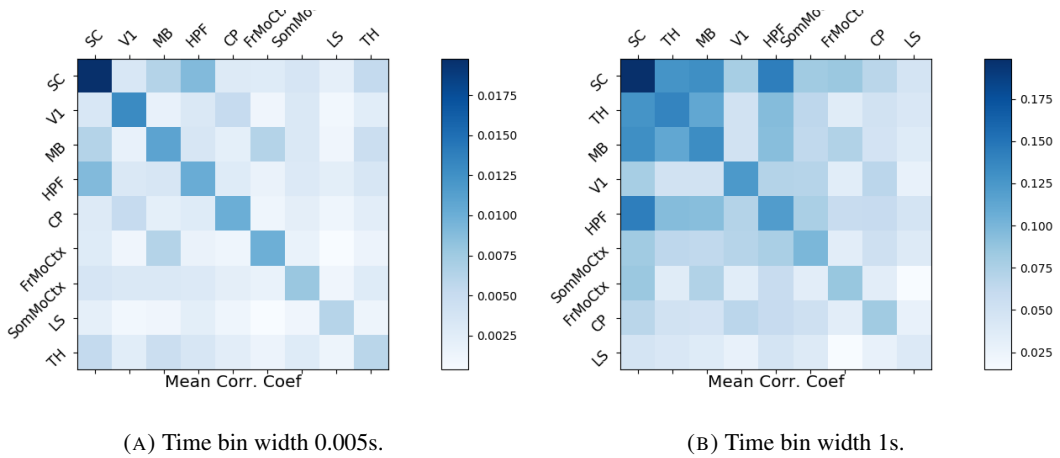


(B) Mean inter-regional and intra-regional correlations using a time bin width of 1s.

FIGURE 3.6: The mean intra-regional correlations (coloured dots) and mean inter-regional correlations (black dots) for a given region, indicated on the x-axis, for different time bin widths. Each black dot represents the mean inter-regional correlations between the region indicated on the x-axis and one other region. (A) shows these measurements when we used a time bin width of 5ms. (B) shows these measurements when we used a time bin width of 1s. Note that the difference between the mean inter-regional correlations and mean intra-regional correlations is smaller for 1s bins.

Finally, to see these regional mean correlations in a bit more detail, to examine the individual pair combinations in particular, we displayed these data in a matrix of mean correlations (see figure 3.7), showing the mean intra-regional correlations on the main diagonal, and the mean inter-regional correlations off diagonal. Comparing a version of this figure created using a short time bin width of 5ms (figure 3.7a) and a version using a longer time bin width of 1s (figure 3.7b) we observed that the mean intra-regional correlations are always relatively high in comparison to the mean inter-regional correlations, but the mean correlations in some inter-regional pairs are relatively much higher when using the longer time bin width.

This could indicate information being processed quickly at a local or within-region level, and the local representations of this information spreading between regions at longer timescales.



(A) Time bin width 0.005s.

(B) Time bin width 1s.

FIGURE 3.7: Mean inter-regional (main diagonal) and intra-regional (off diagonal) correlation coefficients. (A) Shows these measurements when spike times were binned using 5ms time bins. (B) Shows the same, using 1s time bins. Note that the matrices are ordered according to the main diagonal values, therefore the ordering is different in each subfigure.

These results were consistent across the three mouse subjects. But, the relative magnitudes of the mean intra-regional and inter-regional correlations were not consistent. For example, the region with the highest mean intra-regional correlations when using 1s bin widths for subject one is the superior colliculus (SC), but for subject two it is the midbrain (MB).

3.4.4 Connected and divided structure in correlation based networks reduces in dimension with increasing bin width

We used the correlation measurements to create weighted undirected graphs/networks where each node represents a neuron, and the weight of each edge is the pairwise correlation between those neurons represented by the nodes at either end of that edge. We aimed to find

1565 communities of neurons within these networks, and compare the structure of these communities
1566 to the anatomical division of those neurons. The first step of this process involved
1567 applying the ‘spectral rejection’ technique developed by Humphries et al (2019) (Humphries
1568 et al., 2019). This technique compares our data network to a chosen null network model, and
1569 finds any additional structure in the data network beyond that which is captured in the null
1570 network model (if there is any such structure).

1571 By comparing the eigenspectrum of the data network to the eigenspectrum of many samples
1572 from the null network model, this technique allows us to estimate the dimensionality of
1573 the additional structure in the data network, and gives us a basis for that vector space. It also
1574 divides the additional structure into connected structure, and k -partite (or divided) structure.
1575 For example, if our algorithm found two dimensions of additional connected structure, and
1576 one dimension of additional divided structure. We might expect to find three communities,
1577 that is groups more strongly connected within group than without, and we might expect to
1578 find bi-partite structure, that is two sets that are more strongly connected between groups
1579 than within groups.

1580 The technique also finds which nodes contribute to this additional structure, and divides
1581 our data network into signal and noise networks. The details of spectral rejection and node
1582 rejection can be found in sections 3.3.5 and 3.3.5 respectively, and a full overview can be
1583 found in (Humphries et al., 2019).

1584 We chose the sparse weighted configuration model (see section 3.3.5) as our null network
1585 model. This model matches the sparsity and the total weight of the original network but
1586 distributes the weight at random across the sparse network.

1587 We applied the spectral rejection method to our networks based on total correlations using
1588 different values for the time bin width. We observed that for smaller time bin widths, our data
1589 networks had both k -partite structure, and community structure. As the width of the time bin
1590 increased, we found that the k -partite structure disappeared from our data networks, and the
1591 dimension of the community structure reduced in two of the three mice from which we had
1592 data (see figure 3.8).

1593 3.4.5 Detecting communities in correlation based networks

1594 We applied the community detection procedure described in section 3.3.5 to our signal net-
1595 works for our various time bin widths. We detected a greater number of smaller communities
1596 at shorter time bin widths, and a smaller number of larger communities for longer time bin
1597 widths (see figure 3.9). This was expected after the results found in section 3.4.4. We found

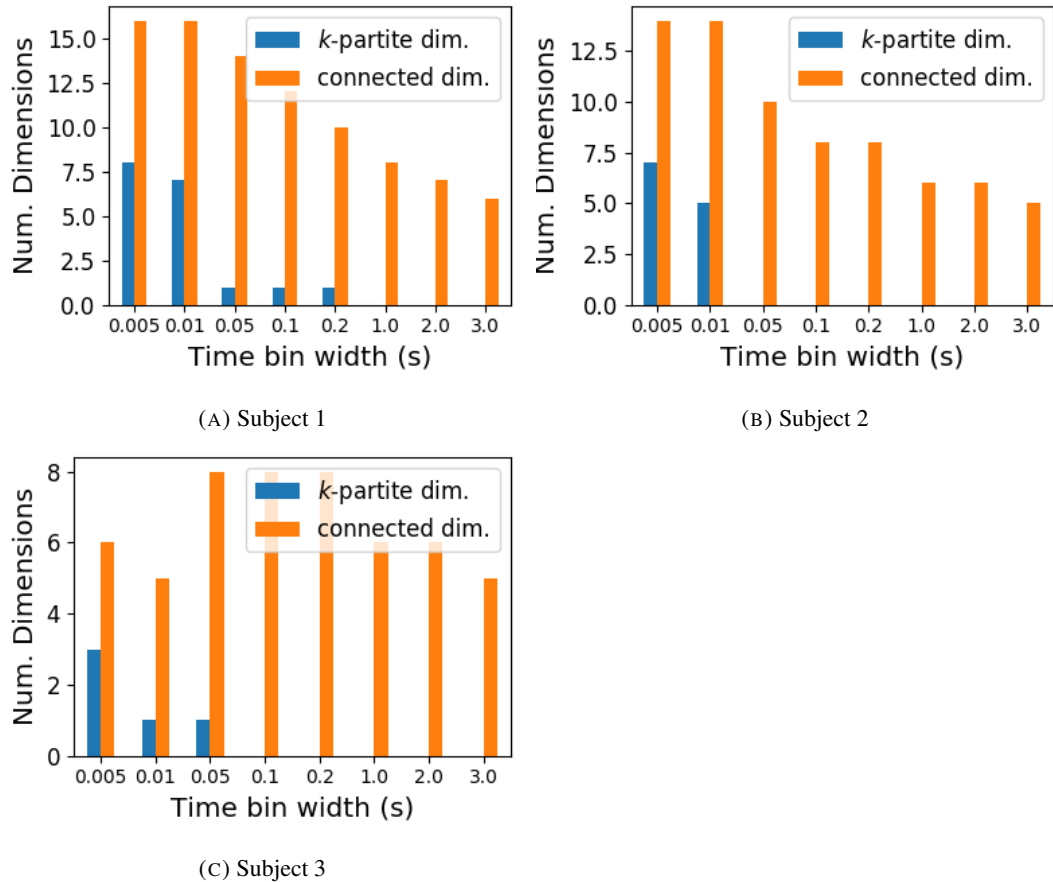


FIGURE 3.8: The number of dimensions in the *k*-partite and connected structure in the correlation based networks beyond the structure captured by a sparse weighted configuration null network model (see section 3.3.5), shown for different time bin widths. Note that the *k*-partite structure disappears for time bin width greater than 200ms for all three subjects. The dimension of the connected structure reduces with increasing bin width for 2 of the 3 subjects (top row).

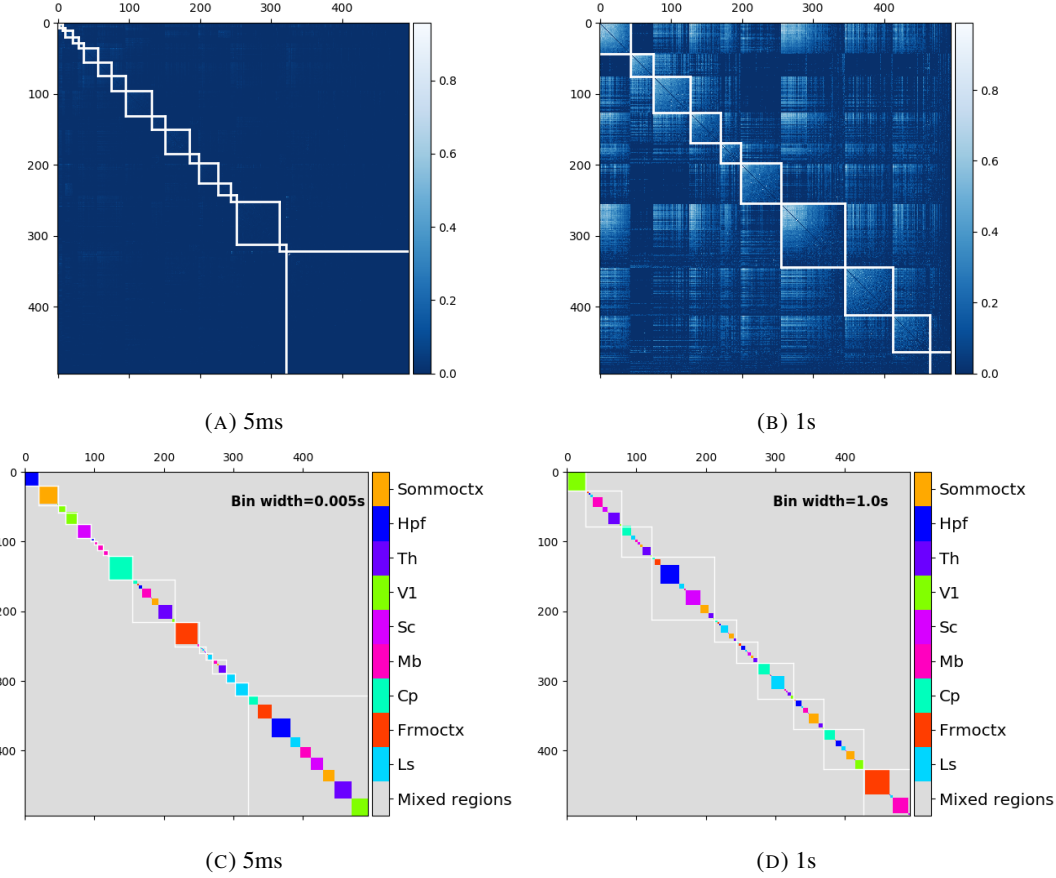


FIGURE 3.9: (A-B) Correlation matrices with detected communities indicated by white lines. Each off main diagonal entry in the matrix represents a pair of neurons. Those entries within a white square indicate that both of those neurons are in the same community as detected by our community detection procedure. Matrices shown are for 5ms and 1s time bin widths respectively. Main diagonal entries were set to 0. (C-D) Matrices showing the anatomical distribution of pairs along with their community membership. Entries where both cells are in the same region are given a colour indicated by the colour bar. Entries where cells are in different regions are given the grey colour also indicated by the colour bar.

1598 more dimensions of additional structure at shorter time bin widths, therefore we found more
1599 communities at shorter time bin widths.

1600 We also noticed that at short time bin widths the communities detected tended to be
1601 dominated by cells from one region. Whereas communities existing in networks created
1602 using wider time bin widths tended to contain cells from many different brain regions. More
1603 on this in the next section.

1604 **3.4.6 Functional communities resemble anatomical division at short timescales**

1605 In order to quantify the similarity of the communities detected to the anatomical division of
1606 the cells. We treated both the anatomical division and the communities as clusterings of these
1607 cells. We then used measures for quantifying the difference or similarity between clusterings
1608 to quantify the difference or similarity between the detected communities and the anatomical
1609 division. Details of these measures can be found in section 3.3.6 or in (Vinh, Epps, and
1610 Bailey, 2010).

1611 We used two different types of measures for clustering comparison; information based
1612 measures (see section 3.3.6) and pair counting based measures (see section 3.3.6). We include
1613 one example of each in figure 3.10.

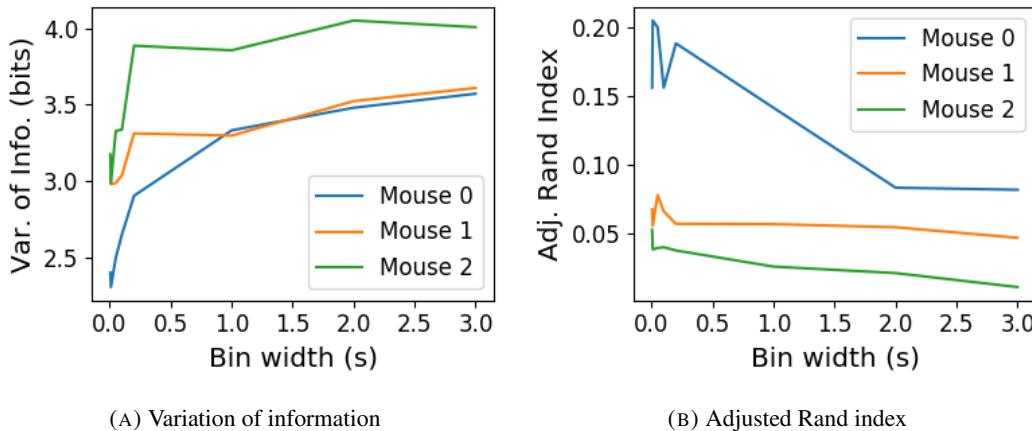
1614 The variation of information is the information based measure included in figure 3.10a.
1615 This measure forms a metric on the space of clusterings. The larger the value for the variation
1616 of information, the more different the clusterings.

1617 The adjusted Rand index is the pair counting based measure included in figure 3.10b. In
1618 contrast with the variation of information, the adjusted Rand index is a normalised similarity
1619 measure. The adjusted Rand index takes value 1 when the clusterings are identical, and takes
1620 value 0 when the clusterings are no more similar than chance.

1621 Both measures indicated that the detected communities and the anatomical division of
1622 the cells were more similar when we used shorter time bins widths (see figure 3.10). This
1623 indicates that correlated behaviour in neuronal ensembles is more restricted to individual
1624 brain regions at short timescales (< 250ms), and the correlated activity spreads out across
1625 brain regions over longer time scales.

1626 **3.4.7 Conditional correlations & signal correlations**

1627 In light of the excellent research of Stringer et al (2019) showing that spontaneous behaviours
1628 can drive activity in neuronal ensembles across the visual cortex and midbrain (Stringer et
1629 al., 2019), we decided to control for the mouse's behaviour when performing our analyses.



(A) Variation of information

(B) Adjusted Rand index

FIGURE 3.10: (A) The variation of information is a measure of distance between clusterings. The distance between the anatomical ‘clustering’ and community detection ‘clustering’ increases with increasing time bin width. (B) The adjusted Rand index is a normalised similarity measure between clusterings. The anatomical and community detection clusterings become less similar as the time bin width increases.

1630 It is possible that our community detection process may be detecting communities across
 1631 multiple brain regions at longer time scales due to aggregating neuronal activity driven by
 1632 several spontaneous behaviours occurring during the time interval covered by a given time
 1633 bin. A time bin of 1s, for example, could contain a spike count where those spikes were driven
 1634 by different spontaneous behaviours. We aimed to investigate this possibility by applying our
 1635 community detection analysis to conditional correlation measures.

1636 We used the top 500 principal components of a video of the mouse’s face as a measure of
 1637 the mouse’s behaviour (see section 3.2.2). We modelled the spike counts as a linear combi-
 1638 nation of the principal components using linear regression with ElasticNet regularisation (see
 1639 section 3.3.3). Using this model, we quantified the expected spike count given the mouse’s
 1640 behaviour $E[X|Z_1, \dots, Z_{500}]$.

1641 We used these expected values to measure $\text{cov}(E[X|Z], E[Y|Z])$, and we used that value,
 1642 the covariance $\text{cov}(X, Y)$, and the *law of total covariance* (see section 3.3.3) to measure
 1643 $E[\text{cov}(X, Y|Z)]$. Here X and Y represent spike counts from individual cells, and Z is short-
 1644 hand for the 500 principal components mentioned above. The two components of the co-
 1645 variance, $\text{cov}(E[X|Z], E[Y|Z])$ and $E[\text{cov}(X, Y|Z)]$, represent a ‘signal covariance’ and ex-
 1646 pected value of a ‘spike count covariance’ respectively, analogous to the signal correlation
 1647 and spike count correlation (Cohen and Kohn, 2011).

1648 We examined the means of these components for different values of the time bin width
 1649 (see figure 3.11). We observed a consistent increase in $E[\text{cov}(X, Y|Z)]$ as the time bin width
 1650 increased. But we saw different trends for $\text{cov}(E[X|Z], E[Y|Z])$ for each mouse.

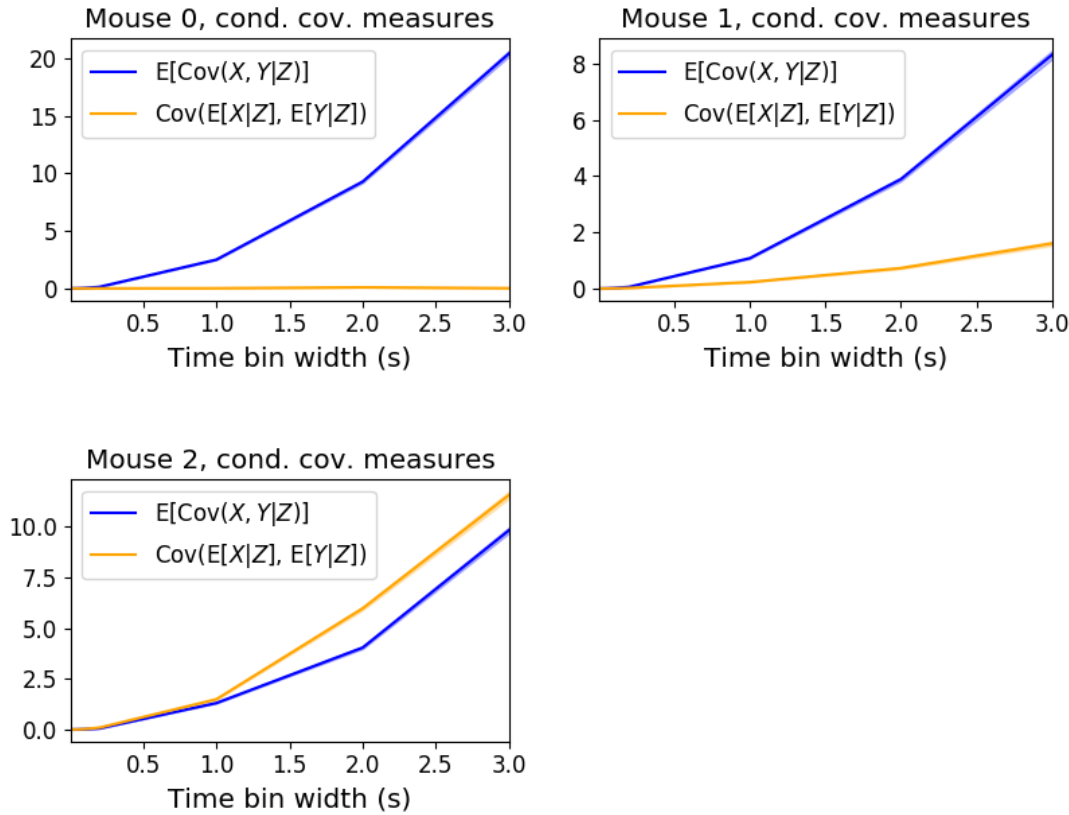


FIGURE 3.11: Comparing the components of the total covariance across different values for the time bin width. We observed a consistent increase in $E[\text{cov}(X, Y|Z)]$ as the time bin width increased. But we saw different trends for $\text{cov}(E[X|Z], E[Y|Z])$ for each mouse.

1651 Using $\text{cov}(E[X|Z], E[Y|Z])$ we measured the signal correlation, ρ_{signal} , and using $E[\text{cov}(X, Y|Z)]$
 1652 we measured the event conditional correlation, $\rho_{X,Y|Z}$ (see section 3.3.3 for more details).
 1653 We saw a consistent increase in $\rho_{X,Y|Z}$ as the time bin width increased, this corresponds to
 1654 the result for $E[\text{cov}(X, Y|Z)]$. We observed different trends for ρ_{signal} for each mouse, this
 1655 corresponds to the result for $\text{cov}(E[X|Z], E[Y|Z])$.

1656 We applied our network noise rejection and community detection process to networks
 1657 based on the spike count correlations $\rho_{X,Y|Z}$ and the signal correlations ρ_{signal} . We noted that
 1658 the community detection on $\rho_{X,Y|Z}$ behaved similarly to the community detection on the total
 1659 correlation. We can see this in figures 3.13a and 3.13b. At very short time bin widths, we
 1660 detect more communities, and those communities often contain cells from one brain region
 1661 only. At longer time bin widths, we detect fewer communities, and those communities tend
 1662 to contain cells from multiple brain regions. When we examine the distance between (or
 1663 similarity between) the anatomical division of the cells, and the detected communities we
 1664 notice that the two clusterings are more similar at shorter time bin widths (see figure 3.14).

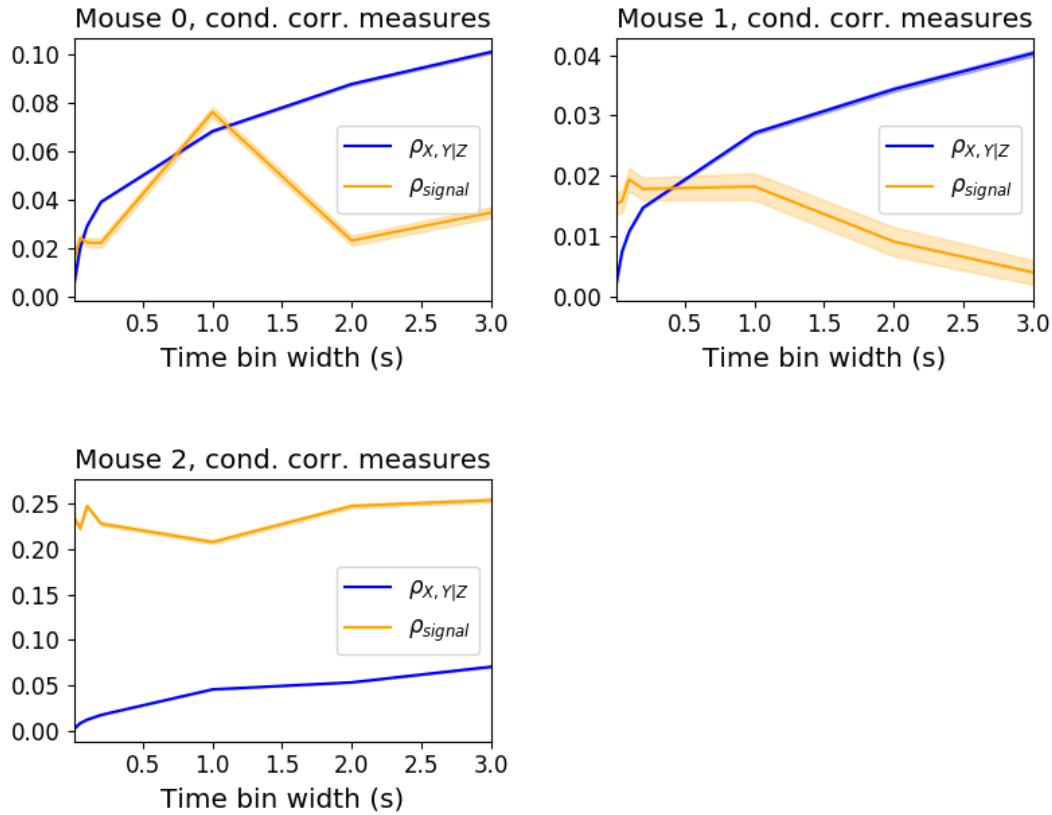


FIGURE 3.12: Comparing the components of the total covariance across different values for the time bin width. We saw a consistent increase in $\rho_{X,Y|Z}$ as the time bin width increased in all three subjects. But we saw different trends in ρ_{signal} for each of the subjects.

When we applied the network noise rejection and community detection process to the networks based on the signal correlations ρ_{signal} we found the number of communities we detected reduced with increasing time bin width. But the number of communities detected was less than that for the total correlations or the spike count correlations. The communities detected always tended to contain cells from multiple regions at both short and long timescales (see figures 3.13c and 3.13d). The communities detected bore very little relation to the anatomical division of the cells. The adjusted Rand index between the community clustering and the anatomical ‘clustering’ is close to zero for every time bin width (see figure 3.15b). This indicates that the similarity between the clusterings is close to chance. We did observe a slight downward trend in the variation of information with increasing bin width (see figure 3.15a), but this is more likely due to a decrease in the number of communities detected rather than any relationship with anatomy.

We also observed that the network noise rejection process rejected some of the cells when applied to the network based on the signal correlations. This means that those cells

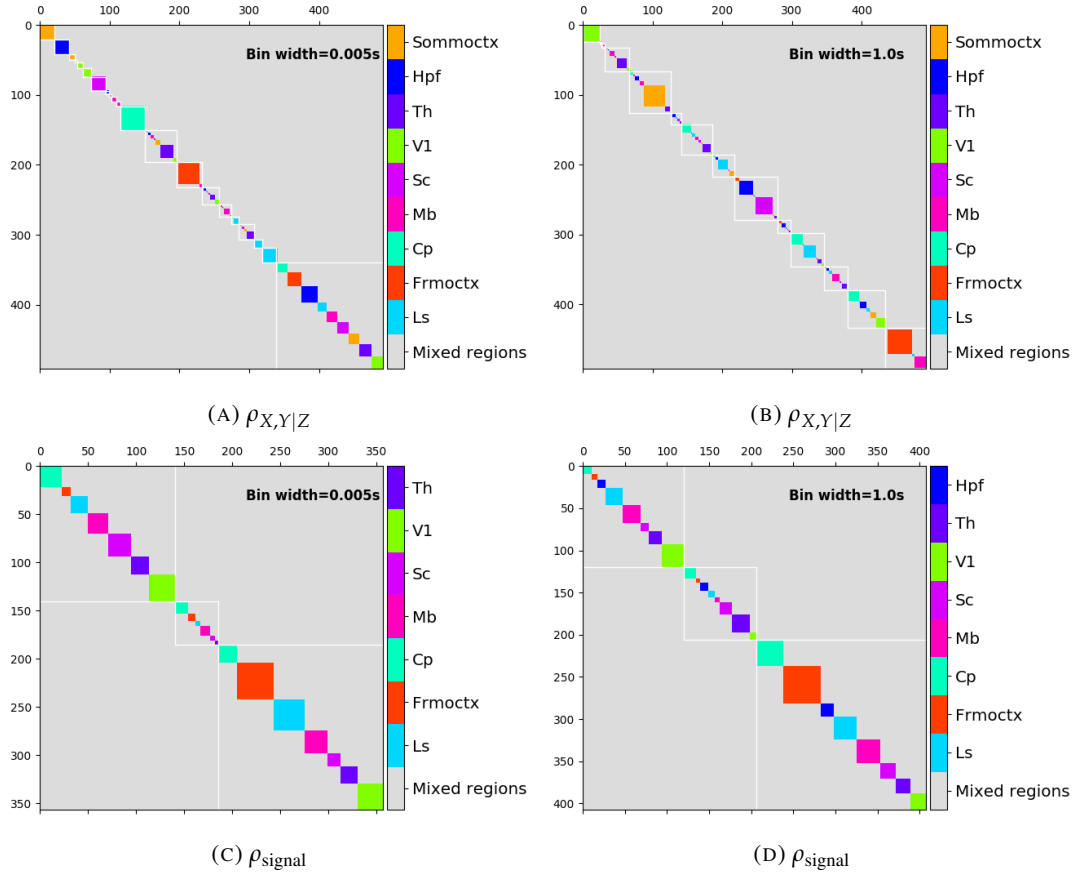


FIGURE 3.13: Matrices showing the regional membership of pairs by colour, and the communities in which those pairs lie. (A-B) Detected communities and regional membership matrix for network based on rectified spike count correlation $\rho_{X,Y|Z}$, using time bin widths of 0.005s and 1s respectively. (C-D) Detected communities and regional membership matrix for network based on rectified signal correlation ρ_{signal} , using time bin widths of 0.005s and 1s respectively.

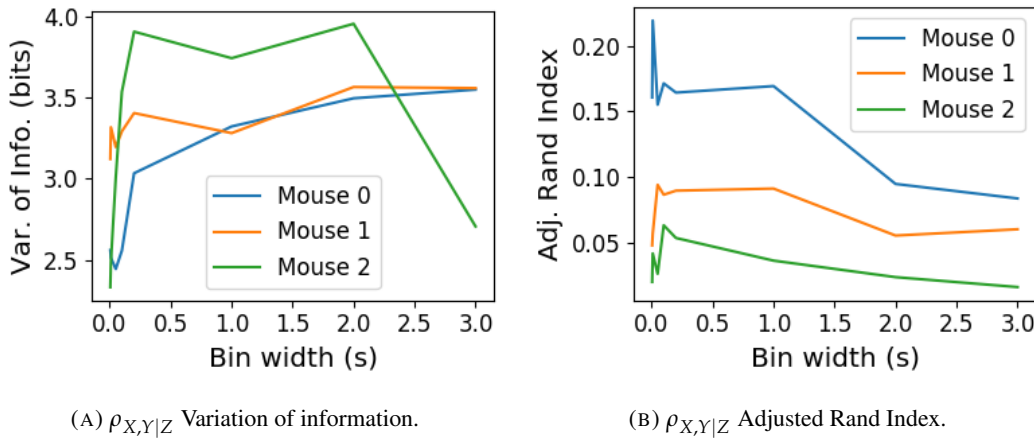
(A) $\rho_{X,Y|Z}$ Variation of information.(B) $\rho_{X,Y|Z}$ Adjusted Rand Index.

FIGURE 3.14: Distance and similarity measures between the anatomical division of the neurons, and the communities detected in the network based on the spike count correlations $\rho_{X,Y|Z}$. (A) The variation of information is a ‘distance’ measure between clusterings. The distance between the anatomical ‘clustering’ and the community clustering increases as the time bin width increases. (B) The adjusted Rand index is a similarity measure between clusterings. The detected communities become less similar to the anatomical division of the cells as the time bin width increases.

1679 did not contribute to the additional structure of the network beyond that captured by the
 1680 sparse weighted configuration model. This is why the matrices in figures 3.13c and 3.13d are
 1681 smaller than their analogues in figures 3.13a and 3.13b.

1682 3.4.8 Absolute correlations and negative rectified correlations

1683 At the moment, the network noise rejection protocol can only be applied to weighted undi-
 1684 rected graphs with non-negative weights. This meant that we had to rectify our correlated
 1685 networks before applying the network noise rejection and community detection process. We
 1686 wanted to investigate what would happen if instead of rectifying the correlations, we used the
 1687 absolute value, or reversed the signs of the correlations and then rectified.

1688 When we used the absolute value of the correlations, we found very similar results to
 1689 those shown above for the rectified total correlations and the rectified spike count corre-
 1690 lations. We detected more communities using shorter bin widths, and these communities
 1691 were more similar to the brain’s anatomy than those communities detected using a longer bin
 1692 width (see figure 3.16). The only exception being that we detected more communities. This
 1693 could indicate that we detected both positively and negatively correlated communities, but
 1694 we haven’t done any further investigation so we cannot say for sure.

1695 When we used the sign reversed rectified correlated networks, we tended to find fewer
 1696 communities. Each community contained cells from many different anatomical regions, at

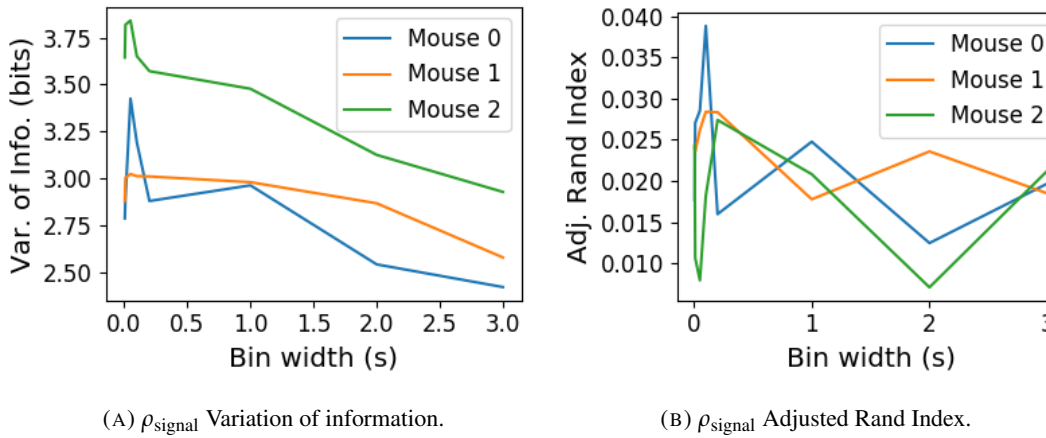


FIGURE 3.15: Distance and similarity measures between the anatomical division of the neurons, and the communities detected in the network based on the signal correlations ρ_{signal} . (A) The variation of information is a ‘distance’ measure between clusterings. The distance between the anatomical ‘clustering’ and the community clustering increases as the time bin width increases. (B) The adjusted Rand index is a similarity measure between clusterings. The detected communities become less similar to the anatomical division of the cells as the time bin width increases.

1697 both long and short bin widths (see figures 3.17a, 3.17b, 3.17c, 3.17d). The communities
 1698 bore little relation to the anatomical distribution of the cells, this can be seen in figure 3.17f,
 1699 the values close to zero indicate that the similarity between the two clusterings are around
 1700 chance level. This indicates that there was not much structure in the negatively correlated
 1701 networks beyond that captured by the sparse weighted configuration model.

1702 3.5 Discussion

1703 It is well established that the brain uses correlated behaviour in neuronal ensembles to repre-
 1704 sent the information taken in through sensation (Cohen and Maunsell, 2009; Litwin-Kumar,
 1705 Chacron, and Doiron, 2012; deCharms and Merzenich, 1996). However, most studies that
 1706 examine the nature of these correlations in-vivo, study an ensemble of cells from only one
 1707 or two brain regions (Cohen and Kohn, 2011; Wierzynski et al., 2009; Patterson et al., 2014;
 1708 Girard, Hupé, and Bullier, 2001). Furthermore, recent results have shown that behaviour can
 1709 drive correlated activity in multiple brain regions, including those not normally associated
 1710 with motor control (Stringer et al., 2019; Gründemann et al., 2019; Allen et al., 2019). In this
 1711 study, we utilised one of the newly recorded large datasets containing electrophysiological
 1712 recordings from multiple brain regions simultaneously. We investigated correlated behaviour
 1713 in these different brain regions and we investigated correlated behaviour between neurons in
 1714 different regions, during spontaneous behaviour.

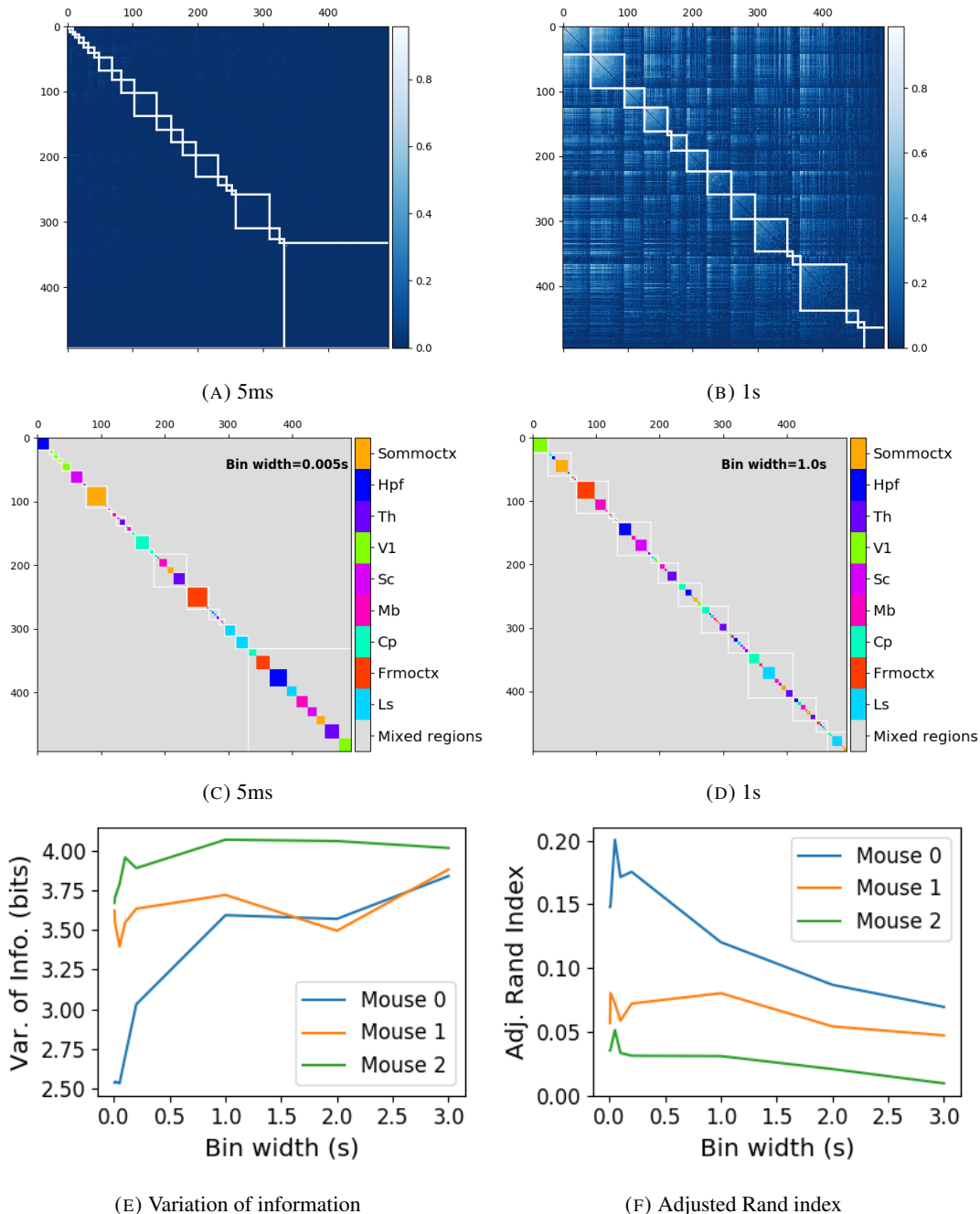


FIGURE 3.16: (A-B) Absolute correlation matrices with detected communities indicated by white lines. These communities are based on the absolute value of the total correlation between each pair of cells. Those entries within a white square indicate that both of those neurons are in the same community. Matrices shown are for 5ms and 1s time bin widths respectively. Main diagonal entries were set to 0. (C-D) Matrices showing the anatomical distribution of pairs along with their community membership. Regional membership is indicated by the colour bar. (E) Variation of information between the anatomical division of the cells, and the detected communities. (F) Adjusted Rand index between the anatomical division, and the detected communities.

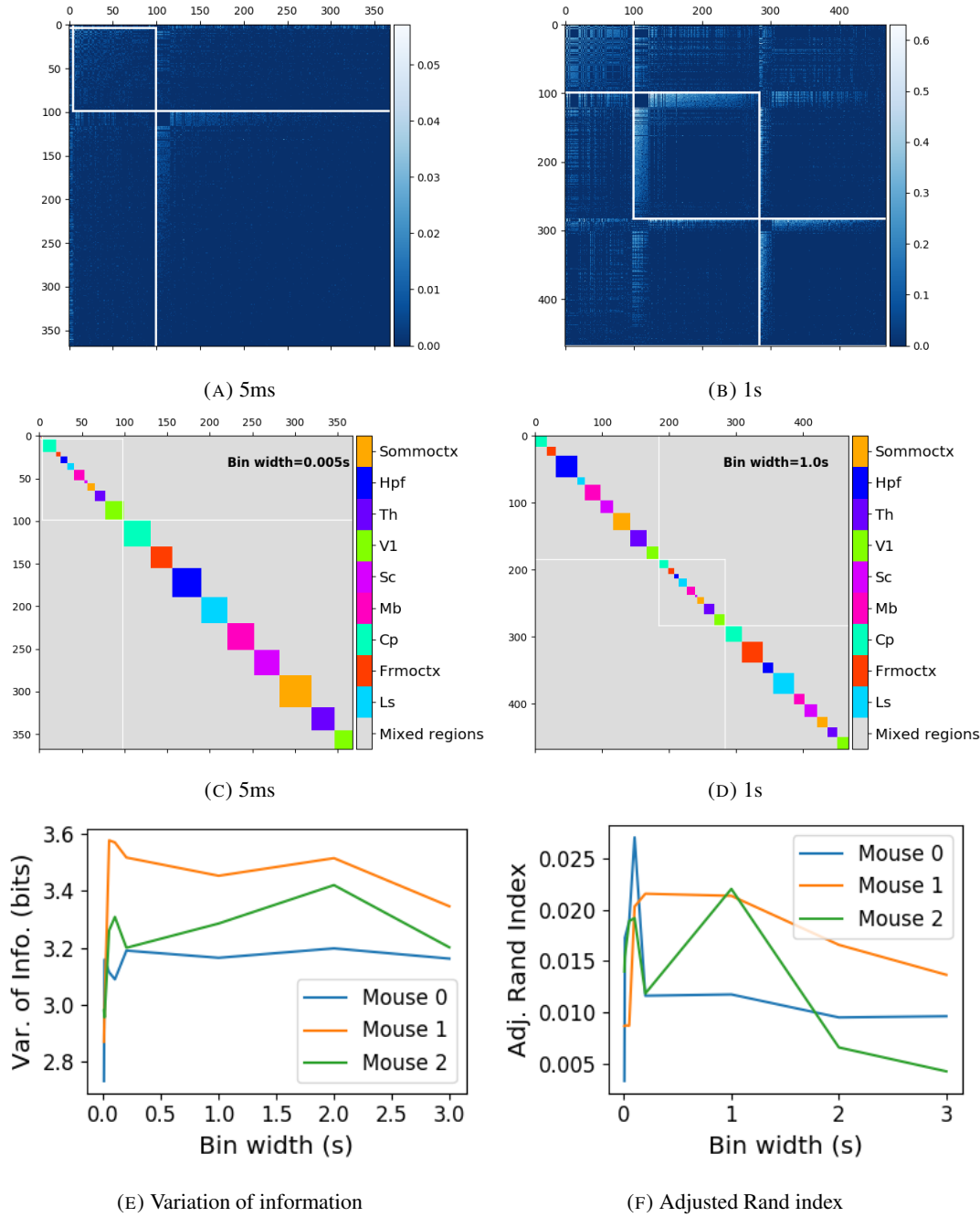


FIGURE 3.17: (A-B) Sign reversed rectified correlation matrices with detected communities indicated by white lines. Those entries within a white square indicate that both of those neurons are in the same community. Matrices shown are for 5ms and 1s time bin widths respectively. Main diagonal entries were set to 0. (C-D) Matrices showing the anatomical distribution of pairs along with their community membership. Regional membership is indicated by the colour bar. (E) Variation of information between the anatomical division of the cells, and the detected communities. (F) Adjusted Rand index between the anatomical division, and the detected communities.

1715 A number of studies have found that the timescale of correlated behaviour induced by a
1716 stimulus can be modulated by the stimulus structure and behavioural context. For example,
1717 the spike train correlations between cells in weakly electric fish are modulated by the spa-
1718 tial extent of the stimulus (Litwin-Kumar, Chacron, and Doiron, 2012), and neurons in the
1719 marmoset primary auditory cortex modulate their spike timing (and therefore correlation) in
1720 response to stimulus features without modulating their firing rate (deCharms and Merzenich,
1721 1996). Furthermore, the width of the time bins over which spike counts are measured has
1722 been shown to have an effect on the magnitude of those correlations (Cohen and Kohn, 2011).
1723 Despite this, very little research has been done comparing correlation measures from the same
1724 dataset at different timescales. We investigated this by varying the time bin width used to bin
1725 spike times into spike counts from as short as 5ms up to 3s.

1726 In order to further investigate the effect of these correlations at different timescales, we
1727 regarded our neuronal ensemble as a weighted undirected graph, where each neuron is rep-
1728 resented by a node, and the weight on each edge is the correlation between the neurons
1729 connected by that edge. We then applied a novel clustering method from network science
1730 (Humphries et al., 2019) to identify communities in these networks. Communities in a net-
1731 work graph refer to sets of nodes that are more strongly connected to each other than the
1732 nodes outside of their set. Another way to put this is to say that the nodes in a community
1733 are more strongly connected than *expected*. What connection strength might be expected is
1734 defined by a null network model. We chose a null network model that matched the sparsity
1735 and total strength of our correlation based data networks. So, if two cells were in the same
1736 community, those cells were more correlated than would be expected given the correlation
1737 strength of their ensemble.

1738 These networks, and the community detection process, were completely agnostic of the
1739 anatomical division of the cells in our ensemble. When we compared the detected commu-
1740 nities with the anatomical division of the cells using distance and similarity measures for
1741 clusterings, we found that the detected communities were more similar to the anatomical
1742 division at shorter timescales. That is, when we used a wider time bin to count spikes, and
1743 computed pairwise correlations with these spike counts, the correlated communities tended to
1744 exist within anatomical regions at shorter timescales, and tended to span anatomical regions
1745 at longer timescales. This could reflect localised functional correlations at short time scales
1746 rippling outwards across brain regions at longer timescales. The brain may be processing
1747 some information quickly locally, and carrying out further, perhaps more detailed, represen-
1748 tation over a longer timescale across many regions using the representations that were just

1749 built locally.

1750 These changes in communities across timescales could also be driven by the anatomy
1751 of the individual cells. For example, it may simply take longer to transmit action potentials
1752 over longer distances, hence correlated activity over longer timescales will exist between
1753 anatomical regions, rather than within. However, the switch to almost exclusively multi-
1754 regional functional networks at 1s bin widths, rather than a mixture of multi-region, and
1755 single-region suggests that the inter-regional correlations either overpower, or inhibit the
1756 local correlations. So there may be more at play than just timescales.

1757 We acknowledged that the region spanning correlated communities that we detected at
1758 longer time scales could exist due to collating activity driven by distinct spontaneous activi-
1759 ties. In order to account for this, we modelled the spike counts as a linear function of the
1760 top 500 principal components of a video of the mouse’s face filmed simultaneously with the
1761 electrophysiological readings. We applied our network noise rejection and community de-
1762 tection process to the weighted undirected networks formed by the spike count correlations
1763 (or noise correlations) and the signal correlations that we calculated using our model. For the
1764 spike count correlation networks, we found much the same results as for the total correlations
1765 as described above. For the signal correlations, the communities detected in these networks
1766 bore little relation to the anatomical division of the cells. Recent findings have shown that
1767 behavioural data accounts for correlations in many brain regions that would otherwise be
1768 dismissed as noise (Stringer et al., 2019), our finding to shows that these correlations are still
1769 governed by the timescale division between local communication and across-region commu-
1770 nication.

1771 There is a lot of room for further investigation based on this research. For a start, the
1772 data that we used here were collected from nine different regions in the mouse brain, but
1773 none of these regions were part of the somatosensory cortex. Given that a mouse experiences
1774 so much of its environment through its sense of smell, some data from this region would be
1775 interesting to investigate. On the same theme, the mice in the experiment from which the
1776 data were collected were headfixed and placed on a rotating ball, but were otherwise behav-
1777 ing spontaneously. Had these mice been exposed to a visual, aural, or olfactory stimulus,
1778 we could have examined the responses of the cells in the brain regions corresponding to vi-
1779 sion, hearing, and olfaction, and compared these responses to the responses from the other
1780 brain regions. Furthermore, we could have investigated the interaction between the sets of
1781 responses.

1782 Another space for further investigation is the community detection. The algorithm that we

1783 used here never detects overlapping communities. But functional communities could indeed
1784 have overlaps. Clustering methods that detect overlapping clusters do exist (Baadel, Thabtah,
1785 and Lu, 2016). Applying one of those algorithms could yield some interesting results. Also,
1786 the community detection algorithm that we used here cannot process graphs with negative
1787 weights, this forced us to separate positive and negative correlations before applying our
1788 network noise rejection and community detections process, or use the absolute value of our
1789 correlations. A community detection algorithm that can work on weighted undirected graphs
1790 with negative weights could yield some interesting results here.

1791 **Chapter 4**

1792 **A simple two parameter distribution
for modelling neuronal activity and
capturing neuronal association**

1795 *Abstract*

1796 Recent developments in electrophysiological technology have lead to an increase in the size
1797 of electrophysiology datasets. Consequently, there is a requirement for new analysis tech-
1798 niques that can make use of these new datasets, while remaining easy to use in practice. In
1799 this work, we fit some one or two parameter probability distributions to spiking data collected
1800 from a mouse exposed to visual stimuli. We show that the Conway-Maxwell-binomial dis-
1801 tribution is a suitable model for the number of active neurons in a neuronal ensemble at any
1802 given moment. This distribution fits these data better than binomial or beta-binomial distribu-
1803 tions. It also captures the correlated activity in the primary visual cortex induced by stimulus
1804 onset more effectively than simply measuring the correlations, at short timescales (< 10ms).
1805 We also replicate the finding of Churchland et al (2010) relating to stimulus onset quenching
1806 neural variability in cortical areas, and we show a correspondence between this quenching
1807 and changes in one of the parameters of the fitted Conway-Maxwell-binomial distributions.

4.1 Introduction

Recent advances in electrophysiological technology, such as ‘Neuropixels’ probes (Jun et al., 2017) have allowed extracellular voltage measurements to be collected from larger numbers of cells than traditional methods, in multiple brain regions simultaneously, and routinely. These larger datasets require innovative methods to extract information from the data in a reasonable amount of time, ‘reasonable’ being subjective in this case.

Theoretically, all the information at any given moment in an electrophysiological dataset with n neurons could be captured by calculating the probability distribution for every possible spiking pattern. This would require defining a random variable with 2^n possible values, a task that quickly becomes impossible as n increases. Attempts at approximating this random variable often involve measuring pairwise or higher order correlations (Schneidman et al., 2006; Flach, 2013; Ganmor, Segev, and Schneidman, 2011). But pairwise correlations may not be enough to characterise instantaneous neural activity (Tkačik et al., 2014). Furthermore, these kinds of models tend to ignore the temporal structure of neuronal data, in favour of smaller model size, and scalability.

Higher order correlations would be helpful here, but defining these correlations can be tricky, never-mind quantifying them. If we use the interaction parameters arising from the exponential family model as measures of higher order correlations, measuring these correlations becomes computationally impractical quite quickly also (the number of ‘three neuron correlations’ to measure scales with $(n)_3$). In this paper, we dispense with measuring correlations directly, and attempt to characterise correlated behaviour by measuring ‘association’; a more general concept that includes correlation.

In this work, we examined the ability of simple distributions to model the number of active (spiking) neurons in a neuronal ensemble at any given timepoint. We compared a little-known distribution named the Conway-Maxwell-binomial distribution to the binomial distribution and the beta-binomial distribution. The binomial distribution is a probability distribution over the number of successes in a sequence of independent and identical Bernoulli trials. The beta-binomial distribution is similar, but allows for a bit more flexibility while still being a model for heterogeneity. Similar to the binomial and beta-binomial, the Conway-Maxwell-binomial distribution is a probability distribution over the number of successes in a series of Bernoulli trials, but allows over- and under-dispersion relative to the binomial distribution. This distribution should therefore be a good candidate for our purposes. We found that Conway-Maxwell-binomial distribution was usually the best candidate of the three that

1841 we examined.

1842 We also observed some interesting changes in the number of active neurons in the primary
1843 visual cortex and hippocampus at stimulus onset and some changes in this activity in the
1844 thalamus which were sustained for the full duration of the stimulus presentation. This let us
1845 know that there were some responses to model.

1846 We found that fitting a Conway-Maxwell-binomial distribution was a better method of
1847 capturing association between neurons than measuring the spike count correlation for the
1848 short time bins that we used (< 10ms).

1849 Finally, we also wanted to investigate parallels between the parameters of the Conway-
1850 Maxwell-binomial distribution and quantities that have been established as relevant to sen-
1851 sory processing. So, we replicated the findings made by Churchland et al. (2010) relating
1852 to a reduction in neural variability at stimulus onset in the macaque cortical regions, but for
1853 data taken from the mouse primary visual cortex. We compared these findings to the values
1854 of the fitted Conway-Maxwell-binomial distribution parameters.

1855 4.2 Data

1856 We used data collected by Nick Steinmetz and his lab ‘CortexLab at UCL’ (Steinmetz, Caran-
1857 dini, and Harris, 2019). The data can be found online ¹ and are free to use for research
1858 purposes.

1859 Two ‘Phase3’ Neuropixels (Jun et al., 2017) electrode arrays were inserted into the brain
1860 of an awake, head-fixed mouse for about an hour and a half. These electrode arrays recorded
1861 384 channels of neural data each at 30kHz and less than $7\mu\text{V}$ RMS noise levels. The sites
1862 are densely spaced in a ‘continuous tetrode’-like arrangement, and a whole array records
1863 from a 3.8mm span of the brain. One array recorded from visual cortex, hippocampus, and
1864 thalamus, the other array recorded from motor cortex and striatum. The data were spike-
1865 sorted automatically by Kilosort and manually by Nick Steinmetz using Phy. In total 831
1866 well-isolated individual neurons were identified.

1867 4.2.1 Experimental protocol

1868 The mouse was shown a visual stimulus on three monitors placed around the mouse at right
1869 angles to each other, covering about ± 135 degrees azimuth and ± 35 degrees elevation.

¹<http://data.cortexlab.net/dualPhase3/>

1870 The stimulus consisted of sine-wave modulated full-field drifting gratings of 16 drift di-
1871 rections ($0^\circ, 22.5^\circ, \dots, 337.5^\circ$) with 2Hz temporal frequency and 0.08 cycles/degree spatial
1872 frequency displayed for 2 seconds plus a blank condition. Each of these 17 conditions were
1873 presented 10 times in a random order across 170 different trials. There were therefore 160
1874 trials with a drifting-grating visual stimulus present, and 10 trials with a blank stimulus.

1875 **4.3 Methods**

1876 **4.3.1 Binning data**

1877 We converted the spike times for each cell into spike counts by putting the spike times into
1878 time bins of a given ‘width’ (in milliseconds). We used time bins of 1ms, 5ms, and 10ms.
1879 We used different time bin widths to assess the impact of choosing a bin width.

1880 **4.3.2 Number of *active* neurons**

1881 To count the number of active neurons in each neuronal ensemble, we split the time interval
1882 for each trial into bins of a given width. We counted the number of spikes fired by each cell
1883 in each bin. If a cell fired *at least* one spike in a given bin, we regarded that cell as active in
1884 that bin. We recorded the number of active cells in every bin, and for the purposes of further
1885 analysis, we recorded each cell’s individual spike counts.

1886 It should be noted that when we used a bin width of 1ms, the maximum number of
1887 spikes in any bin was 1. For the wider time bins, some bins had spike counts greater than
1888 1. Consequently when using a bin width of 1ms, the number of active neurons and the total
1889 spike count of a given bin were identical. But for wider bin widths, the total spike count was
1890 greater than the number of active neurons.

1891 So for the 1ms bin width, the activity of a neuron and the number of spikes fired by that
1892 neuron in any bin can be modelled as a Bernoulli variable. But for wider time bins, only the
1893 activity can be modelled in this way.

1894 **4.3.3 Moving windows for measurements**

1895 When taking measurements (e.g. moving average over the number of active neurons) or
1896 fitting distributions (eg. the beta binomial distribution) we slid a window containing a certain
1897 number of bins across the data, and made our measurements at each window position. For
1898 example, when analysing 1ms bin data, we used a window containing 100 bins, and we slid

Bin width (ms)	Window size (bins)	Window size (ms)	Windows per trial
1ms	100	100ms	296
5ms	40	200ms	286
10ms	40	400ms	266

TABLE 4.1: Details of the different bin width and analysis window sizes used when binning spike times, and analysing those data.

1899 the window across the time interval for each trial moving 10 bins at a time. So that for
 1900 3060ms of data, we made 296 measurements.

1901 For the 5ms bin width data, we used windows containing 40 bins, and slid the window 2
 1902 bins at a time when taking measurements.

1903 For the 10ms bin width data, we used windows containing 40 bins, and slid the window
 1904 1 bin at a time when taking measurements (see table 4.1 for concise details).

1905 By continuing to use windows containing 40 bins, we retained statistical power but sac-
 1906 rificed the number of measurements taken.

1907 There was an interval between each trial with a grey image in place of the moving of
 1908 the moving bar stimulus. This interval varied in time. But we included some of this interval
 1909 when recording the data for each trial. We started recording the number of active neurons,
 1910 and the number of spikes from each neuron from 530ms before each trial until 1030ms after
 1911 each trial. This way, we could see the change in our measurements at the onset of a stimulus
 1912 and the end of stimulus presentation.

1913 As mentioned in section 4.3.2, we recorded the number of active neurons in each bin, and
 1914 the spike count for each neuron in each bin. The actual measurements we took using these
 1915 data in each window were as follows:

1916 **Moving average** The average number of active cells in each window.

1917 **Moving variance** The variance of the number of active cells in each window.

1918 **Average correlation** We measured the correlation between the spike counts of each pair of
 1919 cells in the ensemble, and took the average of these measurements.

1920 **Binomial p** We fitted a binomial distribution to the data in each window and recorded the
 1921 fitted probability of success, p in each case.

1922 **Beta-binomial α, β** We fitted a beta-binomial distribution to the data in each window, and
 1923 recorded the values of the fitted shape parameters, α and β , of each distribution.

1924 **Conway-Maxwell-binomial distribution p, ν** We fitted a Conway-Maxwell-binomial dis-
 1925 tribution to the data in each window, and recorded the fitted values of p and ν for each
 1926 distribution.

1927 **Log-likelihoods** We also recorded the log-likelihood of each of the fitted distributions for
 1928 each window.

1929 **4.3.4 Fano factor**

The *Fano factor* of a random variable is defined as the ratio of the variable's variance to its mean.

$$F = \frac{\sigma^2}{\mu} \quad (4.1)$$

1930 We measured the Fano factor of the spike count of a given cell by measuring the mean and
 1931 variance of the spike count across trials, and taking the ratio of those two quantities. When
 1932 calculated in this way the Fano factor can be used as a measure of neural variability that
 1933 controls for changes in the firing rate. This is similar to the calculation used in (Churchland
 1934 et al., 2010).

1935 **4.3.5 Probability Distributions suitable for modelling ensemble activity**

1936 We present here three different probability distributions that could be suitable to model the
 1937 number of active neurons in an ensemble. Each distribution has the set $\{0, \dots, n\}$ as its sup-
 1938 port, where n is the number of neurons in the ensemble. These are simple distributions with
 1939 either two or three parameters each. However, we regard n as known when using these dis-
 1940 tributions for modelling, so in effect each distribution has either one or two free parameters.

1941 **Association**

1942 *Association* between random variables is similar to the correlation between random variables
 1943 but is more general in concept. The correlation is a measure of association; and association
 1944 doesn't have a mathematical definition like correlation does. Essentially, the association
 1945 between two random variables is their tendency to take the same or similar values. Positively
 1946 associated variables tend to take the same value, and negatively associated variables tend to
 1947 take different values. In this research, we work with probability distributions of the number of
 1948 successes in a set of Bernoulli trials. These Bernoulli variables may or may not be associated.

1949 A probability distribution over the number of successes in n Bernoulli trials, where the
 1950 Bernoulli variables may be associated, could constitute a good model for the number of active
 1951 neurons in an ensemble of n neurons.

1952 **Binomial distribution**

The binomial distribution is a two parameter discrete probability distribution that can be thought of as a probability distribution the number of successes from n independent Bernoulli trials, each with the same probability of success. The parameters of the binomial distribution are n the number of trials, and $0 \leq p \leq 1$, the probability of success for each of these trials. A random variable with the binomial distribution can take values from $\{0, \dots, n\}$. The probability mass function of the distribution is

$$P(k; n, p) = \binom{n}{k} p^k (1-p)^{n-k} \quad (4.2)$$

1953 As a model for the activity of a neuronal ensemble, the main problem with the binomial
 1954 distribution is that it treats each neuron, represented as a Bernoulli trial, as independent. It is
 1955 well known that neurons are not independent, and that correlated behaviour between neurons
 1956 is vital for representing sensory information (Cohen and Maunsell, 2009). The binomial dis-
 1957 tribution falls short in this regard, but it is useful as performance benchmark when assessing
 1958 the performance of other models.

1959 **Beta-binomial distribution**

1960 The beta distribution is the conjugate distribution of the binomial distribution. The beta-
 1961 binomial distribution is the combination of the beta distribution and the binomial distribution,
 1962 in that the probability of success for the binomial distribution is sampled from the beta dis-
 1963 tribution. This allows the beta-binomial distribution to capture some over dispersion relative
 1964 to the binomial distribution.

The beta-binomial distribution is a three parameter distribution, n the number of Bernoulli trials, and $\alpha \in \mathbb{R}_{>0}$ and $\beta \in \mathbb{R}_{>0}$ the shape parameters of the beta distribution. The probability mass function for the beta-binomial distribution is

$$P(k; n, \alpha, \beta) = \binom{n}{k} \frac{B(k + \alpha, n - k + \beta)}{B(\alpha, \beta)} \quad (4.3)$$

1965 where $B(\alpha, \beta)$ is the beta function.

This probability distribution can be reparametrised in a number of ways. One of which defines new parameters π and ρ by

$$\pi = \frac{\alpha}{\alpha + \beta} \quad (4.4)$$

$$\rho = \frac{1}{\alpha + \beta + 1} \quad (4.5)$$

1966 This reparametrisation is useful because π acts as a location parameter analogous to the p
 1967 parameter of a binomial distribution. A value of $\rho > 0$ indicates over-dispersion relative to a
 1968 binomial distribution.

1969 As a model for the activity of a neuronal ensemble, the beta-binomial distribution is
 1970 more suitable than a binomial distribution because the over-dispersion of the beta-binomial
 1971 distribution can be used to model positive association between the neurons. An extreme
 1972 example of this over-dispersion/positive association can be seen in figure 4.1b. In this figure,
 1973 the neurons are positively associated and so tend to take the same value, consequently the
 1974 probability mass of the beta-binomial distribution builds up close to $k = 0$ and $k = n$. It is
 1975 worth noting that the location parameter for each distribution has the same value, $p = \pi =$
 1976 0.5.

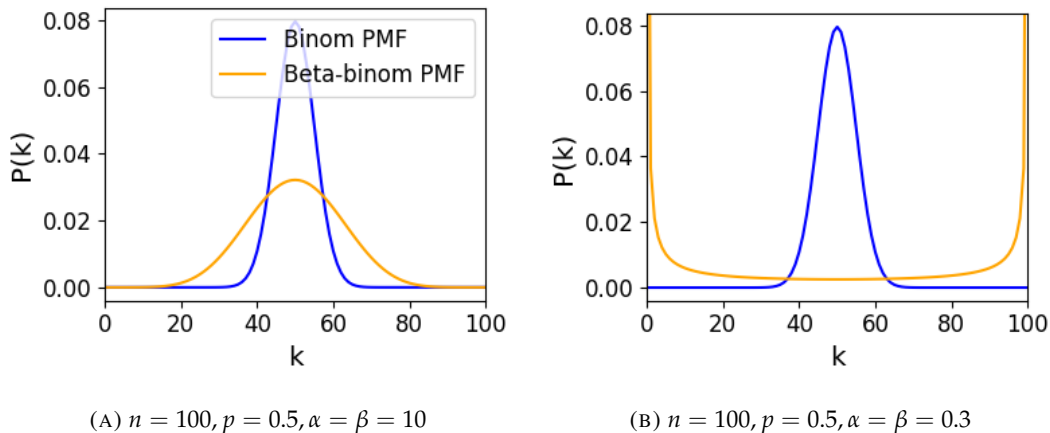


FIGURE 4.1: Figures showing the over-dispersion possible for a beta-binomial distribution relative to a binomial distribution. Parameters are shown in the captions.

1977 Conway-Maxwell-binomial distribution

1978 The Conway-Maxwell-binomial distribution (COMb distribution) is a three parameter generalisation of the binomial distribution that allows for over dispersion and under dispersion

relative to the binomial distribution. The parameters of the distribution are n the number of Bernoulli trials, and two shape parameters $0 \leq p \leq 1$, and $\nu \in \mathbb{R}$.

The probability mass function of the COMb distribution is

$$P(k; n, p, \nu) = \frac{1}{S(n, p, \nu)} \binom{n}{k}^{\nu} p^k (1-p)^{n-k} \quad (4.6)$$

where

$$S(n, p, \nu) = \sum_{j=0}^n \binom{n}{j}^{\nu} p^j (1-p)^{n-j} \quad (4.7)$$

The only difference between this PMF and the PMF for the standard binomial is the introduction of ν and the consequent introduction of the normalising function $S(n, p, \nu)$.

Indeed, if $\nu = 1$ the COMb distribution is identical to the binomial distribution with the same values for n and p . We can see in figure 4.2d that the KL-divergence $D_{KL}(P_{COMb}(n, p, \nu) || P_{Bin}(n, p)) = 0$ along the line where $\nu = 1$. The analytical expression for the divergence is

$$D_{KL}(P_{COMb}(k; n, p, \nu) || P_{Bin}(k; n, p)) = (\nu - 1) E_{P_{COMb}(k; n, p, \nu)} \left[\log \binom{n}{k} \right] \quad (4.8)$$

$$- \log S(n, p, \nu) \quad (4.9)$$

At $\nu = 1$, we have $S(n, p, 1)$ which is just the sum over the binomial PMF, so $S(n, p, 1) = 1$ and therefore $D_{KL}(P_{COMb}(n, p, \nu) || P_{Bin}(n, p)) = 0$.

If $\nu < 1$ the COMb distribution will exhibit over-dispersion relative to the binomial distribution. If $p = 0.5$ and $\nu = 0$ the COMb distribution is the discrete uniform distribution, and if $\nu < 0$ the mass of the COMb distribution will tend to build up near $k = 0$ and $k = n$. This over-dispersion represents positive association in the Bernoulli variables. An example of this over-dispersion can be seen in figure 4.2b.

If $\nu > 1$ the COMb distribution will exhibit under-dispersion relative to the binomial distribution. The larger the value of ν the more probability mass will build up at $n/2$ for even n , or at $\lfloor n/2 \rfloor$ and $\lceil n/2 \rceil$ for odd n . This under-dispersion represents negative association in the Bernoulli variables. An example of this under-dispersion can be seen in figure 4.2a.

It should be noted that the p parameter of the COMb distribution does not correspond to the mean of the distribution, as is the case for the binomial p parameter, and beta-binomial π parameter. That is, the COMb p parameter is not a location parameter. An illustration of this can be seen in figure 4.2c. This is because an interaction between the p and ν parameters skews the mean. There is no analytical expression for the mean of the COMb distribution.

ν	Relative dispersion	Association between neurons/variables
< 1	over	positive
1	none	none
> 1	under	negative

TABLE 4.2: Relative dispersion of the COMb distribution, and association between Bernoulli variables as represented by the value of the ν parameter.

2000 Since the COMb distribution has the potential to capture positive and negative associa-
 2001 tions between the neurons/Bernoulli variables, it should be an excellent candidate for mod-
 2002 elling the number of active neurons in a neuronal ensemble.

2003 We wrote a dedicated Python package to enable easy creation and fitting of COMb dis-
 2004 tribution objects. The format of the package imitates the format of other distribution objects
 2005 from the `scipy.stats` Python package. The COMb package can be found here:
 2006 https://github.com/thomasjdelaney/Conway_Maxwell_Binomial_Distribution

2007 4.3.6 Fitting

2008 We fitted binomial, beta-binomial, and Conway-Maxwell-binomial (COMb) distributions to
 2009 the neural activity in each of the overlapping windows covering each trial. To fit the distribu-
 2010 tions we minimised the appropriate negative log likelihood function using the data from the
 2011 window.

There is an analytical solution for maximum likelihood estimate of the binomial distribution's p parameter.

$$\hat{p} = \frac{1}{n} \sum_{i=1}^N k_i \quad (4.10)$$

2012 We minimised the negative log likelihood function of the beta-binomial distribution nu-
 2013 merically. We calculated the negative log likelihood for a sample directly, by taking the sum
 2014 of the log of the probability mass function for each value in the sample. We minimised the
 2015 negation of that function using the `minimise` function of the `scipy.optimize` Python
 2016 package.

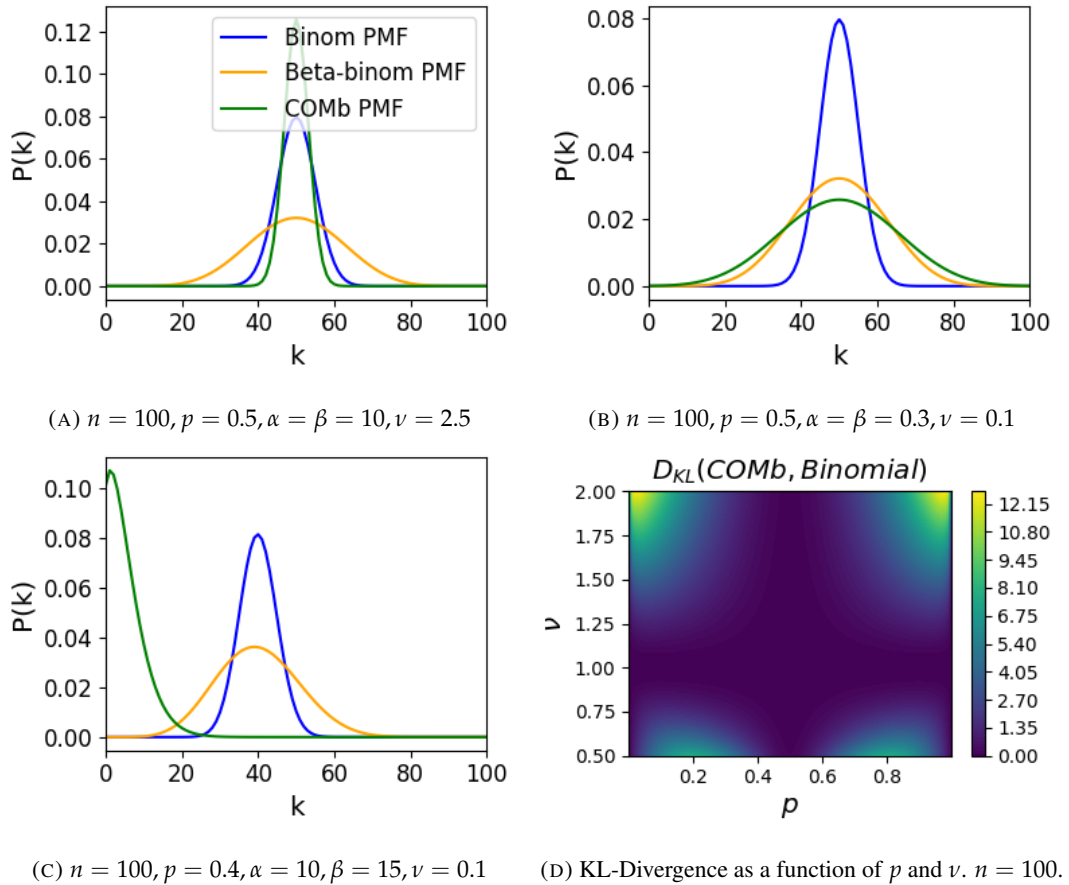


FIGURE 4.2: Figures showing (A) the under-dispersion and (B) over-dispersion permitted by the COMb distribution relative to a binomial distribution. (C) illustrates that the p parameter of the COMb distribution does not correspond to the mean of the distribution, as it does for the binomial and beta-binomial distributions. (D) shows a heatmap for the value of the Kullback-Liebler divergence between the COMb distribution and the standard binomial distribution with same value for n , as a function of p and ν . Parameters are shown in the captions.

The log likelihood function of the COMb distribution given some sample $\{k_1, \dots, k_N\}$ is

$$\ell(p, \nu | k_1, \dots, k_N) = N [n \log(1 - p) - \log S(n, p, \nu)] \quad (4.11)$$

$$+ \log \frac{p}{1 - p} \sum_{i=1}^N k_i \quad (4.12)$$

$$+ \nu \sum_{i=1}^N \log \binom{n}{k_i} \quad (4.13)$$

2017 We minimised the negation of this function using numerical methods. More specifically, we
2018 used the `minimise` function of the `scipy.optimize` Python package.

2019 **4.3.7 Goodness-of-fit**

2020 After fitting, we measured the goodness-of-fit of each model/distribution with their log like-
2021 lihood. We calculated this directly using the `logpmf` functions of the distribution objects in
2022 Python.

2023 **4.4 Results**

2024 We defined a neuron as *active* in a time bin if it fires at least one spike during the time interval
2025 covered by that bin. We measured the number of active neurons in the primary visual cortex
2026 of a mouse in 1ms bins across 160 trials of a moving bar visual stimulus. We then slid a
2027 100ms window across these 1ms bins taking measurements, and fitting distributions along
2028 the way. We did the same for neurons in the thalamus, hippocampus, striatum, and motor
2029 cortex. We repeated the analysis for 5ms time bins with 40 bin windows, and 10ms time bins
2030 with 40 bin windows.

2031 **4.4.1 Increases in mean number of active neurons and variance in number of
2032 active neurons at stimulus onset in some regions**

2033 We measured the average number of active neurons, and the variance of the number of active
2034 neurons in a 100ms sliding window starting 500ms before stimulus onset until 1000ms after
2035 stimulus onset. We found differences in the response across regions. There were no observed
2036 changes in response to the stimulus in the motor cortex or the striatum. The changes in the
2037 other regions are detailed below.

2038 **Primary visual cortex**

2039 We found a transient increase in both the average and variance of the number of active neu-
2040 rons at stimulus onset, followed by a fall to pre-stimulus levels, followed by another transient
2041 increase (see figure 4.3). The oscillation in both of these measurements appear to reflect the
2042 frequency of the stimulus (see Data section 4.2.1), and it is known that stimulus structure can
2043 influence response structure(Litwin-Kumar, Chacron, and Doiron, 2012). We see a similar
2044 but lower amplitude oscillation at the end of the stimulus presentation.

2045 **Hippocampus**

2046 In the hippocampus we observed a transient increase in the average number of active neurons
2047 and in the variance of the number of active neurons at stimulus onset (see figure 4.4). The
2048 increase lasted about 125ms, and the subsequent fall to baseline took the a similar amount of
2049 time.

2050 **Thalamus**

2051 In the thalamus we observed a transient increase in the both the average and variance of
2052 the number of active neurons on stimulus onset, followed by a fall to pre-stimulus levels,
2053 followed by a sustained increase until the stimulus presentation ends.

2054 As one you might expect for a visual stimulus, the change in the average number of active
2055 neurons was greatest in the primary visual cortex. In this region, this quantity doubled on
2056 stimulus onset. In contrast, in the hippocampus and the thalamus, the average number of
2057 active neurons only increased by a fraction of the unstimulated baseline value. The duration
2058 of the response in V1 and the hippocampus at stimulus onset was 300 – 400ms, but the
2059 response in the thalamus appeared to last for the duration of stimulus presentation. The V1
2060 also showed a change in the average number of active neurons at stimulus end. The change
2061 was similar to that observed at stimulus onset, but smaller in magnitude (see figures 4.3, 4.4,
2062 and 4.5)

2063 **4.4.2 Conway-Maxwell-binomial distribution is usually a better fit than bino-
2064 mial or beta-binomial**

2065 Since the Conway-Maxwell-binomial distribution has not been fitted to neuronal data before,
2066 it is not clear that it would be a better fit than the binomial or beta-binomial distributions.
2067 In order to find out which parametric distribution was the best fit for the largest proportion

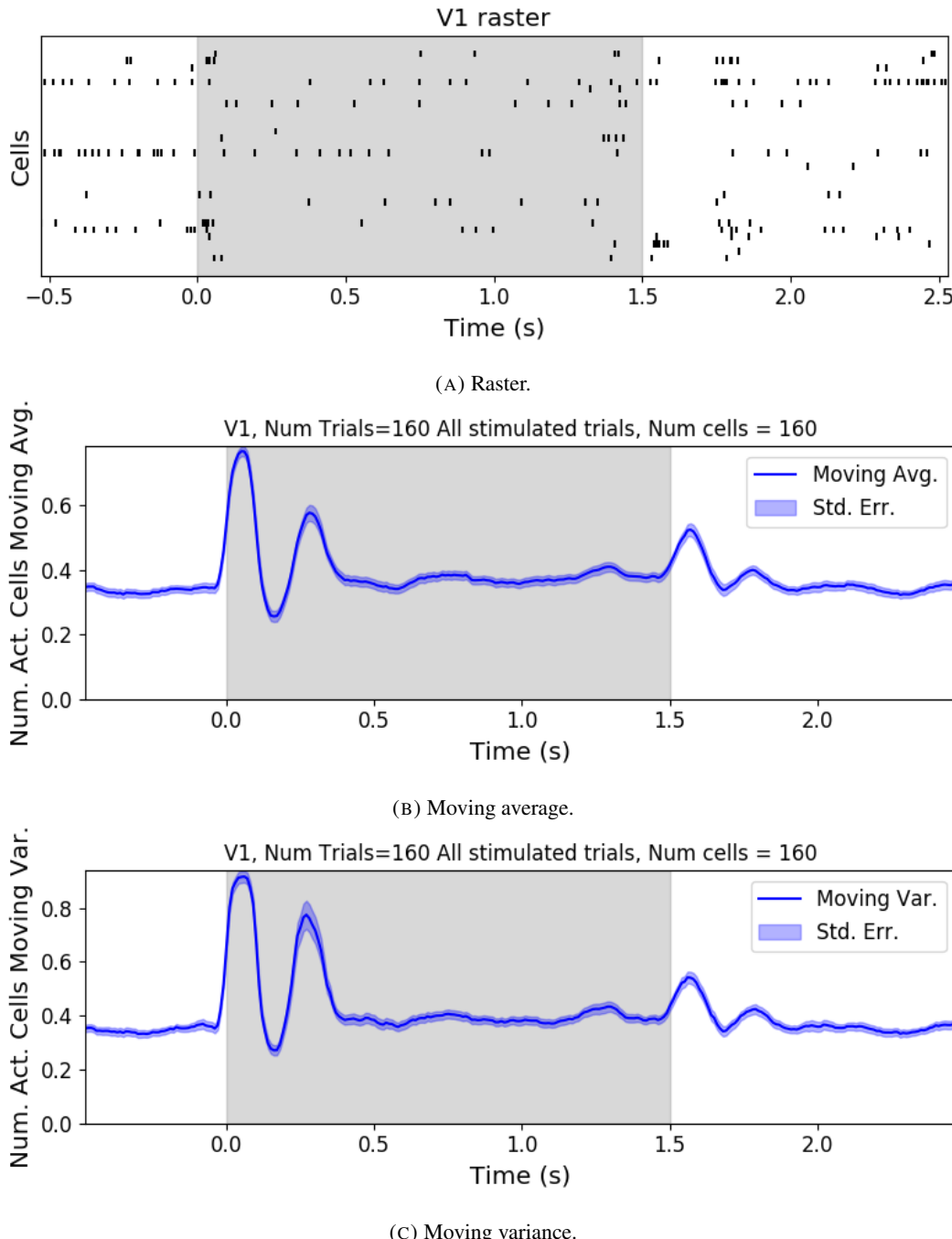


FIGURE 4.3: (A) Raster plot showing the spikes fired by 33 randomly chosen neurons in the primary visual cortex. (B-C) (B) average and (C) variance of the number of active neurons, measured using a sliding window 100ms wide, split into 100 bins. The midpoint of the time interval for each window is used as the timepoint (x-axis point) for the measurements using that window. The grey shaded area indicates the presence of a visual stimulus. The opaque line is an average across the 160 trials that included a visual stimulus of any kind. We can see a transient increase in the average number of active neurons and the variance of this number, followed by a fluctuation and another increase.

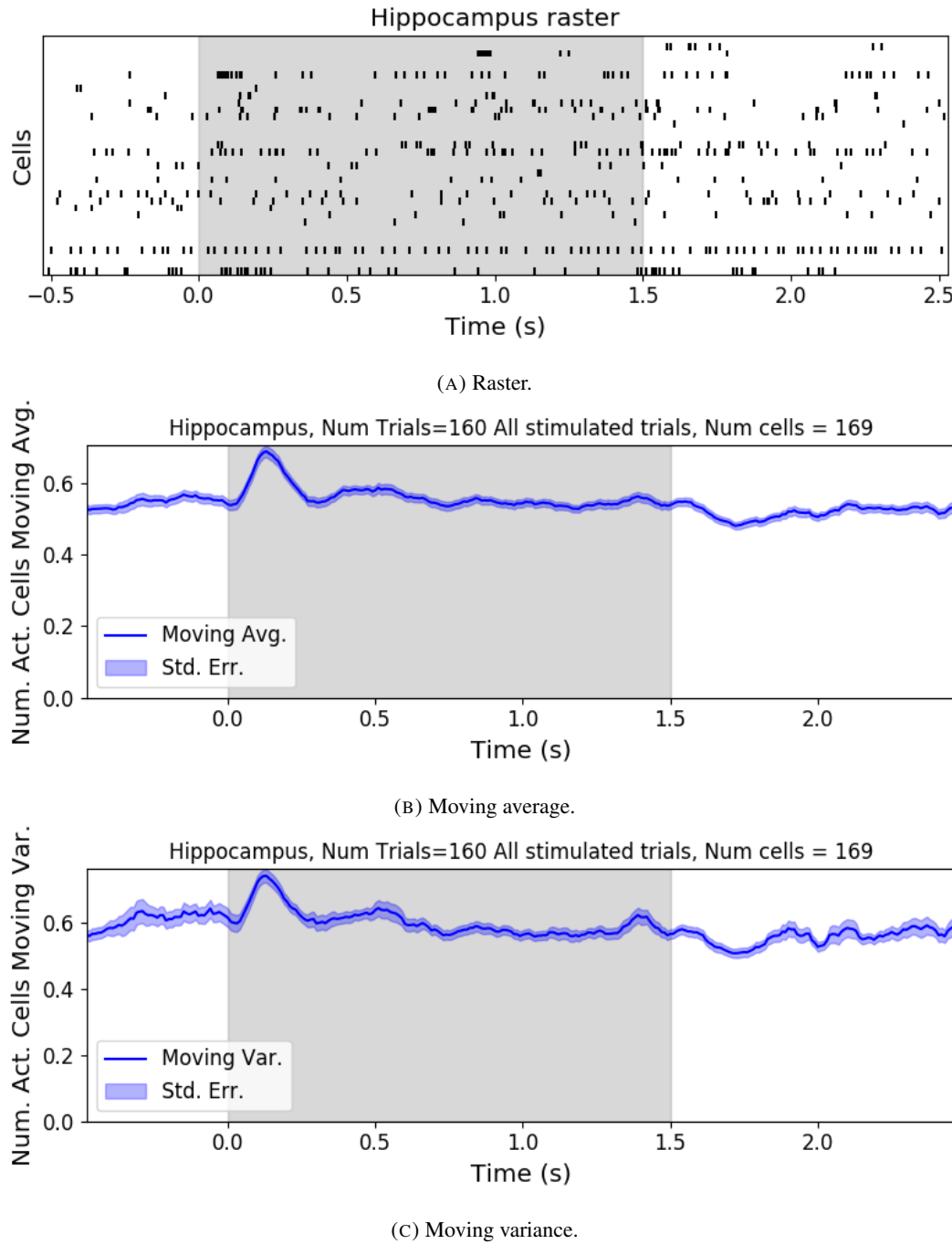


FIGURE 4.4: (A) Raster plot showing the spikes fired by 33 randomly chosen neurons in the hippocampus. (B-C) (B) average and (C) variance of the number of active neurons, measured using a sliding window 100ms wide, split into 100 bins. The midpoint of the time interval for each window is used as the timepoint (x-axis point) for the measurements using that window. The grey shaded area indicates the presence of a visual stimulus. The opaque line is an average across the 160 trials that included a visual stimulus of any kind. We can see a transient increase in the average number of active neurons and the variance of this number at stimulus onset.

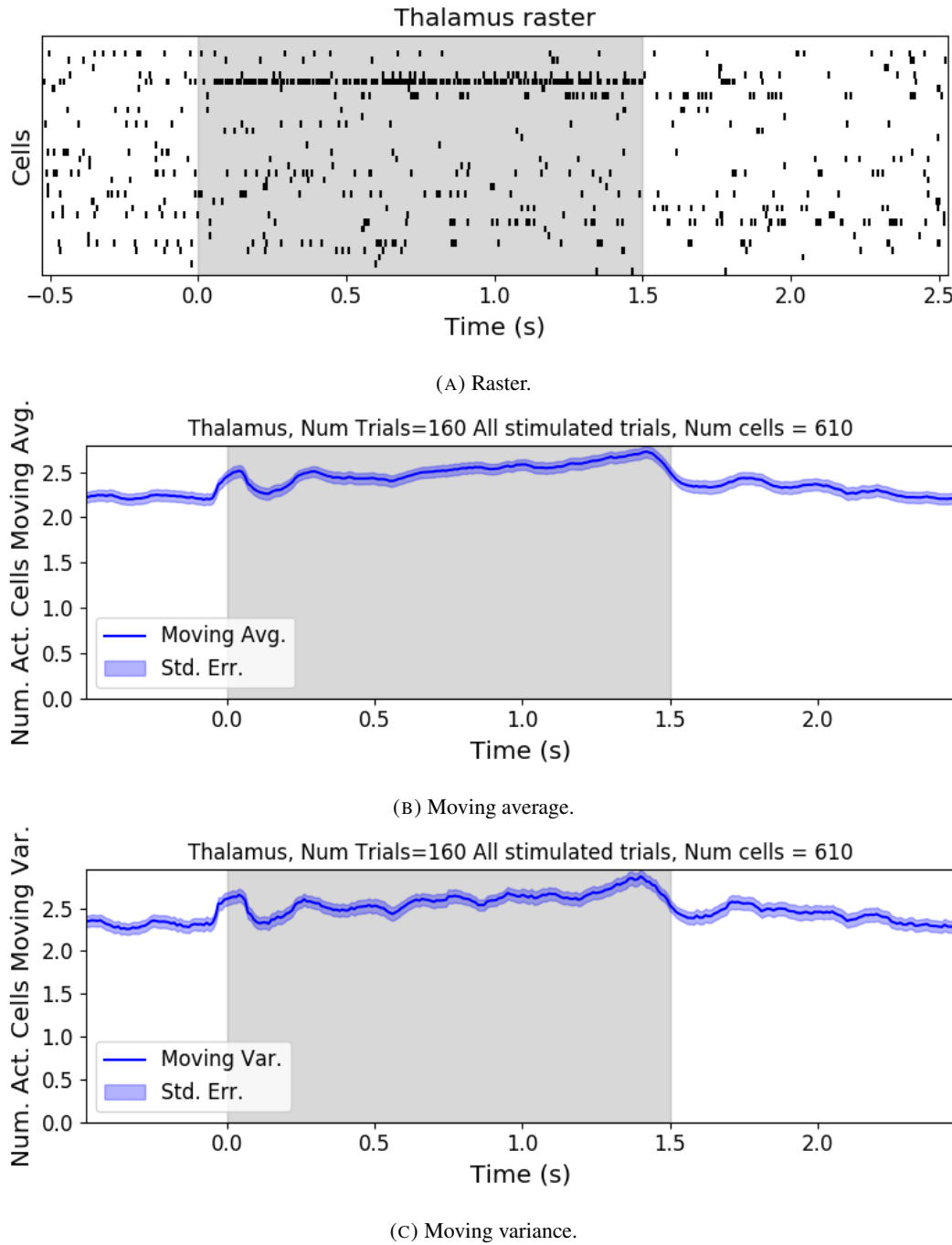
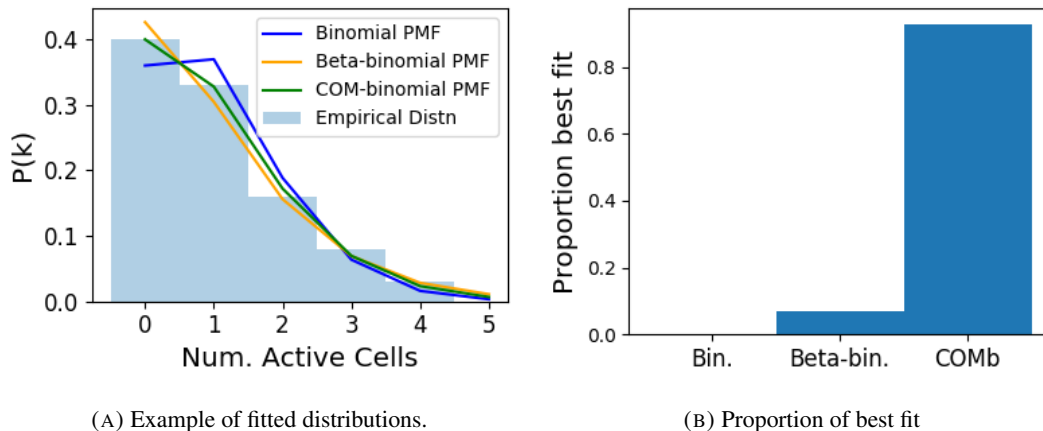


FIGURE 4.5: (A) Raster plot showing the spikes fired by 33 randomly chosen neurons in the thalamus. (B-C) (B) average and (C) variance of the number of active neurons, measured using a sliding window 100ms wide, split into 100 bins. The midpoint of the time interval for each window is used as the timepoint (x-axis point) for the measurements using that window. The grey shaded area indicates the presence of a visual stimulus. The opaque line is an average across the 160 trials that included a visual stimulus of any kind. We can see an immediate increase at stimulus onset, a subsequent fall, and another sustained increase until the stimulus presentation ends.

of our data, we fit a binomial, a beta-binomial, and a Conway-Maxwell-binomial (COMb) distribution to each window for each bin width, and each region. Then we assessed the goodness-of-fit of each distribution by calculating the log-likelihood of each fitted distribution using the associated sample. We measured the proportion of samples for which each distribution was the best fit, for each bin width value and each region.

We found that the COMb distribution was the best fit for most of the samples regardless of bin width or region. The bin width had an effect on the number of samples for which the COMb distribution was the best fit. The results are summarised in table 4.3. For a bin width of 1ms, the COMb distribution was the best fit for over 90% of samples, the beta-binomial distribution was the best fit for less than 10% of samples, and the binomial distribution was the best fit for less than 1% of samples, across regions. For 5ms bins, the COMb distribution was the best fit for 70 – 80% of samples, the beta-binomial distribution was the best fit for 20 – 30% of the samples, and again the binomial distribution was the best fit for less than 1% of samples, across regions. Finally, for 10ms bins, the COMb distribution was the best fit for 53 – 80% of samples, the beta-binomial distribution was the best fit for 20 – 47% of the samples, and the binomial distribution was the best fit for less than 0.1% of samples, across regions.



(A) Example of fitted distributions. (B) Proportion of best fit

FIGURE 4.6: (A) An example of the binomial, beta-binomial, and Conway-Maxwell-binomial distributions fitted to a sample of neural activity. The Conway-Maxwell-binomial distribution is the best fit in this case. The histogram shows the empirical distribution of the sample. The probability mass function of each distribution is indicated by a different coloured line. (B) Across all samples in all trials, the proportion of samples for which each fitted distribution was the best fit. The Conway-Maxwell-binomial distribution was the best fit for 93% of the samples taken from V1 using a bin width of 1ms.

Bin Width (ms)	Binomial	Beta-binomial	COMb
1ms	< 1%	< 10%	> 90%
5ms	< 0.1%	20 – 30%	70 – 80%
10ms	< 0.1%	20 – 47%	53 – 80%

TABLE 4.3: Proportion of samples for which each distribution was the best fit, grouped by bin width. The COMb distribution is the best fit most of the time.

2085 **4.4.3 Conway-Maxwell-binomial distribution captures changes in association
2086 at stimulus onset**

2087 We fit a Conway-Maxwell-binomial (COMb) distribution to the number of active neurons in
2088 the 1ms time bins in a 100ms sliding window. We also measured the correlation coefficient
2089 between the spike counts of all possible pairs of neurons, and took the average of these
2090 coefficients. We did this for all the trials with a visual stimulus. We observed a reduction in
2091 the COMb distribution's ν parameter at stimulus onset from around 1 to between 0 and 1 (see
2092 figure 4.7a). A value of ν less than 1 indicates positive association between the neurons (see
2093 section 4.3.5). We might expect to see this positive association reflected in the correlation
2094 coefficients, but this is not the case. We see no change in the time series of average correlation
2095 measures at stimulus onset.

2096 This may be due to the very short time bin we used in this case. We know that using small
2097 time bins can artificially reduce correlation measurements (Cohen and Kohn, 2011). In this
2098 case, fitting the COMb distribution may be a useful way to measure association in a neuronal
2099 ensemble over very short timescales (< 10ms).

2100 **4.4.4 Replicating stimulus related quenching of neural variability**

2101 Churchland et al. (2010) inspected the effect of a stimulus on neural variability. One of the
2102 measures of neural variability that they employed was the Fano factor of the spike counts of
2103 individual cells (see section 4.3.4). They found a reduction in neural variability as measured
2104 by the Fano factor in various cortical areas in a macaque at the onset of various visual stimuli,
2105 or a juice reward (Churchland et al., 2010).

2106 We measured the Fano factor of the spike count of each cell in each brain region, during
2107 each trial. We measured the mean and standard error of these Fano factors from 500ms
2108 before stimulus onset until 1000ms after stimulus end. For the primary visual cortex, we
2109 found a transient reduction in the Fano factor immediately after stimulus onset. We used
2110 a Mann-Whitney U test to check that the Fano factors measured in a window starting at

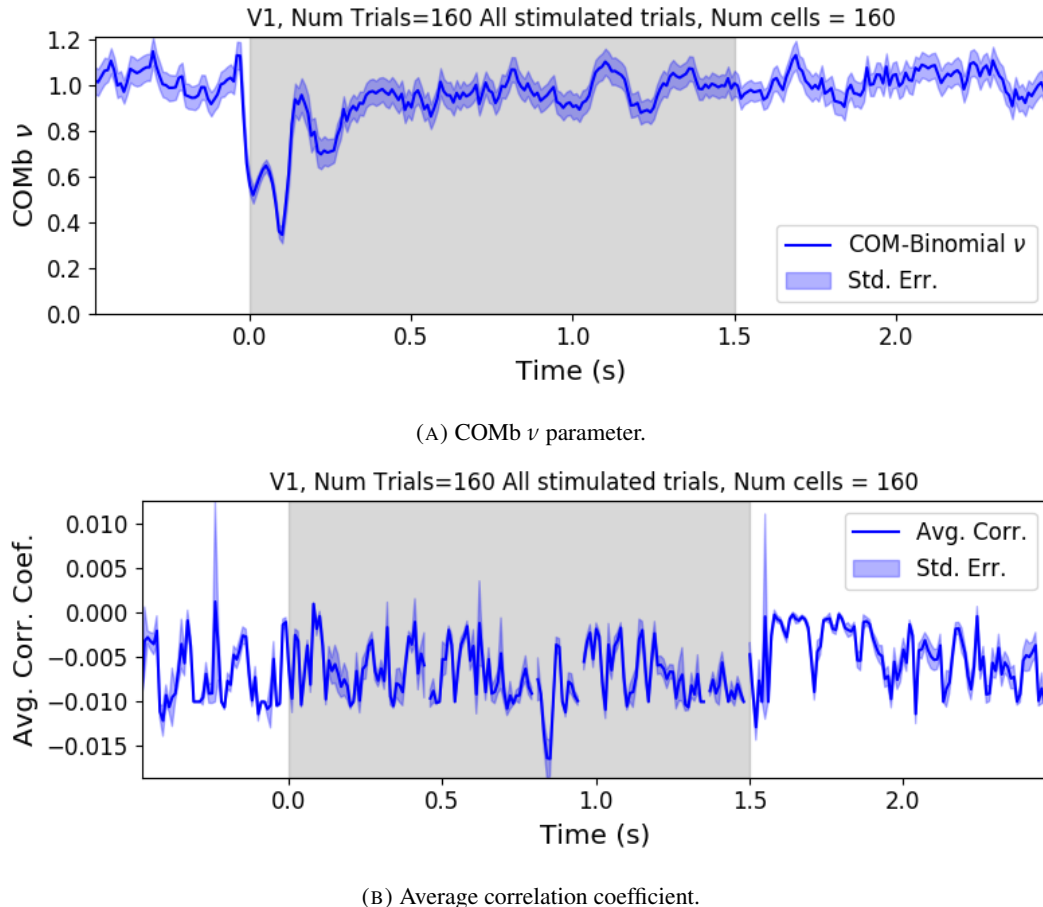


FIGURE 4.7: (A) We fit a Conway-Maxwell-binomial distribution to the number of active neurons in 1ms time bins of a 100ms sliding window. We did this for all trials with a visual stimulus and took the average across those trials. We see a transient drop in value for the distribution's ν parameter at stimulus onset. This shows an increase in association between the neurons. (B) We measured the correlation coefficient between the spike counts of all possible pairs of neurons in the same sliding window. We took the average of those coefficients. We also did this for every visually stimulated trial, and took the average across trials. The increase in association is not reflected with an increase in average correlation.

stimulus onset and ending 100ms later were significantly lower than the factors measured in a window ending at stimulus onset ($p < 0.001$, see figure 4.8a). We did not get this statistically significant result in any other region.

Our findings agree with those of Churchland et al. for the primary visual cortex. However Churchland also found a reduction in the Fano factor in the dorsal premotor cortex (PMd) at stimulus onset. Our measurements from the mouse motor cortex show no change at stimulus onset (see figure 4.8b). This could indicate some difference in the functionality of the motor cortex in a macaque and the motor cortex of a mouse.

Similar to these findings in the Fano factor, we found a reduction in the ν parameter of the COMB distribution on stimulus onset in V1 (figure 4.7a) and in no other region from

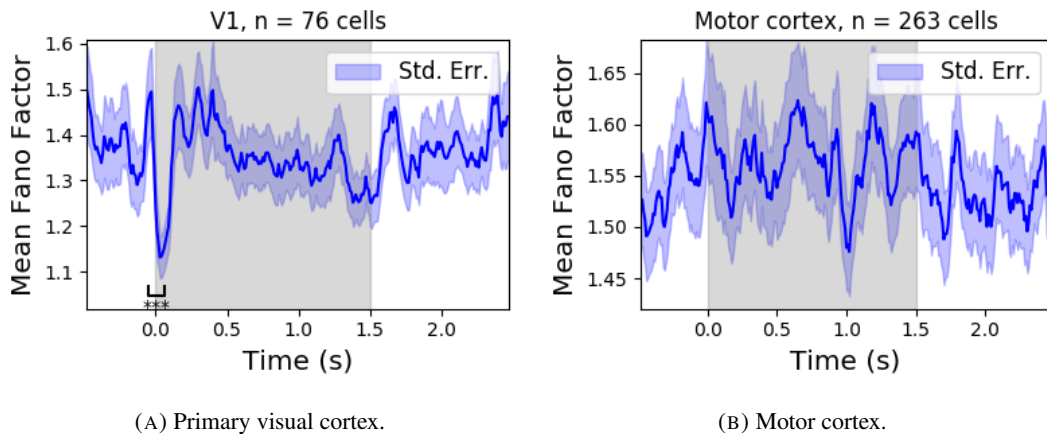


FIGURE 4.8: (A) The mean Fano factor of the spike counts of the cells in the primary visual cortex. Means were taken across cells first, then across trials. There was a significant decrease in the Fano factors immediately after stimulus onset. (B) The mean Fano factor of the spike counts of the cells in the motor cortex. No significant change in measurements at any point.

which we had data. Specifically, the ν parameter reduced from around 1, to between 1 and 0. This represents a change from no association between the neurons, to a positive association. It is possible that this positive association may be responsible for the reduction in the Fano factor.

4.5 Discussion

Our aim in this research was to develop a new statistical method for analysing the activity of a neuronal ensemble at very short timescales. We wanted our method to use information taken from the whole ensemble, but we also wanted the method to be quick and easy to implement. It is likely that analysis methods with these characteristics will become valuable as electrophysiological datasets include readings from more cells over longer time periods. In this case, we used the number of active, or spiking, neurons in a very short time bin ($< 10\text{ms}$) as a measure of ensemble activity.

First of all, we showed that there were changes in response that we could model at these very short time scales in some of the brain regions from which we had recordings. We observed changes in the average number of active neurons, and the variance of the number of active neurons in three different brain regions in response to visual stimuli. Since we know that correlated behaviour is associated with sensory perception (deCharms and Merzenich, 1996), we might hope to measure the pairwise correlations within the neuronal population in order to further investigate these responses. But, using such short time bins can produce

artificially small spike count correlation measurements (Cohen and Maunsell, 2009). Overcoming this limitation was one of our objectives for our new method. In order to do this, we abandoned the idea of measuring the correlations directly and embraced the concept of *association*. In order to quantify the association between neurons, we used the Conway-Maxwell-binomial distribution to model the number of active (spiking) neurons in an ensemble as a sum of possibly associated Bernoulli random variables.

We showed that the Conway-Maxwell-binomial distribution performed better than the more common options of the binomial and beta-binomial distributions. Furthermore, we showed that the positively associated behaviour between neurons in the primary visual cortex could be captured by fitting a Conway-Maxwell-binomial distribution, but was not captured by the more standard approach of measuring the spike count correlation. The associated behaviour could not be measured using spike count correlations, because of the very short bins required to capture short timescale behaviour.

We replicated a famous result from Churchland et al (2010) relating to the quenching of neural variability in cortical areas at stimulus onset, and in doing so, we established a correspondence between the association quantifying parameter of the Conway-Maxwell-binomial (COMb) distribution and the neural variability as measured by the Fano factor. We found a reduction in the ν parameter of the COMB distribution at stimulus onset, indicating a change from no association to positive association between neurons in V1. We found a corresponding reduction in the Fano factor of the individual cells in V1. The positive association between neurons induced by the stimulus would constrain the neurons to fire at the same time. The stimulus also induced a larger number of neurons to spike. These two actions combined could cause an increase in the firing rate of individual cells that is greater in magnitude than the increase in firing rate variability. If this is indeed the case, then the association as captured by the COMB distribution could be regarded as one of the ‘natural parameters’ of the ensemble response for short timescales. That is, a quantity that directly measures some aspect of the behaviour of the ensemble. In this case, it the correlated behaviour of the individual neurons is captured.

This work could be just a first step in creating analysis methods based on the Conway-Maxwell-binomial distribution, or similar statistical models. One way to extend the method would be to pair it up with the ‘Population Tracking model’ (O’Donnell et al., 2017). This model attempts to characterise the interaction between an ensemble and each member of the ensemble by quantifying the probability of spiking for a given a cell, given the number of active cells in the whole population. Combining this model with the COMB distribution

2174 would give us a model that could accurately fit the number of active neurons at any moment,
2175 and that gives a probability of firing for each cell, and therefore probabilities for full spiking
2176 patterns, without adding a huge number of parameters to fit.

2177 A more complex way to extend the model would be to fit a Conway-Maxwell-binomial
2178 distribution to data recorded from multiple brain regions simultaneously, with a different fit
2179 for each region, then to analyse the temporal relationship between the fitted parameters of
2180 each region. If we analysed the time series of the COMB distribution parameters from the
2181 different regions, looking at cross-correlations between regions, this may give some results
2182 relating to the timescales in which information is processed in different brain regions.

2183 **Chapter 5**

2184 **Studies with practical limitations &**
2185 **negative results**

2186 *Abstract*

2187 Here I will present some details on research topics that I started, but that unfortunately did not
2188 lead anywhere useful. There are two pieces of research, based on two papers. Each paper is
2189 related to the overall theme of my PhD of analysing and modelling behaviours of populations
2190 of neurons. The first part is based on a model of parallel spike trains including higher order
2191 interactions by Shimazaki et al (2012). The second part is based on a multiscale model for
2192 making inferences on hierarchical data.

2193 **5.1 Dynamic state space model of pairwise and higher order neu-**
2194 **ronal correlations**

2195 In their paper Shimazaki et al (2012) aimed to model spike trains from populations of neurons
2196 in parallel, with pairwise and higher order dynamic interactions between the trains. They
2197 modelled the spike trains as multi-variate binary processes using a log-linear model, and they
2198 extracted spike interaction parameters using a Bayesian filter/EM-algorithm. They developed
2199 a goodness-of-fit measure for the model to test if including these higher order correlations
2200 is necessary for an accurate model. Their measure was based on the Bayes factor but they
2201 also assessed the suitability of higher order models using the AIC and BIC. So the increase
2202 in the number of parameters associated with fitting higher order interactions was taken into
2203 account. They tested the performance of the model on synthetic data with known higher
2204 order correlations. They used the model to look for higher order correlations in data from
2205 awake behaving animals. They use the model to demonstrate dynamic appearance of higher
2206 order correlations in the monkey motor cortex (Shimazaki et al., 2012).

2207 We used the available Python repository to implement the model, and we successfully
2208 worked through the tutorial provided. But we found that the model did not scale well to
2209 larger populations. We attempted to fit the model to a population of 10 neurons and found we
2210 didn't manage to finish the process. Since, our goal was to find a model to scale to hundreds
2211 or thousands of neurons, we decided that this model was no longer worth pursuing.

2212 **5.2 A multiscale model for hierarchical data applied to**
2213 **neuronal data**

2214 In their paper Kolaczyk et al (2001) developed a framework for a modelling hierarchically
2215 aggregated data, and making inferences based on a model arising from this framework. They
2216 assumed that a hierarchical aggregation existed on the data in question, where each element at
2217 each level of the hierarchy had some associated measurements, an associated mean process,
2218 which was the expected value of these measurements. They also assumed that the measure-
2219 ments of each parent were equal to the sum of the measurements from all of its children.
2220 They showed that these assumptions gave rise to a relationship between parent and child
2221 measurements across all levels of the hierarchy, where the product of the likelihood of the
2222 parameters of the lowest level of the hierarchy can be expressed as products of conditional
2223 likelihoods of the elements of higher levels of the hierarchy (Kolaczyk and Huang, 2010).

2224 They gave examples of these expressions for measurements sampled from Gaussian dis-
2225 tributions, and Poisson distributions, and showed the definitions of the hierarchical param-
2226 eters which reparametrise the distribution of these data taking the hierarchy into account.
2227 They go on to suggest prior distributions for this multiscale model, and integrate these priors
2228 to give posterior distributions for the measurements from each element at each level in the hi-
2229 erarchy, and expressions for the MAP estimated parameters of each the associated processes
2230 (Kolaczyk and Huang, 2010).

2231 We implemented their model in Python by creating some synthetic data from Poisson
2232 distributions, and defining a hierarchy by agglomerating these data. We calculated the MAP
2233 estimates using our knowledge of the hierarchy, and using the expressions given in the paper.
2234 We found that the MAP estimates were far less accurate than would be achieved by simply
2235 ignoring the hierarchy during estimation, and using a maximum likelihood approach. After
2236 that, we decided to move on.

2237 **Chapter 6**

2238 **Discussion**

2239 In this project, we attempted to address some of the challenges in data collection from
2240 large neuronal ensembles (specifically with calcium imaging) and some of the problems in
2241 analysing the data collected from large neuronal ensembles.

2242 Firstly, we investigated the relationship between cell biochemistry, action potentials and
2243 the fluorescence traces produced by fluorescent calcium indicators. We did this by building
2244 a biophysical model that takes in a spike train and returns the fluorescence trace that that
2245 spike would induce. The model included mechanics for the binding of calcium to fluorescent
2246 and endogenous mobile and immobile buffers, and the consequent changes in concentration
2247 of free and bounded calcium. The model consisted of 17 parameters, 13 of which were
2248 set according to data from the literature, and 4 of which were free parameters. We trained
2249 the model using simultaneously collected spiking and calcium imaging data (Berens et al.,
2250 2018). We fitted the model by matching the $\Delta F/F_0$ in response to an action potential, and
2251 by matching the power spectrum of the actual fluorescence trace. This meant that our model
2252 would include the correct amount of noise as well as return the correct change in amplitude
2253 in response to an action potential.

2254 Since our model produced fluorescence traces, we could apply spike inference algorithms
2255 to the modelled fluorescence traces that our model produced after training, and compare the
2256 performance of the algorithms on the modelled traces to their performance on the real traces.
2257 We used three spike inference algorithms, two of which were based on modelling the cal-
2258 cium trace as an autoregression (Friedrich and Paninski, 2016; Pnevmatikakis et al., 2016),
2259 and another inference algorithm that was a little more biologically inspired, but amounted to
2260 a very similar algorithm (Deneux et al., 2016). We compared the performance of the algo-
2261 rithms by using them to infer spikes from 20 real and modelled fluorescence traces induced
2262 by 20 corresponding real spike trains. We then used several binary classification measures
2263 (true positive rate, accuracy etc.) to asses the quality of the spike inference for the real and

2264 modelled fluorescence traces. We found that the spike inference algorithms performed sim-
2265 ilarly on real and modelled traces, showing that our model is capturing at least some of the
2266 characteristics of the real fluorescence traces.

2267 In order to investigate the effect of indicator characteristics on the modelled fluorescence
2268 trace and spike inference quality, we perturbed the indicator's affinity and dissociation rate in
2269 parallel, keeping the ratio of the two the same for all perturbations. We measured the SNR
2270 of the trace, and the true positive rate of the spike inference algorithms at each perturbed
2271 value pair. We found that perturbing the values lower caused in decrease in SNR and spike
2272 inference quality. This shows that our model could be used to test theoretical fluorescent cal-
2273 cium indicators without having to actually manufacture them. Experimental neuroscientists
2274 could also use our model to judge which indicator characteristics are most influential in their
2275 experimental context.

2276 We then investigated the effect of perturbing buffer concentration, and indicator concen-
2277 tration, on the signal-to-noise ratio of the modelled fluorescence trace and spike inference
2278 quality. This was a worthwhile experiment because endogenous buffer concentrations vary
2279 from cell to cell (Bartol et al., 2015; Maravall et al., 2000; Neher and Augustine, 1992), as
2280 does indicator expression (Chen et al., 2013). We found that extreme perturbations away
2281 from the indicator concentration taken from the literature lowered the SNR of the trace, and
2282 the spike inference quality. We also found that increases in the concentration of endogenous
2283 buffer above the value taken from the literature caused a decrease in the SNR and spike infer-
2284 ence quality. This reiterates that the indicator and endogenous buffers compete to bind with
2285 free calcium molecules, and this has an effect on fluorescence and consequently on spike
2286 inference.

2287 We then created some synthetic spike trains with controlled mean firing rates sampled
2288 the rates from an Ornstein-Uhlenbeck process. We found that the higher the firing rate, the
2289 lower the accuracy of the spike inference algorithms. But the mean firing could perhaps be
2290 inferred from the amplitude of the fluorescence traces. The higher firing rate, the higher the
2291 amplitude. Calibrating the model to facilitate and accurate measurement would require some
2292 kind of ground truth, but relative comparisons could be made without any other knowledge
2293 of the underlying spiking process.

2294 One obvious limitation to our model is the lack of binding mechanics for both the indi-
2295 cator and endogenous buffers. Greenberg et al included these mechanics in their successful
2296 spike inference model. We felt that the timescale of these binding mechanics was so small
2297 in comparison to the fluorescence dynamics that omitting them would make no difference.

2298 But it is possible that their inclusion would improve our model.

2299 After investigating the difficulties with inferring spiking data from calcium imaging data,
2300 we moved from data collection to analysis and we decided to implement a new network anal-
2301 ysis method on data from a neuronal ensemble. Using an electrophysiological dataset with
2302 spike sorted data from 9 different brain regions in 3 mice (Steinmetz, Carandini, and Harris,
2303 2019), we binned the spike times for each cell into spike counts for each cell and measured
2304 the correlation coefficients between these spike counts for a selection of cells evenly dis-
2305 tributed across the 9 regions. We repeated these measurements for time bin widths ranging
2306 from 5ms to 3s. We rectified these measurements and, for a given time bin width, used them
2307 as weights for a weighted undirected graph where each node represents a neuron, and the
2308 weight of each edge is the correlation between the neurons represented by the nodes on that
2309 edge. We applied a novel spectral analysis and community detection method (Humphries
2310 et al., 2019) to this network. This clustered the nodes in our ensemble into communities
2311 whose behaviour was more correlated than expected. Our measure of 'expected correlation
2312 strength' were based on a random network that matched our data network's sparsity and total
2313 weight. We compared the detected communities to the anatomical division of our cells using
2314 clustering comparison measures. We then conditioned the binned spike counts on the be-
2315 haviour of the mouse using the principal components of a video of the mouses face recorded
2316 simultaneously with the electrophysiology. We broke the total covariance down into 'spike
2317 count covariance' and 'signal covariance' components conditioning on the behavioral data
2318 and using the law of total covariance. We then repeated our analysis for spike count corre-
2319 lations, and signal correlation. Finally, since our community detection method was only valid
2320 on graphs with non-negative weights, we used different methods for creating a non-negative
2321 graph from our total correlations, and we repeated our analysis on those graphs.

2322 Our first finding was that the time bin width used to bin spike times into spike counts had
2323 a effect on the mean magnitude of the correlations measured. The wider the bin, the higher
2324 the correlations. Not only that, we separated the pairs into positively and negative correlated
2325 pairs, and we found that positively correlated pairs have greater correlation coefficients when
2326 using a wider bin, and negatively correlated pairs have more negative correlation coefficients
2327 when using a wider bin. We also found that the width of the bin used had an effect on the
2328 distribution of the spike counts. For smaller bin widths, the distribution of spike counts was
2329 better represented by a skewed distribution like the Poisson distribution. For wider bins, the
2330 spike counts were better represented by a Gaussian distribution.

2331 Next we investigated the differences between correlations within regions and between

regions. When we divided the pairs according to those two groups, we found that the mean within-region correlations were higher at every bin width, and the difference between the two means grew with increasing bin width. When we split the pairs of cells according to their regions, we found that the mean within-region correlations in any given region were usually greater than the mean between-region correlations for any region pair involving that region. The difference between the mean within-region correlation and the highest between-region correlations involving that region grew smaller with increasing bin width. To investigate this further, we plotted these mean correlations in matrices. Although the mean within-region correlations were usually the highest value in their row or column, as the bin width increased, the mean between-region correlations grew in magnitude relative to the within-region figure.

Next we chose a null network model, and we used the ‘Network Noise Rejection’ process (Humphries et al., 2019) to check for additional structure in our correlation based data network that was not captured by the null model. We found additional structure for any bin width that we used. We also found that the dimensionality of the additional structure reduced as we increased the bin width. This could mean that the processes or representations that take place over longer timescales within the brain also take place in a lower dimensional space.

We applied a community detection method (Humphries, 2011) to the signal correlation networks arising from the network noise rejection. We found that the number of communities detected decreased with increasing bin width. We also noticed that at shorter bin widths, the detected communities were more likely to consist of cells from one brain region only. We investigated this further by using clustering comparison methods to compare the detected communities with the anatomical division of the cells. We found that for short timescales $< 50\text{ms}$ correlated communities tended to exist within anatomical regions, and for longer timescales $> 100\text{ms}$, the correlated communities tended to exist across anatomical regions. This is broadly in agreement with a similar finding for EEG data from humans performing semantic or memory tasks (Stein and Sarnthein, 2000). Von Stein et al. (2000) found that visual processing taking place locally in the visual system was captured in the gamma frequency range (25 – 70Hz), while semantic processing was captured in the beta range (12 – 18Hz), and tasks involving mental imagery and working memory retention were captured in the theta and alpha ranges (4 – 8Hz, and 8 – 12Hz respectively).

We then conditioned our correlation measures on the the mouse’s behaviour. This allowed us to create spike count correlation (or noise correlation) networks, and signal correlation networks (Cohen and Kohn, 2011). We applied our analysis to these networks. For the

spike count correlation networks we found very similar results to the total correlation networks. More communities at smaller bin widths, and communities resembled the anatomical division at smaller bin widths. Given that recent findings show that behaviour can account for correlated spiking in many areas of the brain (Stringer et al., 2019), these results for the spike count correlation show that this correlated behaviour is still processed locally at short timescales, while processes and representations that take more time make use of correlated activity across multiple regions.

For the signal correlations, we still found additional structure in these networks. But we always detected a smaller number of communities. These communities also had no relation to the anatomical division of the cells. This result shows that there are groups of cells across multiple brain regions that are activated similarly by certain behaviours.

All of the networks so far were based on rectified correlation measures, because the network noise rejection and community detection processing is (currently) only valid for networks with non-negative weights. For the final part of our analysis, we tried different ways of transforming our total correlations into non-negative quantities before applying our analysis. First of all we took the absolute value of our correlation measures. Our results were very similar to those for the rectified correlations with the exception that we detected more communities consistently. It is possible that using this method detects both positively and negatively correlated communities.

We also tried reversing the sign of all the correlations, then rectifying the network. We hope that this would allow us to detect the negatively correlated communities. We did detect communities in these networks, but never more than three, and these communities bore no relationship with the anatomical distribution of the cells.

Having spent much time investigating correlated behaviour using coefficients of spike counts, we decided to try another method for capturing correlated behaviour in neuronal ensembles. We used electrophysiological data taken from 5 brain regions of an awake mouse exposed to visual stimuli (Steinmetz et al., 2019). We modelled the number of active neurons in a given brain region as the number of successes in a collection of dependent Bernoulli random variables using the Conway-Maxwell-binomial distribution. To avoid violating the Bernoulli assumption, we binned the spike times using 1ms bins. The Conway-Maxwell-binomial distribution is a two parameter extension of the standard binomial distribution. The extra parameter allows the distribution to capture possible positive or negative association between the Bernoulli trials (Kadane, 2016). This means that we are assuming that all the neurons are dependent in the same way. This is not an accurate assumption, but it allows us

2399 model the data in a simple way.

2400 First of all we established that there were changes in the number of active neurons in
2401 response to the visual stimuli. This was the case in the hippocampus, thalamus, and primary
2402 visual cortex. Each region had its own signature response. We measured the mean and
2403 variance of the number of active neurons in a sliding window starting before stimulus onset,
2404 and finishing after the end of stimulus presentation.

2405 As well as the Conway-Maxwell-binomial distribution, we also fitted binomial, and beta-
2406 binomial distributions to the number of active neurons in a sliding window. We found that the
2407 Conway-Maxwell-binomial distribution was the best fit for over 90% of the samples. This
2408 means that the COMb distribution is capturing some dependency between the neurons, be-
2409 cause the binomial distribution assumes independence. Also the COMb distribution captures
2410 this dependence more accurately than the beta-binomial distribution, which does have some
2411 capacity for over dispersion.

2412 Next we showed that the Conway-Maxwell-binomial distribution captured the change
2413 in association at stimulus onset better than the correlation coefficient. The extremely small
2414 bin width artificially shrunk the correlation coefficient to the point where this measurement
2415 didn't detect any correlated activity. But the association parameter of the COMb distribution
2416 detected some positive association between the neurons at stimulus onset. So, for particularly
2417 short time bins, where neurons can be treated as Bernoulli random variables, the Conway-
2418 Maxwell-binomial distribution is a good way to capture correlated behaviour. There are
2419 other measurements for capturing association to which this distribution should be compared.
2420 Cross-correlograms could be used for some measure of synchrony, for example.

2421 Finally, we replicated a famous finding of Churchland et al. (2010) relating to the quench-
2422 ing of neural variability at stimulus onset, thereby finding a parallel between this reduction
2423 in the Fano factor and a reduction in the association parameter of the COMb distribution.

2424 We showed that computational neuroscientists can make progress by being inventive with
2425 their statistical models. A similar distribution to investigate would be the Conway-Maxwell-
2426 Poisson distribution. This is similar to the standard Poisson distribution, but with an addi-
2427 tional parameter that allows for over- or under- dispersion relative to a Poisson distribution.
2428 This might be ideal for modelling firing rates of individual neurons. Some interaction be-
2429 tween the fitted parameters could capture the association between neurons.

2430 There is one technology that has the potential to take over from both electrophysiology
2431 and calcium imaging. The technique of voltage imaging has become more useful in recent
2432 years. The aim for neuroscience would be to develop a voltage imaging dye or protein that

2433 images the membrane potential of a neuron with enough spatial and temporal resolution to
2434 detect action potentials. Genetically encoded voltage indicators have been developed, and
2435 enable targeting of specific neuronal ensembles. But their spatial resolution is not yet high
2436 enough to single out individual cells (Bando et al., 2019). These indicators have the potential
2437 to take over from calcium imaging, and if imaging deep within the brain becomes possible,
2438 electrophysiology could also be replaced. This is specualtaion, but the potential is there.

2439 Bibliography

- 2440 Allen, William E. et al. (2019). “Thirst regulates motivated behavior through modulation of
 2441 brainwide neural population dynamics”. In: *Science* 364.6437. ISSN: 0036-8075. DOI:
 2442 [10.1126/science.aav3932](https://doi.org/10.1126/science.aav3932). eprint: <https://science.sciencemag.org/content/364/6437/eaav3932.full.pdf>. URL: <https://science.sciencemag.org/content/364/6437/eaav3932>.
- 2445 Baadel, S., F. Thabtah, and J. Lu (2016). “Overlapping clustering: A review”. In: *2016 SAI Computing Conference (SAI)*, pp. 233–237. DOI: [10.1109/SAI.2016.7555988](https://doi.org/10.1109/SAI.2016.7555988).
- 2447 Baldassano, Christopher et al. (2017). “Discovering Event Structure in Continuous Narrative Perception and Memory”. In: *Neuron* 95.3, 709 –721.e5. ISSN: 0896-6273. DOI: <https://doi.org/10.1016/j.neuron.2017.06.041>. URL: <http://www.sciencedirect.com/science/article/pii/S0896627317305937>.
- 2451 Bando, Yuki et al. (2019). “Genetic voltage indicators”. In: *BMC Biology* 17.1, p. 71. ISSN:
 2452 1741-7007. DOI: [10.1186/s12915-019-0682-0](https://doi.org/10.1186/s12915-019-0682-0). URL: <https://doi.org/10.1186/s12915-019-0682-0>.
- 2454 Bartol, Thomas M. et al. (2015). “Computational reconstitution of spine calcium transients from individual proteins”. In: *Frontiers in Synaptic Neuroscience* 7, p. 17. ISSN: 1663-
 2455 3563. DOI: [10.3389/fnsyn.2015.00017](https://doi.org/10.3389/fnsyn.2015.00017). URL: <https://www.frontiersin.org/article/10.3389/fnsyn.2015.00017>.
- 2458 Berens, Philipp et al. (May 2018). “Community-based benchmarking improves spike rate inference from two-photon calcium imaging data”. In: *PLOS Computational Biology* 14.5, pp. 1–13. DOI: [10.1371/journal.pcbi.1006157](https://doi.org/10.1371/journal.pcbi.1006157). URL: <https://doi.org/10.1371/journal.pcbi.1006157>.
- 2462 Bezanson, Jeff et al. (Sept. 2012). “Julia: A Fast Dynamic Language for Technical Computing”. In: *MIT*.
- 2464 Buccino, Alessio P. et al. (2019). “SpikeInterface, a unified framework for spike sorting”. In: *bioRxiv*. DOI: [10.1101/796599](https://doi.org/10.1101/796599). eprint: <https://www.biorxiv.org/content/early/2019/10/07/796599.full.pdf>. URL: <https://www.biorxiv.org/content/early/2019/10/07/796599>.

- 2468 Chen, Tsai-Wen et al. (July 2013). “Ultrasensitive fluorescent proteins for imaging neuronal
2469 activity”. In: *Nature* 499, 295–300. DOI: [10.1038/nature12354](https://doi.org/10.1038/nature12354). URL: <https://doi.org/10.1038/nature12354>.
- 2471 Churchland, Mark M. et al. (2010). “Stimulus onset quenches neural variability: a widespread
2472 cortical phenomenon”. eng. In: *Nature neuroscience* 13.3. 20173745[pmid], pp. 369–378.
2473 ISSN: 1546-1726. DOI: [10.1038/nn.2501](https://doi.org/10.1038/nn.2501). URL: <https://pubmed.ncbi.nlm.nih.gov/20173745>.
- 2475 Cohen, Marlene R. and Adam Kohn (2011). “Measuring and interpreting neuronal correla-
2476 tions”. In: *Nature Neuroscience* 14.7, pp. 811–819. ISSN: 1546-1726. DOI: [10.1038/nn.2842](https://doi.org/10.1038/nn.2842). URL: <https://doi.org/10.1038/nn.2842>.
- 2478 Cohen, Marlene R. and John H. R. Maunsell (2009). “Attention improves performance pri-
2479 marily by reducing interneuronal correlations”. eng. In: *Nature neuroscience* 12.12. 19915566[pmid],
2480 pp. 1594–1600. ISSN: 1546-1726. DOI: [10.1038/nn.2439](https://doi.org/10.1038/nn.2439). URL: <https://pubmed.ncbi.nlm.nih.gov/19915566>.
- 2482 Dana, Hod et al. (Sept. 2014). “Thy1-GCaMP6 Transgenic Mice for Neuronal Population
2483 Imaging In Vivo”. In: *PloS one* 9, e108697. DOI: [10.1371/journal.pone.0108697](https://doi.org/10.1371/journal.pone.0108697).
- 2485 deCharms, R. Christopher and Michael M. Merzenich (1996). “Primary cortical represen-
2486 tation of sounds by the coordination of action-potential timing”. In: *Nature* 381.6583,
2487 pp. 610–613. ISSN: 1476-4687. DOI: [10.1038/381610a0](https://doi.org/10.1038/381610a0). URL: <https://doi.org/10.1038/381610a0>.
- 2489 Deneux, Thomas et al. (July 2016). “Accurate spike estimation from noisy calcium signals
2490 for ultrafast three-dimensional imaging of large neuronal populations in vivo”. In: *Nature
2491 Communications* 7.1. DOI: [10.1038/ncomms12190](https://doi.org/10.1038/ncomms12190). URL: <https://doi.org/10.1038/ncomms12190>.
- 2493 Faas, Guido C. et al. (2011). “Calmodulin as a direct detector of Ca2+ signals”. In: *Nature
2494 Neuroscience* 14.3, pp. 301–304. ISSN: 1546-1726. DOI: [10.1038/nn.2746](https://doi.org/10.1038/nn.2746). URL:
2495 <https://doi.org/10.1038/nn.2746>.
- 2496 Fiala, John C. and Kristen M. Harris (1999). *Dendrite Structure*.
- 2497 Flach, Boris (Sept. 2013). “A Class of Random Fields on Complete Graphs with Tractable
2498 Partition Function”. In: *IEEE transactions on pattern analysis and machine intelligence*
2499 35, pp. 2304–6. DOI: [10.1109/TPAMI.2013.99](https://doi.org/10.1109/TPAMI.2013.99).
- 2500 Forney, G. D. (1973). “The viterbi algorithm”. In: *Proceedings of the IEEE* 61.3, pp. 268–
2501 278. ISSN: 1558-2256. DOI: [10.1109/PROC.1973.9030](https://doi.org/10.1109/PROC.1973.9030).

- 2502 Fosdick, Bailey et al. (Aug. 2016). “Configuring Random Graph Models with Fixed Degree
2503 Sequences”. In: *SIAM Review* 60. DOI: [10.1137/16M1087175](https://doi.org/10.1137/16M1087175).
- 2504 Friedrich, Johannes and Liam Paninski (2016). “Fast Active Set Methods for Online Spike
2505 Inference from Calcium Imaging”. In: *Advances in Neural Information Processing Sys-*
2506 *tems* 29. Ed. by D. D. Lee et al. Curran Associates, Inc., pp. 1984–1992. URL: [http://papers.nips.cc/paper/6505-fast-active-set-methods-for-](http://papers.nips.cc/paper/6505-fast-active-set-methods-for-online-spike-inference-from-calcium-imaging.pdf)
2507 online-spike-inference-from-calcium-imaging.pdf.
- 2508
- 2509 Ganmor, Elad, Ronen Segev, and Elad Schneidman (2011). “Sparse low-order interaction
2510 network underlies a highly correlated and learnable neural population code”. In: *Proceed-*
2511 *ings of the National Academy of Sciences* 108.23, pp. 9679–9684. ISSN: 0027-8424. DOI:
2512 [10.1073/pnas.1019641108](https://doi.org/10.1073/pnas.1019641108). eprint: <https://www.pnas.org/content/108/23/9679.full.pdf>. URL: <https://www.pnas.org/content/108/23/9679>.
- 2513
- 2514
- 2515 Girard, P., J. M. Hupé, and J. Bullier (2001). “Feedforward and Feedback Connections Be-
2516 tween Areas V1 and V2 of the Monkey Have Similar Rapid Conduction Velocities”. In:
2517 *Journal of Neurophysiology* 85.3. PMID: 11248002, pp. 1328–1331. DOI: [10.1152/jn.2001.85.3.1328](https://doi.org/10.1152/jn.2001.85.3.1328). eprint: <https://doi.org/10.1152/jn.2001.85.3.1328>. URL: <https://doi.org/10.1152/jn.2001.85.3.1328>.
- 2516
- 2517
- 2518
- 2519
- 2520 Greenberg, David et al. (Nov. 2018). “Accurate action potential inference from a calcium
2521 sensor protein through biophysical modeling:” in: DOI: [10.1101/479055](https://doi.org/10.1101/479055).
- 2521
- 2522 Gründemann, Jan et al. (2019). “Amygdala ensembles encode behavioral states”. In: *Science*
2523 364.6437. ISSN: 0036-8075. DOI: [10.1126/science.aav8736](https://doi.org/10.1126/science.aav8736). eprint: <https://science.sciencemag.org/content/364/6437/eaav8736.full.pdf>. URL: <https://science.sciencemag.org/content/364/6437/eaav8736>.
- 2524
- 2525
- 2526
- 2527 Hodgkin, A. L. and A. F. Huxley (1939). “Action Potentials Recorded from Inside a Nerve Fi-
2528 bre”. In: *Nature* 144.3651, pp. 710–711. ISSN: 1476-4687. DOI: [10.1038/144710a0](https://doi.org/10.1038/144710a0).
2529 URL: <https://doi.org/10.1038/144710a0>.
- 2530 Humphries, Mark et al. (Jan. 2019). “Spectral rejection for testing hypotheses of structure in
2531 networks”. In:
- 2532 Humphries, Mark D. (2011). “Spike-Train Communities: Finding Groups of Similar Spike
2533 Trains”. In: *Journal of Neuroscience* 31.6, pp. 2321–2336. ISSN: 0270-6474. DOI: [10.1523/JNEUROSCI.2853-10.2011](https://doi.org/10.1523/JNEUROSCI.2853-10.2011). eprint: <https://www.jneurosci.org/>
- 2533
- 2534

- 2535 [content/31/6/2321.full.pdf](https://www.jneurosci.org/content/31/6/2321.full.pdf). URL: <https://www.jneurosci.org/content/31/6/2321>.
- 2536
- 2537 Jun, James J. et al. (2017). “Fully integrated silicon probes for high-density recording of
2538 neural activity”. In: *Nature* 551.7679, pp. 232–236. ISSN: 1476-4687. DOI: [10.1038/nature24636](https://doi.org/10.1038/nature24636). URL: <https://doi.org/10.1038/nature24636>.
- 2540 Kadane, Joseph B. (June 2016). “Sums of Possibly Associated Bernoulli Variables: The
2541 Conway–Maxwell-Binomial Distribution”. In: *Bayesian Anal.* 11.2, pp. 403–420. DOI:
2542 [10.1214/15-BA955](https://doi.org/10.1214/15-BA955). URL: <https://doi.org/10.1214/15-BA955>.
- 2543 Kilhoffer, Marie-Claude et al. (Sept. 1992). “Use of Engineered Proteins With Internal Tryp-
2544 tophean Reporter Groups and Perturbation Techniques to Probe the Mechanism of Ligand-
2545 Protein Interactions: Investigation of the Mechanism of Calcium Binding to Calmod-
2546 ulin”. In: *Biochemistry* 31.34, pp. 8098–8106. DOI: [10.1021/bi00149a046](https://doi.org/10.1021/bi00149a046). URL:
2547 <https://doi.org/10.1021/bi00149a046>.
- 2548 Koch, Christoff (1999). *Biophysics of Computation: Information Processing in Single Neu-*
2549 *rons*. Oxford University Press. ISBN: ISBN 0-19-510491-9.
- 2550 Kolaczyk, Eric and Haiying Huang (Sept. 2010). “Multiscale Statistical Models for Hier-
2551 archical Spatial Aggregation”. In: *Geographical Analysis* 33, pp. 95 –118. DOI: [10.1111/j.1538-4632.2001.tb00439.x](https://doi.org/10.1111/j.1538-4632.2001.tb00439.x).
- 2553 Lee, Suk-HO et al. (July 2000). “Differences in Ca²⁺ buffering properties between excitatory
2554 and inhibitory hippocampal neurons from the rat”. In: *The Journal of Physiology* 525.
2555 DOI: [10.1111/j.1469-7793.2000.t01-3-00405.x](https://doi.org/10.1111/j.1469-7793.2000.t01-3-00405.x).
- 2556 Litwin-Kumar, Ashok, Maurice Chacron, and Brent Doiron (Sept. 2012). “The Spatial Struc-
2557 ture of Stimuli Shapes the Timescale of Correlations in Population Spiking Activity”.
2558 In: *PLoS computational biology* 8, e1002667. DOI: [10.1371/journal.pcbi.1002667](https://doi.org/10.1371/journal.pcbi.1002667).
- 2560 Maravall, M et al. (May 2000). “Estimating intracellular calcium concentrations and buffer-
2561 ing without wavelength ratioing”. In: *Biophysical Journal* 78.5, pp. 2655–2667. DOI:
2562 [10.1016/S0006-3495\(00\)76809-3](https://doi.org/10.1016/S0006-3495(00)76809-3). URL: [https://doi.org/10.1016/S0006-3495\(00\)76809-3](https://doi.org/10.1016/S0006-3495(00)76809-3).
- 2564 Maugis, Pa (Jan. 2014). “Event Conditional Correlation: Or How Non-Linear Linear Depen-
2565 dence Can Be”. In:
- 2566 Meilă, Marina (2007). “Comparing clusterings—an information based distance”. In: *Journal*
2567 *of Multivariate Analysis* 98.5, pp. 873 –895. ISSN: 0047-259X. DOI: <https://doi.org/10.1016/j.jmva.2006.09.006>.

- 2568 [org/10.1016/j.jmva.2006.11.013](http://doi.org/10.1016/j.jmva.2006.11.013). URL: <http://www.sciencedirect.com/science/article/pii/S0047259X06002016>.
- 2569
- 2570 Murray, John D. et al. (2014). “A hierarchy of intrinsic timescales across primate cortex”.
2571 In: *Nature Neuroscience* 17.12, pp. 1661–1663. ISSN: 1546-1726. DOI: [10.1038/nn.3862](https://doi.org/10.1038/nn.3862). URL: <https://doi.org/10.1038/nn.3862>.
- 2572
- 2573 Neher, E. and G. J. Augustine (1992). “Calcium gradients and buffers in bovine chromaffin
2574 cells”. eng. In: *The Journal of physiology* 450. 1331424[pmid], pp. 273–301. ISSN: 0022-
2575 3751. DOI: [10.1113/jphysiol.1992.sp019127](https://doi.org/10.1113/jphysiol.1992.sp019127). URL: <https://pubmed.ncbi.nlm.nih.gov/1331424>.
- 2576
- 2577 O’Donnell, Cian et al. (Jan. 2017). “The population tracking model: a simple, scalable statistical
2578 model for neural population data”. English. In: *Neural Computation* 29.1, pp. 50–
2579 93. ISSN: 0899-7667. DOI: [10.1162/NECO_a_00910](https://doi.org/10.1162/NECO_a_00910).
- 2580
- 2581 Okun, Michael et al. (2015). “Diverse coupling of neurons to populations in sensory cortex”.
2582 In: *Nature* 521.7553, pp. 511–515. ISSN: 1476-4687. DOI: [10.1038/nature14273](https://doi.org/10.1038/nature14273).
2583 URL: <https://doi.org/10.1038/nature14273>.
- 2584
- 2585 Ouzounov, Dimitre G. et al. (2017). “In vivo three-photon imaging of activity of GCaMP6-
2586 labeled neurons deep in intact mouse brain”. eng. In: *Nature methods* 14.4. 28218900[pmid],
2587 pp. 388–390. ISSN: 1548-7105. DOI: [10.1038/nmeth.4183](https://doi.org/10.1038/nmeth.4183). URL: <https://pubmed.ncbi.nlm.nih.gov/28218900>.
- 2588
- 2589 Patterson, Carolyn A. et al. (2014). “Similar adaptation effects in primary visual cortex and
2590 area MT of the macaque monkey under matched stimulus conditions”. In: *Journal of Neurophysiology* 111.6. PMID: 24371295, pp. 1203–1213. DOI: [10.1152/jn.00030.2013](https://doi.org/10.1152/jn.00030.2013). eprint: <https://doi.org/10.1152/jn.00030.2013>. URL: <https://doi.org/10.1152/jn.00030.2013>.
- 2591
- 2592 Peron, Simon P. et al. (2015). “A Cellular Resolution Map of Barrel Cortex Activity during
2593 Tactile Behavior”. In: *Neuron* 86.3, pp. 783–799. ISSN: 0896-6273. DOI: [10.1016/j.neuron.2015.03.027](https://doi.org/10.1016/j.neuron.2015.03.027). URL: <https://doi.org/10.1016/j.neuron.2015.03.027>.
- 2594
- 2595 Pnevmatikakis, E.A. et al. (Jan. 2016). “Simultaneous Denoising, Deconvolution, and Demixing
2596 of Calcium Imaging Data”. In: *Neuron* 89.2, pp. 285–299. DOI: [10.1016/j.neuron.2015.11.037](https://doi.org/10.1016/j.neuron.2015.11.037). URL: <https://doi.org/10.1016/j.neuron.2015.11.037>.
- 2597
- 2598
- 2599

- 2600 Pnevmatikakis, Eftychios et al. (Nov. 2013). “Bayesian spike inference from calcium imaging
2601 data”. In: *Conference Record - Asilomar Conference on Signals, Systems and Computers*.
2602 DOI: [10.1109/ACSSC.2013.6810293](https://doi.org/10.1109/ACSSC.2013.6810293).
- 2603 Pnevmatikakis, Eftychios et al. (Sept. 2014). “A structured matrix factorization framework
2604 for large scale calcium imaging data analysis”. In:
- 2605 Schneidman, Elad et al. (2006). “Weak pairwise correlations imply strongly correlated net-
2606 work states in a neural population”. eng. In: *Nature* 440.7087. 16625187[pmid], pp. 1007–
2607 1012. ISSN: 1476-4687. DOI: [10.1038/nature04701](https://doi.org/10.1038/nature04701). URL: <https://pubmed.ncbi.nlm.nih.gov/16625187>.
- 2609 Shannon, C. E. (1948). “A Mathematical Theory of Communication”. In: *Bell System Techni-*
2610 *cal Journal* 27.3, pp. 379–423. DOI: [10.1002/j.1538-7305.1948.tb01338.x](https://doi.org/10.1002/j.1538-7305.1948.tb01338.x).
2611 eprint: <https://onlinelibrary.wiley.com/doi/pdf/10.1002/j.1538-7305.1948.tb01338.x>. URL: <https://onlinelibrary.wiley.com/doi/abs/10.1002/j.1538-7305.1948.tb01338.x>.
- 2614 Shimazaki, Hideaki et al. (2012). “State-space analysis of time-varying higher-order spike
2615 correlation for multiple neural spike train data”. eng. In: *PLoS computational biology* 8.3.
2616 22412358[pmid], e1002385–e1002385. ISSN: 1553-7358. DOI: [10.1371/journal.pcbi.1002385](https://doi.org/10.1371/journal.pcbi.1002385). URL: <https://pubmed.ncbi.nlm.nih.gov/22412358>.
- 2618 Staude, Benjamin, Sonja Grün, and Stefan Rotter (2010). “Higher-Order Correlations and
2619 Cumulants”. In: *Analysis of Parallel Spike Trains*. Ed. by Sonja Grün and Stefan Rotter.
2620 Boston, MA: Springer US, pp. 253–280. ISBN: 978-1-4419-5675-0. DOI: [10.1007/978-1-4419-5675-0_12](https://doi.org/10.1007/978-1-4419-5675-0_12). URL: https://doi.org/10.1007/978-1-4419-5675-0_12.
- 2623 Stein, Astrid von and Johannes Sarnthein (2000). “Different frequencies for different scales
2624 of cortical integration: from local gamma to long range alpha/theta synchronization”. In:
2625 *International Journal of Psychophysiology* 38.3, pp. 301 –313. ISSN: 0167-8760. DOI:
2626 [https://doi.org/10.1016/S0167-8760\(00\)00172-0](https://doi.org/10.1016/S0167-8760(00)00172-0). URL: <http://www.sciencedirect.com/science/article/pii/S0167876000001720>.
- 2628 Steinmetz, Nick, Matteo Carandini, and Kenneth D. Harris (2019). ”Single Phase3” and
2629 ”Dual Phase3” Neuropixels Datasets. DOI: [10.6084/m9.figshare.7666892.v2](https://doi.org/10.6084/m9.figshare.7666892.v2). URL: https://figshare.com/articles/dataset/_Single_Phase3_Neuropixels_Dataset/7666892/2.
- 2632 Steinmetz, Nick et al. (Mar. 2019). “Eight-probe Neuropixels recordings during sponta-
2633 neous behaviors”. In: DOI: [10.25378/janelia.7739750.v4](https://doi.org/10.25378/janelia.7739750.v4). URL: <https://doi.org/10.25378/janelia.7739750.v4>

- 2634 //janelia.figshare.com/articles/Eight-probe_Neuropixels_
2635 recordings_during_spontaneous_behaviors/7739750.
- 2636 Stringer, Carsen et al. (2019). "Spontaneous behaviors drive multidimensional, brainwide ac-
2637 tivity". In: *Science* 364.6437. ISSN: 0036-8075. DOI: 10.1126/science.aav7893.
2638 eprint: <https://science.sciencemag.org/content/364/6437/eaav7893.full.pdf>. URL: <https://science.sciencemag.org/content/364/6437/eaav7893>.
- 2639
2640
- 2641 Tada, Mayumi et al. (2014). "A highly sensitive fluorescent indicator dye for calcium imag-
2642 ing of neural activity in vitro and in vivo". In: *European Journal of Neuroscience* 39.11,
2643 pp. 1720–1728. DOI: 10.1111/ejn.12476. eprint: <https://onlinelibrary.wiley.com/doi/pdf/10.1111/ejn.12476>. URL: <https://onlinelibrary.wiley.com/doi/abs/10.1111/ejn.12476>.
- 2644
2645
- 2646 Tian, Lin et al. (2009). "Imaging neural activity in worms, flies and mice with improved
2647 GCaMP calcium indicators". eng. In: *Nature methods* 6.12. 19898485[pmid], pp. 875–
2648 881. ISSN: 1548-7105. DOI: 10.1038/nmeth.1398. URL: <https://pubmed.ncbi.nlm.nih.gov/19898485>.
- 2649
- 2650 Tkačík, Gašper et al. (2014). "Searching for collective behavior in a large network of sen-
2651 sory neurons". eng. In: *PLoS computational biology* 10.1. 24391485[pmid], e1003408–
2652 e1003408. ISSN: 1553-7358. DOI: 10.1371/journal.pcbi.1003408. URL:
2653 <https://pubmed.ncbi.nlm.nih.gov/24391485>.
- 2654
2655
- 2656 Treves, Alessandro and Stefano Panzeri (1995). "The Upward Bias in Measures of Informa-
2657 tion Derived from Limited Data Samples". In: *Neural Computation* 7.2, pp. 399–407.
2658 DOI: 10.1162/neco.1995.7.2.399. eprint: <https://doi.org/10.1162/neco.1995.7.2.399>. URL: <https://doi.org/10.1162/neco.1995.7.2.399>.
- 2659
2660
- 2661 Vinh, Nguyen Xuan, Julien Epps, and James Bailey (Dec. 2010). "Information Theoretic
2662 Measures for Clusterings Comparison: Variants, Properties, Normalization and Correc-
2663 tion for Chance". In: *J. Mach. Learn. Res.* 11, 2837–2854. ISSN: 1532-4435.
- 2664
2665
- 2666 Vogelstein, Joshua T. et al. (Oct. 2010). "Fast nonnegative deconvolution for spike train infer-
2667 ence from population calcium imaging". In: *Journal of neurophysiology* 104.6, 295–300.
2668 DOI: 10.1152/jn.01073.2009. URL: <https://dx.doi.org/10.1152%2Fjn.01073.2009>.
- 2669
2670
- 2671 Wierzynski, Casimir M. et al. (2009). "State-Dependent Spike-Timing Relationships be-
2672 tween Hippocampal and Prefrontal Circuits during Sleep". In: *"Neuron"* "61": "4", "587

- 2668 –596”. ISSN: ”0896-6273”. DOI: <https://doi.org/10.1016/j.neuron.2009.01.011>. URL: <http://www.sciencedirect.com/science/article/pii/S0896627309000786>.
- 2671 Zariwala, Hatim A. et al. (2012). “A Cre-dependent GCaMP3 reporter mouse for neuronal
2672 imaging in vivo”. eng. In: *The Journal of neuroscience : the official journal of the Society
2673 for Neuroscience* 32.9. 22378886[pmid], pp. 3131–3141. ISSN: 1529-2401. DOI: [10.1523/JNEUROSCI.4469-11.2012](https://doi.org/10.1523/JNEUROSCI.4469-11.2012). URL: <https://pubmed.ncbi.nlm.nih.gov/22378886>.
- 2676 Zou, Hui and Trevor Hastie (2005). “Regularization and variable selection via the Elastic
2677 Net”. In: *Journal of the Royal Statistical Society, Series B* 67, pp. 301–320.
- 2678 Éltes, Tímea et al. (2019). “Improved spike inference accuracy by estimating the peak am-
2679 plitude of unitary [Ca₂₊] transients in weakly GCaMP6f-expressing hippocampal pyra-
2680 midal cells”. In: *The Journal of Physiology* 597.11, pp. 2925–2947. DOI: [10.1113/JP277681](https://doi.org/10.1113/JP277681). eprint: <https://physoc.onlinelibrary.wiley.com/doi/pdf/10.1113/JP277681>. URL: <https://physoc.onlinelibrary.wiley.com/doi/abs/10.1113/JP277681>.
- 2682
- 2683